

**ENHANCEMENT AND EVALUATION OF PAN-DERIVED
CARBON FIBRES AND RESULTING COMPOSITES BY
ACTIVE SCREEN PLASMA SURFACE MODIFICATION**

by

YANA LIANG



A thesis submitted to

The University of Birmingham

for the degree of

DOCTOR OF PHILOSOPHY

School of Metallurgy and Materials

College of Engineering and Physical Sciences

The University of Birmingham

May 2021

UNIVERSITY OF
BIRMINGHAM

University of Birmingham Research Archive

e-theses repository

This unpublished thesis/dissertation is copyright of the author and/or third parties. The intellectual property rights of the author or third parties in respect of this work are as defined by The Copyright Designs and Patents Act 1988 or as modified by any successor legislation.

Any use made of information contained in this thesis/dissertation must be in accordance with that legislation and must be properly acknowledged. Further distribution or reproduction in any format is prohibited without the permission of the copyright holder.

Synopsis

Owing to their excellent properties, such as outstanding mechanical properties, high strength to weight ratio, high thermal stability and corrosion resistance, carbon fibres (CFs) have become materials of choice for the reinforcements of high-performance composites. However, their chemical inertness and low surface free energy, which is attributed to their high density of graphitic planes on the surface, limit the interfacial adhesion of CFs to the matrix. This poses a critical challenge in further improving the properties of CFs reinforced composites to meet the requirement arising from demanding applications.

To this end, numerous surface modification methods have been developed to improve interfacial adhesion of CFs to the matrix in composites, such as chemical treatment, electrochemical treatment, plasma treatment and polymer/nano particles coating. However, most of these treatments either lead to environmental concerns due to the use of toxic chemicals or reduce more or less the mechanical properties of CFs due to surface damage.

Plasma treatment is highlighted as an environmentally-friendly, economic and adaptable process for surface treatment of CFs with less impact on the fibre strength as compared with other methods. However, conventional direct plasma still damages the fibre surface due to ions bombardment. Therefore, a more advanced plasma technology, active screen plasma (ASP), has been developed to avoid the undesirable effects associated with conventional direct plasma treatment such as arcing, edge effect and hollow-cathode induced damage.

In this project, advanced active screen plasma technology has been developed to modify PAN-derived CF surfaces. The ASP modified CF surfaces were fully characterised by scanning electron microscopy (SEM), atomic force microscopy (AFM), X-ray diffraction (XRD), Raman spectroscopy, X-ray photoelectron spectroscopy (XPS) and dynamic vapour sorption

(DVS) to understand the response of CF surface to the active screen plasma. Single fibre tensile tests were carried out to directly study the effect of ASP treatment on single fibre tensile strength. Nano-indentation enabled single fibre push-out testing method, which was further improved by purposely designing the sample holder and using a conical indenter, was adopted to evaluate the interfacial adhesion between the ASP modified CF and the epoxy resin. Interlaminar shear strength, flexural strength and fracture toughness of ASP modified CF/epoxy composites were also evaluated.

The results have demonstrated that the advanced ASP technology is capable of modifying the CF surface without causing any surface damage or tensile strength degradation. Unlike conventional plasma treatments, the ASP treatments can reduce the structural disorder of the CF surfaces and increase the surface crystallite size. Moreover, the ASP treatments can lead to an increased single fibre tensile strength. This is mainly because the post-plasma nature of the ASP technology can effectively eliminate ion bombardment induced degradation while providing radicals necessary for surface modification. Changes have also been found in the chemical composition and wettability of the ASP modified fibre surfaces. Furthermore, a more than 30% improvement was found in the interfacial shear strength (IFSS) between the modified CFs and the epoxy substrate as disclosed by push-out tests. The mechanical properties (shear strength, flexural strength and fracture toughness) of the composites reinforced with ASP modified CFs have been improved as well.

Based on the experimental results, the potential mechanisms involved in the interaction between the CF surface and the active screen plasma, significantly increased single fibre tensile strength, effectively improved interfacial shear strength and enhanced mechanical properties of CF-reinforced composites have been discussed.

Acknowledgements

First of all, I would like to express my sincere gratitude to my supervisors Prof Hanshan Dong and Dr Xiaoying Li, for the opportunity to carry out this wonderful project and their invaluable supervision throughout this study. Both of them have contributed their knowledge and experience, as well as plenty of inspiring advice, without which I could not have and developed my research skills and completed this study.

I wish to express my deep appreciation to the School of Metallurgy and Materials at the University of Birmingham, and also to the Engineering and Physical Sciences Research Council (EPSRC) Innovative Metal Processing Centre for Doctoral Training (IMPACT) scheme for providing financial support for this study.

I would like to acknowledge all the members/alumni of the Surface Engineering Group who have helped me throughout my PhD study, especially, Dr Santiago Corujeira Gallo, Dr Zhenxue Zhang, Dr Kaijie Lin, Dr Shaojun Qi and Dr Behnam Dashtbozorg.

I would also like to send my thanks to Prof. Alberto Tagliaferro and Dr Mauro Giorcelli for performing XPS tests and providing their invaluable suggestions, to Dr Dionisis Semitekolos and Mr Miles Holt for conducting composite coupon tests, and to Dr Daniel Reed for kindly providing Raman and XRD training.

Finally, I would like to express my love and deepest gratitude to my parents, sister and brother who are proud of me and have provided me constant support, and to my dear fiancée who always encourages me and makes my PhD journey much more enjoyable. Many thanks also to all my friends who have spent the years and shared memories with me.

List of Publications

Journals

- **Y. Liang**, X. Li, D. Semitekolos, C. A. Charitidis and H. Dong. *Enhanced properties of PAN-derived carbon fibres and resulting composites by active screen plasma surface functionalisation*. Plasma Processes and Polymers, 2020. **17**(4): p. 1900252.
- **Y. Liang**, X. Li, M. Giorcelli, A. Tagliaferro, C. A. Charitidis and H. Dong. *Enhancement and evaluation of interfacial adhesion between active screen plasma surface functionalised carbon fibres and the epoxy substrate*. Polymers, 2021 Submitted.
- Z. Li, S. Qi, **Y. Liang**, Z. Zhang, X. Li and H. Dong. *Plasma surface functionalization of carbon nanofibres with silver, palladium and platinum nanoparticles for cost-effective and high-performance supercapacitors*. Micromachines, 2019. **10**(1): p. 2.
- D. Semitekolos, A. Trompeta, I. Husarova, T. Man'ko, A. Potapov, O. Romenskaya, **Y. Liang**, et al. *Comparative physical–mechanical properties assessment of tailored surface-treated carbon fibres*. Materials, 2020. **13**(14): p. 3136.
- A. Garcia-Giron, J. M. Romano, **Y. Liang**, B. Dashtbozorg, H. Dong and P. Penchev. *Combined surface hardening and laser patterning approach for functionalising stainless steel surfaces*. Applied Surface Science, 2018. **439**: p. 516-524.
- M. Giorcelli, S. Guastella, P. Mandracci, **Y. Liang**, X. Li and A. Tagliaferro. *Carbon fibre functionalisation by plasma treatment for adhesion enhancement on polymers*. AIP Conference Proceedings, 2018. **1981**: p. 202142.

Conferences

- Surface activation and functionalisation of carbon fibres for improved IFSS of CFR composites. Oral presentation. **4th composites @ Manchester**, June 2019, Manchester, UK.
- The effect of rapid annealing on the stability of S-phase formed on the surface of AISI 316 stainless steel by low-temperature plasma nitriding. Poster presentation. **5th UK-China Steel Research Forum**, July 2018, Birmingham, UK.
- Plasma activation and functionalisation of carbon fibres for improved carbon fibre/polymer matrix interfacial bonding. Poster presentation. **National Student Conference in Metallic Materials**, July 2018, Sheffield, UK.
- Response of S-phase to rapid annealing. Poster presentation. **9th World congress on materials science and engineering**, June 2017, Rome, Italy.

Table of Contents

CHAPTER 1 INTRODUCTION	1
CHAPTER 2 LITERATURE REVIEW	4
2.1 History and development of carbon fibre	4
2.2 Carbon fibre manufacturing, structure and property	6
2.2.1 PAN-derived CF manufacturing.....	6
2.2.2 Pitch-derived CF manufacturing.....	10
2.2.3 Structure, morphology and properties of CF.....	11
2.3 Carbon fibre-reinforced composites (CFRC).....	17
2.3.1 Fabrication process for composites	18
2.3.2 Properties of CF-reinforced composites.....	21
2.3.3 Applications	21
2.4 Carbon fibre/matrix interface.....	24
2.4.1 Introduction of interface.....	24
2.4.2 Interfacial shear strength (IFSS)	26
2.5 Characterisation of interfacial adhesion.....	27
2.5.1 Interfacial shear strength testing	27
2.5.2 Mechanical properties testing of composites	32
2.6 Surface modification on CF	35
2.6.1 Surface modification effects	35
2.6.2 Gas-phase oxidative surface treatments.....	38
2.6.3 Liquid-phase oxidative surface treatments.....	39
2.6.4 Electrochemical oxidative surface treatments.....	40
2.6.5 Thin coatings or nanostructures	41
2.6.6 Plasma surface treatments	42
2.7 Summary	48
CHAPTER 3 EXPERIMENTAL.....	50
3.1 Materials	50

3.2 Active screen plasma treatment.....	51
3.3 General characterisation.....	53
3.3.1 Scanning electron microscopy (SEM)	53
3.3.2 Atomic force microscope (AFM).....	53
3.3.3 Raman spectra.....	53
3.3.4 X-ray diffraction (XRD)	54
3.3.5 X-ray photoelectron spectroscopy (XPS).....	54
3.3.6 Contact angle	55
3.3.7 Dynamic vapour sorption (DVS).....	55
3.3.8 Tensile test of single fibre	56
3.3.9 Tensile test of fibre bundle.....	57
3.4 Evaluation of CF/epoxy interfacial adhesion.....	59
3.4.1 Preparation of composite slice and sample support	59
3.4.2 Interfacial shear strength (IFSS) test.....	60
3.4.3 Nano-indentation creep test	63
3.5 Evaluation of the mechanical properties of composites.....	65
3.5.1 Fabrication of CF reinforced composites.....	65
3.5.2 Tensile test.....	66
3.5.3 Short beam shear test	66
3.5.4 Three-point bending test	67
3.5.5 Mode I interlaminar fracture test	68
3.5.6 Internal pressure destructive test.....	70
CHAPTER 4 RESULTS AND DISCUSSION	72
4.1 Morphology, structure and chemistry	72
4.1.1 Surface morphology.....	72
4.1.2 Distortion of CF surface after ASP treatments.....	76
4.1.3 Change of CF turbostratic structure by ASP treatments.....	80
4.1.4 Surface chemistry.....	83
4.2 Mechanical property and surface hydrophilicity.....	89

4.2.1 Surface wettability and durability	89
4.2.2 Surface water-sorption behaviour	92
4.2.3 Tensile strength	98
4.3 Evaluation of CF/epoxy interfacial adhesion.....	102
4.3.1 Optimisation of nano-indentation enabled push-out testing	102
4.3.2 Interpretation of load-displacement curves.....	109
4.3.3 Load-displacement curves and post observations	111
4.3.4 Interfacial shear strength (IFSS)	116
4.3.5 Creep behaviour of the CF/matrix system	118
4.4 Mechanical properties of carbon fibre reinforced composites	125
4.4.1 Mechanical properties of woven fabric reinforced laminate composites.....	125
4.4.2 Mechanical properties of unidirectional carbon fibre reinforced composites.....	134
CHAPTER 5 DISCUSSION	137
5.1 The interaction between active screen plasma and CF	137
5.2 Effects of ASP modification on tensile property of CFs	143
5.3 Effects of ASP modification on CF/resin interface	149
5.3.1 Changes in surface topography	149
5.3.3 Improvement of surface wettability	152
5.4 Effect of ASP modification on CFs reinforced epoxy composite	156
CHAPTER 6 CONCLUSIONS	159
Part I – Surface modification of CF surfaces	159
Part II – Interfacial property between fibre and epoxy resin	160
Part III – Mechanical properties of CF reinforced composites	161
CHAPTER 7 FUTURE WORK.....	162
REFERENCES:	163

List of Figures

- Figure 2.1 PAN-derived CF production process.
- Figure 2.2 Chemical reactions during the stabilisation and carbonisation of PAN-derived CFs [45].
- Figure 2.3 (a) Unit cell of the turbostratic structure (b) Structural unit of the crystallites in CFs (A-A' is the fibre axis direction) and (c) Schematic diagram of the microstructure of PAN-derived CF.
- Figure 2.4 SEM micrographs of the cross-section of (a) PAN-derived CF and (b) pitch-derived CF.
- Figure 2.5 Sequence of main steps of RTM process [77].
- Figure 2.6 Schematic of the pultrusion process for composite fabrication [78].
- Figure 2.7 Schematic of filament winding process [80].
- Figure 2.8 Characteristics of the fibre/matrix interface in a composite material [71].
- Figure 2.9 Schematic illustration of the single fibre fragmentation test [118].
- Figure 2.10 Schematic set-up of (a) micro bond test [121] and (b) pull-out test [122].
- Figure 2.11 Schematic diagrams and a typical load-displacement curve of a single fibre push-out test with a conical indenter tip.
- Figure 2.12 Schematic diagram of short beam shear test.
- Figure 2.13 Double cantilever beam specimen [115].
- Figure 3.1 Schematic diagram of active screen plasma treatments.
- Figure 3.2 Schematic diagram of the petri dish holder used for contact angle measurements.
- Figure 3.3 An example of DVS test procedure.
- Figure 3.4 Paper frames with attached single fibre for tensile tests.

- Figure 3.5 Frame and attached fibre bundles for tensile tests.
- Figure 3.6 Images of (a) produced composite bars, (b) composite slices and (c) surface of polished thin composites slice.
- Figure 3.7 Images of (a) thin composite slices mounted on the metal sample support and (b) magnified grooves made on the sample support.
- Figure 3.8 (a) Nano indentation equipment and (b) close look of indentation configuration.
- Figure 3.9 Geometry schematics of the conical indenter aligned with a single CF during the push-out test.
- Figure 3.10 Images of (a) unidirectional CF prepregs, (b) unidirectional CF reinforced composites on winding mandrel and (c) woven carbon fabric reinforced laminate composite panels.
- Figure 3.11 Images of unidirectional CF prepregs on the tensile testing machine.
- Figure 3.12 Images of (a) DCB specimen with piano hinges and (b) image of crack propagation during loading of Mode I interlaminar fracture toughness experiment.
- Figure 3.13 Images of (a) structure shell on the metal mandrel; (b) carbon plastic covers; (c) propellant tanks; (d) thermographic control and (e) uniformity control by ultrasound.
- Figure 3.14 Images of (a) and (b) stain sensors on the tank outside layer and (c) internal pressure destructive test scheme.
- Figure 4.1-1 Surface morphologies of pristine and de-sized CFs observed by SEM.
- Figure 4.1-2 Surface morphologies of ASP treated CFs observed by SEM.
- Figure 4.1-3 Surface morphologies of pristine, ASPN5 and ASPAr5-10% treated CFs observed by AFM.
- Figure 4.1-4 Raman spectra of pristine and active screen plasma treated CFs.
- Figure 4.1-5 Peak fitting for Raman spectrum of ASPN5 treated CFs under Gaussian-Lorentzian function for D and G bands.
- Figure 4.1-6 XRD patterns of (a) pristine and ASP treated CFs and (b) XRD patterns at higher 2θ values.

Figure 4.1-7 XPS surface survey spectra of pristine, ASPN5 and ASPAr 5-10% treated CFs.

Figure 4.1-8 High-resolution XPS spectra deconvolution into surface functional groups for C 1s peaks area.

Figure 4.1-9 High-resolution XPS spectra deconvolution into surface functional groups for O 1s peaks area.

Figure 4.1-10 High-resolution XPS spectra deconvolution into surface functional groups for N 1s peaks area.

Figure 4.2-11 Optical microscope images of the resin droplets on single fibres for pristine and ASP modified CFs with average contact angles.

Figure 4.2-2 Evolution of the contact angle of ASPN5 treated CFs. The samples were subsequently aged in air for 10 days.

Figure 4.2-3 Contact angles for the pristine and ASP modified CFs on day 1 and day 10.

Figure 4.2-4 Images of CFs (a) before testing and (b) after testing.

Figure 4.2-5 Dynamic vapour adsorption and desorption of pristine and ASP treated CFs within 20 hours at room temperature (25 °C).

Figure 4.2-6 Dynamic vapour adsorption and desorption of aged pristine and ASP treated CFs (after 60 days) within 20 hours at room temperature (25 °C).

Figure 4.2-7 Average moisture absorption content of pristine, ASPN5 and ASPAr5-10% treated CFs at 25 °C and 60 °C.

Figure 4.2-8 Weibull plots and linear fits for all groups of CFs.

Figure 4.3-1 SEM observation of Nano-indentation tests on fibres and resin.

Figure 4.3-2 Typical loading-unloading curves (above) recorded from push-out tests and the corresponding SEM images of the indents positions (below).

Figure 4.3-3 SEM image of pushed-out fibre with conical indenter imprint in its centre of top surfaces.

- Figure 4.3-4 SEM observation of the push-out tested composite specimen from a) top view and b) back view of the pushed-out CFs.
- Figure 4.3-5 Sequence of cross-section preparation by Focused Ion Beam technique and the cross-sectional view of a pushed-out CF disc.
- Figure 4.3-6 Schematic diagram and typical load-displacement curve of a push-out test.
- Figure 4.3-7 Experimental load-displacement curves of pushed-out CFs taken from composites made with a) pristine CFs ($h = 39.1 \mu\text{m}$), b) ASPN5 CFs ($h = 31.2 \mu\text{m}$) and c) ASPAr5-10% CFs ($h = 36.4 \mu\text{m}$).
- Figure 4.3-8 Post observations of pushed-out CFs taken from composites made with a) pristine CFs, b) ASPN5 CFs and c) ASPAr5-10% CFs.
- Figure 4.3-9 Weibull probability plots and linear fits for the push-out tests data taken from the composites made with pristine, ASPN5 and ASPAr5-10% treated CFs.
- Figure 4.3-10(a) Typical load-displacement curves for different peak loads and (b) (c) (d) the displacement of the indenter at peak load against the increment of time at dwelling period.
- Figure 4.3-11 The displacement of the fibre/matrix system at peak loads of 8 mN and 10 mN against the increment of time at dwelling period.
- Figure 4.3-12(a) Maximum creep deformation and (b) creep rate of the fibre/matrix system for a 9 μm thick composite sheet with peak loads of 8 mN and 10 mN.
- Figure 4.3-13 Load-displacement curves for push-out tests of 9 μm composites with ASPAr5-10% modified CFs.
- Figure 4.4-1 Images of the pristine and the ASP treated carbon fabrics.
- Figure 4.4-2 Flexural strength and ILSS of the woven fabric/epoxy resin composites with pristine, ASPN5 and ASPAr5-10% modified carbon fabrics.
- Figure 4.4-3 SEM side-view images of fracture surfaces of composites with pristine and ASP modified carbon fabrics.

- Figure 4.4-4 Load-crack opening displacement curves for the produced composite laminate with (a) pristine carbon fabrics and with (b) ASPN5 carbon fabrics.
- Figure 4.4-5 The average initial fracture toughness and the average steady-state toughness for pristine and ASPN5 carbon fabric reinforced composites.
- Figure 4.4-6 SEM images of fracture morphologies for composite laminates with pristine and ASPN5 carbon fabrics after Mode I interlaminar fracture tests.
- Figure 4.4-7 Images of (a) (c) tanks manufactured with (b) (d) pristine CFs and ASPN5 treated CFs.
- Figure 5.1 Schematic mechanisms of (a) conventional plasma treatment and (b) active screen plasma treatment.
- Figure 5.2 Illustration of the energy levels of active species in the plasma and the strength of chemical bonds found in CFs [129].
- Figure 5.3 Variation of structural disorder parameter I_D/I_G , surface crystalline size La and tensile load of carbon fibres as a function of various carbon fibre treatments. (UNT-untreated; YBF3-nano ytterbium fluoride particles treated) [189].
- Figure 5.4 Reynolds and Sharp mechanism of tensile failure in misoriented crystallite [191].
- Figure 5.5 Schematic diagrams of interfacial failure mode of ASP CF/epoxy matrix and pristine CF/epoxy matrix.
- Figure 5.6 Schematic diagram of interfacial bonding mechanisms of ASP CF/epoxy resin.

List of Tables

- Table 3.1 Documented properties of HTA40 carbon fibres.
- Table 3.2 Documented properties of three-part resin system at 25 °C.
- Table 3.3 Active screen plasma treatment conditions and the corresponding sample codes.
- Table 4.1-1 Diameters of the pristine and ASP treated CFs.
- Table 4.1-2 Positions and widths of the D and G bands and the corresponding I_D/I_G ratio (standard deviations given in brackets).
- Table 4.2-1 Degradation rates on contact angle of different ASP treatments after 10 days.
- Table 4.2-2 Summary of DVS tests for freshly treated and aged pristine, ASP treated CFs.
- Table 4.2-3 Summary of results from the Weibull analysis of single fibre tensile tests.
- Table 4.2-4 Tensile strength of CF bundles.
- Table 4.1-3 XRD structure parameters (standard deviations given in brackets).
- Table 4.1-4 XPS chemical quantification of pristine and ASP treated CFs.
- Table 4.3-1 Average interfacial shear strength and Weibull parameters for pristine, ASPN5 and ASPAr5-10% CFs reinforced composites.
- Table 4.3-2 Creep maximum deformation and creep rate of the fibre/matrix system.
- Table 4.4-1 Tensile, shear and flexural strengths of composites reinforced with unidirectional pristine and ASPN5 treated CFs.
- Table 4.4-2 Calculated destructive pressure and average strain values in different sections of the tank manufactured with pristine and ASPN5 treated CFs.
- Table 5.1 Summary of properties of single fibres, interfaces and composites under optimised ASP treatments condition.
- Table 5.2 Surface crystalline dimensions, structural disorder ratio and tensile strength of pristine and ASP treated CFs.
- Table 5.3 The atomic diameter and ionic diameter of H, N and Ar elements [193].

Nomenclature

Symbols

a	delamination length
b	specimen width
d	diameter
F	load where
F_{max}	maximum load
F_t	breaking load
G_{IC}	critical energy release rate
h	thickness
I_D/I_G	intensity ratio of the D to G Raman bands
K	Scherrer constant
K_B	Boltzmann constant
L	span length
L_c	crystallite height
L_a	crystallite width
m	Weibull modulus
M_{ad}	average mass of adsorption process
M_{de}	average mass of desorption process
M_d	dry weight
P	pressure
P_f	failure probability
r	fibre radius

T	temperature
T_d	linear density of fibre yarn
β	FWHM of the diffraction peak
δ_0	reference tensile strength (Weibull scaling parameter)
δ	tensile strength
θ	diffraction angle
λ	wavelength of radiation
ρ	fibre bulk density
σ	load displacement
σ_t	ultimate tensile strength
σ_s	interlaminar shear strength
σ_f	flexural strength
τ_0	reference shear strength (Weibull scaling parameter)
τ	shear strength
Δ	rotation correction

Acronyms

ASP	active screen plasma
AFM	atomic force microscopy
BMI	bismaleimide
CD	corona discharge
CF	carbon fibre
CFRC	carbon fibre-reinforced composite
CNT	carbon nanotube
CVD	chemical vapour deposition
CVI	chemical vapour infiltration
DBD	dielectric barrier discharge
DC	direct current
DCB	double cantilever beam
DVS	dynamic vapour sorption
EPD	electrophoretic deposition
FIB	focused ion beam
FESEM	field emission scanning electron microscopy
FWHM	full width half maximum
FTIR	fourier transform infrared spectroscopy
ICVD	injection chemical vapour deposition
IFSS	interfacial shear strength
ILSS	interlaminar shear strength
LPP	low-pressure plasma
MBT	modified Beam Theory

MW	microwave
OES	optical emission spectroscopy
PAN	polyacrylonitrile
PTFE	polytetrafluoroethylene
RF	radio frequency
RTM	resin transfer moulding
SERS	surface enhanced Raman scattering
UV	ultraviolet
VIS	visual initiation value
XPS	x-ray photoelectron spectroscopy
XRD	x-ray diffraction

CHAPTER 1 INTRODUCTION

Carbon fibres (CFs) acquire the pioneering position in structural application due to their outstanding mechanical properties, high strength to weight ratio and high thermal stability. Considering their high specific strength, CF reinforced polymer composites are gradually replacing other conventional materials in automotive, civil construction, rail, aerospace, aviation and off-shore applications [1, 2]. It is well-known that CFs are used as reinforcements in composites provided the stress applied to the substrate can fully transfer to the CFs. However, because of the chemical inertness and low free energy of CF surfaces with high density graphitic basal planes, the CF/matrix interfacial bonding is not strong enough to fully transfer the stress from the matrix to the CFs [3]. Therefore, further increase in the performance of CF-reinforced composites is mainly restricted by the low CF/matrix interfacial shear strength.

Extensive researches have been conducted into the physic-chemical interaction between carbon fibre and the matrix and a range of surface engineering methods were studied aiming to enhance CF/substrate interfacial strength, such as chemical/electrochemical oxidation [3, 4], plasma treatment [5, 6], polymer grafting [7], sizing and nanoparticle coating [8-10]. All these techniques aimed to modify the surface morphology of the carbon fibres, to introduce new chemical groups to the carbon fibre surface and to change the surface free energy and hence to improve the CF/matrix interfacial bonding. For instance, chemical oxidation generally etched the fibre surface and grafted carbonyl and hydroxyl groups on the fibre surface, resulting in an improved CF/matrix bonding. However, it has been widely recognised that although chemical and electrochemical oxidation treatments can increase the

fibre/matrix interfacial strength, the strength of the treated single fibre significantly was reduced mainly due to fibre surface damage.

Plasma treatment is attractive, owing to its less-destructive, economic advantages and environmental benefits [11-13]. However, conventional plasma treatments can be harmful to the fibre strength mainly due to the direct plasma damage [14]. Recently, an advanced plasma technology, active screen plasma (ASP) technology has been developed, based on the principles of glow discharge plasma and post plasma, to avoid the undesirable effects associated with conventional direct plasma treatment such as arcing, edge effect and hollow-cathode induced damage [15]. In such a novel process, the entire workload is surrounded by a metal screen, on which a high voltage cathodic potential is applied. Thus, the plasma is generated on the metal screen rather than on the samples to be treated as in the conventional plasmas treatments and the samples to be treated are at a floating potential. This setting allows more control over the physical and chemical interactions between the plasma and sample surfaces [16].

Therefore, this PhD project was directed at exploring the potential of active screen plasma technology for the surface modification of carbon fibres to improve their adhesion to epoxy matrix and the mechanical property of resulting CF-reinforced composites. The specific objectives of this research were:

- To identify optimal active plasma treatment conditions for carbon fibre surface modification.
- To fully characterise the morphology, structure, chemical composition, wettability and tensile property of active screen plasma modified CFs.
- To develop advanced testing methods for measuring the interfacial shear strength

between carbon fibre and the epoxy matrix.

- To evaluate the mechanical performance of the composites reinforced with active screen plasma modified CFs.

For a quick overview, the purposes of the chapters of the thesis are outlined below:

- **Chapter 2** gives a survey of the literature starting from the discovery, manufacturing, structure and property of CFs, to the introduction of the CF-reinforced composites and the interface between the CF and the matrix, followed by a review of the state-of-the-art surface modifications for CFs.
- **Chapter 3** describes the materials, treatments and all the characterisation and testing methods.
- **Chapter 4** presents all the results and their interpretation, covering the general characterisation and the promising property of CFs, interface evaluation and mechanical properties of CF-reinforced composites.
- **Chapter 5** discusses four topics, covering 1) the mechanisms involved in ASP surface modification of CF and the effects of ASP modification on 2) the tensile property of CFs, 3) the CF/resin interface and 4) the CF-reinforced epoxy composites.
- **Chapter 6** concludes the key findings and implications of this research.
- **Chapter 7** provides suggestions for future scientific work.

CHAPTER 2 LITERATURE REVIEW

2.1 History and development of carbon fibre

Carbon fibre (CF) is a kind of material with a fibrous shape containing at least 92 wt. % of carbon in composition [17]. It has been heralded as the new wonder material, especially as an extremely useful reinforcement material. CFs were first recorded by Thomas Alva Edison in 1877. He converted cotton threads and bamboo strips into CFs and patented their use as filament materials for the electric lamp [18]. After that in 1889, Hughes and Chambers [19] patented a process to produce carbon filaments. Hair-like carbon filaments were obtained but the process was uneconomic. In 1909, Whitney [20] heated a product, which comprised of an impure carbon at the core and a pyrolytic carbon in the outer layer, to over 2300 °C. The outer layer of pyrolytic carbon was converted to a more graphitic form and the final product obtained enhanced electrical properties. However, all of the carbon filaments produced by the early inventors were very weak or brittle.

Since the early work of Edison, many studies for producing CFs have taken place in the following decades. Graphite whiskers with 20 GPa tensile strength and 700 GPa modulus were reported by Bacon in 1958 [21, 22]. Synthetic rayon was carbonised to form carbon-like fibres at nearly the same time. But highly scalable commercial use of CF only began after the introduction of polyacrylonitrile (PAN) as the precursor of CFs by Akio Shindo in Japan in the 1960s [23]. This approach turned out to be economically more favourable due to its combination of physical and chemical properties, as well as the fibre yield. Shindo's [24] patent was industrialised in 1970 by Toray and continuous PAN-based Torayca T300 and M40 CFs were manufactured just a year later. The tensile strength of the T300 CFs was further increased by Toray, from 2.45 GPa to 3.30 - 3.43 GPa, in 1985. High-

performance PAN-derived CFs were developed by Toray simultaneously, such as T1000 with a tensile strength of 7.06 GPa and a tensile modulus of 295 GPa [24]. At nearly the same time, Hexcel Corp. Inc developed the IM6, IM7 and IM8 intermediated modulus CFs with the Exlan PAN precursor [25]. Parallel studies were conducted to produce CFs from pitches obtained from petroleum, coal tar, asphalt, etc. Otani in Japan produced the first pitch-derived CF using polyvinyl chloride pitch as the raw materials in 1965 [26] and developed the mesophase pitch-derived CF in 1971 [27]. Since then, many attempts were made to produce CFs from mesophase pitch, with commercialisation being finally achieved in the 1980s. Pitch-derived CFs demonstrate much higher modulus (up to 900 GPa) and better electrical and thermal properties than PAN-derived CFs [28]. However, the production process of pitch-derived CFs has been shown to be more expensive when compared to that for PAN-derived CFs. Increasing number of manufacturers entered the CF production industry in the late 1980s and early 1990s [25], resulting in various types of CFs with different mechanical properties.

Currently, the annual worldwide production of CFs has increased from 20 million kg in 2002 to 90 million kg in 2018, with about 90% of the CFs being derived from PAN precursor [29]. The annual production is projected to be doubled to 180 million kg by 2025, with the growing demands from the wind energy, transportation and aerospace markets. Although it has significantly reduced since the 1980s, the production costs of CFs are still one of the major barriers to its further growth and uptake. Currently, the price of CFs is in the range of \$66 /kg to \$176 /kg for the aerospace industry, and in the range of \$22 /kg to \$44 /kg for other applications, such as the automotive industry, sporting goods and wind energy [30]. Therefore, it is expected that the low-cost-high-performance CF technologies should be developed to further expand the production and usage of CFs.

2.2 Carbon fibre manufacturing, structure and property

2.2.1 PAN-derived CF manufacturing

Polyacrylonitrile (PAN), which contains 68 wt. % carbon, is currently the predominant precursor for CF manufacture [31]. Typically, the production of PAN-derived CFs involves the polymerisation of acrylonitrile and its comonomers, spinning to obtain the precursor fibres, stabilisation by oxidation in air at moderate temperatures, and subsequent carbonisation or graphitisation in an inert environment at high temperature (Figure 2.1).

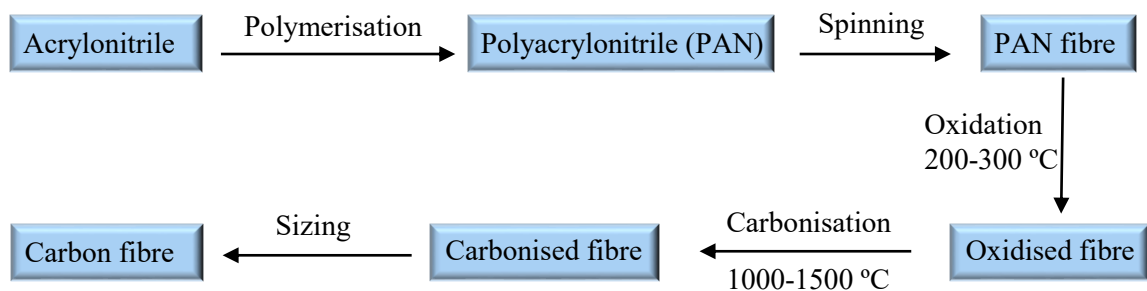


Figure 2.1 PAN-derived CF production process.

2.2.1.1 Polymerisation

Solution polymerisation and suspension polymerisation are the most typical commercial methods for producing PAN precursors. The solution polymerisation is usually conducted in a PAN solvent, so that after removing the unreacted monomers in the solution, the produced PAN solution can be directly used as the fibre spinning dope for the next CF manufacturing step. The PAN drying and re-dissolving processes can be avoided [32]. However, the molecular weight of the PAN/PAN copolymer produced with the solution polymerisation process is usually low. In comparison with solution polymerisation, the suspension polymerisation process produces linear PAN polymers with higher molecular

weights. However, post-processing steps involving washing, drying, milling and dissolution of the polymer powder into a suitable solvent are required in the suspension polymerisation process [33]. This arises due to the strong intermolecular interactions that exist in the molecules of the linear PAN polymer. Therefore, nearly all industrial PAN precursors are made from copolymer containing 2 - 15% comonomers, such as acrylic acid, methacrylic acid, itaconic acid, methacrylate, acrylamide, vinyl acetate, vinyl bromide and/or quaternary ammonium [34]. The use of these comonomers contributes to disrupt the intermolecular interactions and hence improve the dissolution process and the processability of PAN precursor fibres [35]. Meanwhile, the incorporation of comonomers produces CFs with improved performance due to the increased molecular alignment in precursor fibres [35, 36].

2.2.1.2 Fibre spinning

Traditional spinning techniques for PAN fibres include wet spinning, dry spinning, dry-jet wet spinning, gel spinning and melt spinning [28]. Amongst them, wet spinning is the most widely used technique, within which the polymer solution is directly extruded into the coagulation bath with a submerged spinneret and the fibres are subsequently drawn at ~ 100 °C [37]. Wet-spun PAN fibres typically have a core-shell structure because of the counter diffusion of bath solvent, leading to polymer precipitation at the surface of PAN fibres. As a result of this, a thin, dense and homogenous skin with a thickness of 200-300 nm is formed, which in turn hinders the counter diffusion process to form a loose and disordered core. Such core-shell structure of the PAN fibres is believed to affect the structure and mechanical properties of resulting CFs [37, 38].

The melt spinning process has been utilised to reduce the processing cost as no solvents are required. However, diluent or suitable copolymers are indispensable for reducing the nitrile-

nitrile interactions between PAN molecules. Subsequently, relatively low mechanical properties of the final PAN fibres are inevitable due to the surface defects and internal voids formed by this method [39]. The final mechanical properties of PAN fibres produced from the gel spinning technique outperform those produced using the other fibre spinning techniques mentioned above [36, 40].

2.2.1.3 Stabilisation and carbonisation

Conversion of the PAN fibres into CFs involves two heat treatments, namely stabilisation and carbonisation. The PAN fibres are stabilised under stress at temperatures ranging from 200 °C to 300 °C in an oxidative environment for about 2 hours. The stabilisation process contributes to preventing the PAN fibres from melting or fusing when the temperature is further raised. Then the stabilised fibres are carbonised under tension in an inert environment (N₂) at high temperatures in the range of 1000 - 1700 °C [41, 42]. The key parameter during the carbonisation process is the gradient of the temperature, which is required to be kept low at the beginning to avoid destruction of the high degree of molecular order in the fibres [42]. The non-carbon elements, such as hydrogen, oxygen and nitrogen, are removed during these heat treatments and thus the carbon content of the carbonised fibres increases to over 90% [43]. Compared with the precursor PAN fibres, the tensile strength of the fibres increases and the fibre diameter decreases from approximately 15 µm to about 7 µm. Carbonised fibres can be further heated at very high temperatures of up to 3000 °C in an inert environment for graphitisation to further increase the carbon content and improve the fibre texture, and this consequently raises Young's modulus in the fibre direction [41, 44]. The structure development during the stabilisation and carbonisation processes of the PAN fibres is shown schematically in Figure 2.2 [45]. The linear PAN molecules are firstly

converted to a rigid, thermally stable ladder structure by cyclisation during the stabilisation step. Then, the hydrogen atoms are expelled from the carbon atoms to form aromatic pyridine groups when the temperature is elevated at the early stage of the carbonisation process. The stabilised ladder structures start to link up in the lateral direction to form ribbon-like structures by expelling more hydrogen atoms. When the temperature is increased to 600-1300 °C, the adjacent ribbon-like chains fuse together to form a planar structure by further expelling nitrogen atoms. These basal planes are oriented parallel to the fibre axis to form CF [46].

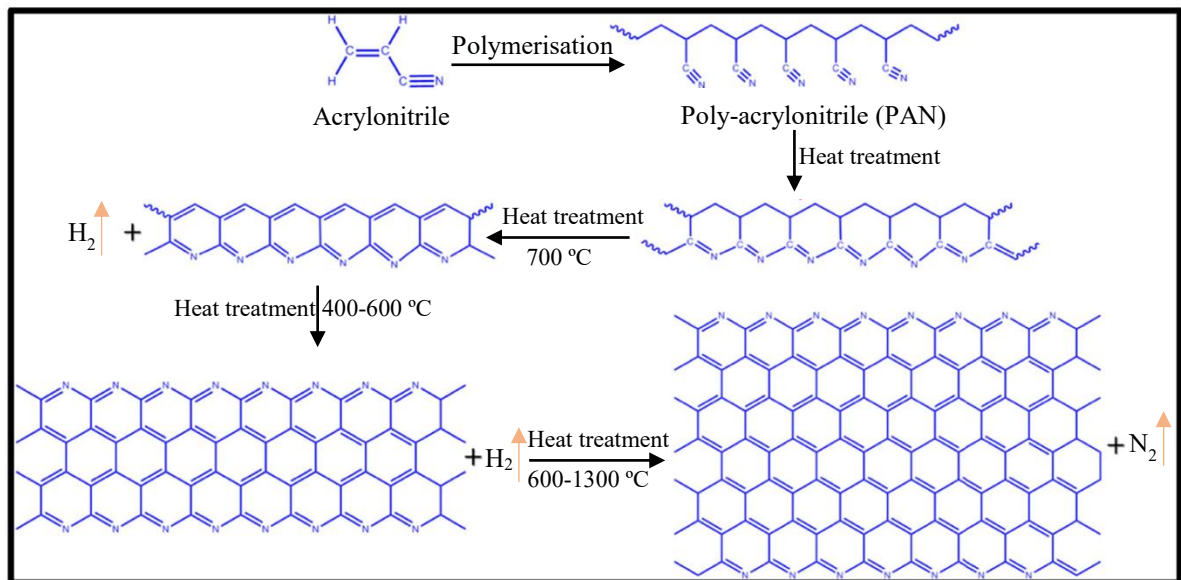


Figure 2.2 Chemical reactions during the stabilisation and carbonisation of PAN-derived CFs [45].

2.2.1.4 Sizing

The sizing process is conducted immediately after cooling from carbonisation, aiming to protect fibres from fluffiness and damage during manufacturing and usage and to provide a surface that is compatible with the matrix used in resulting composites [47]. Normally, the CFs are sized (generally, 0.5 - 1.5% by weight) by contacting an applicator roll carrying a

layer of an aqueous mixture of coupling agents, lubricants, emulsified polymers, etc. [48]. The sizing material forms a protective film after drying on the surface of filaments and thus protects the filaments from damage. Commonly used sizing materials include polyvinyl acetates, polyurethanes, polyolefins, polyesters, epoxies and modified epoxies [49]. However, the actual composition of sizing formulation is usually complex, multicomponent and confidential.

Furthermore, sizing for CFs can promote the fibre impregnation and bonding with the matrix, which will improve the mechanical properties of the end products, such as compressive strength and interlaminar shear strength [50].

2.2.2 Pitch-derived CF manufacturing

Pitch-derived CFs can be fabricated by both isotropic and mesophase pitches, which are produced by destructive distillation of petroleum or coal tar which is composed of the fused aromatic ring [51]. Normally, general-purpose grade pitch-derived CFs are obtained from petroleum and coal tar due to their isotropic structure in nature [51]. Mesophase pitch is converted from an isotropic pitch by pyrolysis at the temperature between 300 °C and 500 °C, resulting in an anisotropic phase of pitch consists of disc-like aromatic molecules [52]. This conversion makes the mesophase pitch capable of producing high mechanical performance pitch-derived CFs.

Similar to the manufacturing process of PAN-derived CFs, the production of pitch-derived CFs involves melt spinning of pitch precursor fibres, stabilisation, carbonisation graphitisation and sizing [53]. After purification, both isotropic pitch and mesophase pitch can be melt spun into continuous fibres. The spinning temperature is vital to the microstructure of the pitch fibres because of the temperature-dependence of the pitch

viscosity [52]. It was reported that the transverse microstructure for mesophase pitch fibres transitioned from a cracked radial texture to a concentric onion skin texture when the spinning temperature increased [54]. The microstructure of mesophase fibres has also been shown to be affected by the spinneret hole, which also controls the shape of the fibres [55]. Mesophase pitch fibres are stabilised in air at temperatures between 250 °C and 350 °C, and then immediately carbonised in an inert atmosphere at temperatures between 800 °C and 1200 °C. Increasing the temperature of carbonisation results in pitch-derived CFs with increased tensile strength and tensile modulus. The carbon yield for pitch-derived fibres is the highest of all the precursors [54].

2.2.3 Structure, morphology and properties of CF

2.2.3.1 Microstructure and morphology

Carbon fibres are fibres having a diameter in the range of 5 - 10 μm and containing at least 92% carbon in composition. The microstructure of CFs consists of hexagonal graphene layers, in which some of them are distorted irregularly due to the weak interaction between the graphene layers, resulting in the formation of a turbostratic structure, as shown in Figure 2.3 (a) [56, 57]. This turbostratic structure is considered to be the basic structural unit of CFs, which can join, fold, twist and split with each other to form various types of micro-region within the CFs (Figure 2.3 (c)) [58]. Therefore, the distance between the turbostratic planes of the CFs increases by 2.6% to 3.44 Å, compared to the distance between perfect graphite planes of 3.35 Å [57]. In addition, PAN-CFs exhibit a skin-core structure which has been confirmed by scanning electron microscopy [59]. The outer skin shows a highly orientated turbostratic structure and tends to be circumferential while the core shows much less organised structures (Figure 2.4 (a)). This structural heterogeneity is associated with the

coagulation condition during the PAN precursor fibres spinning process [60]. On the other hand, pitch-derived CFs usually display a typical radial wedge structure, in which the graphene planes fan out from the centre of the fibre (Figure 2.4 (b)) [54, 61].

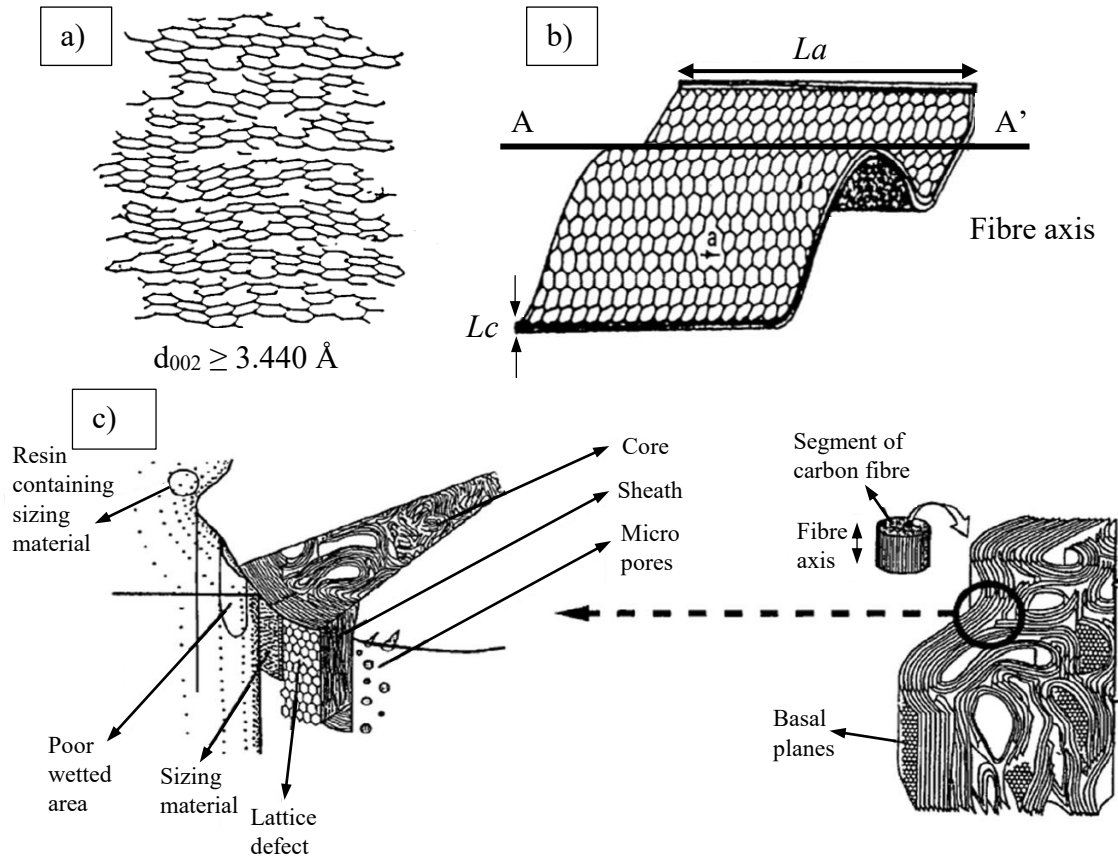


Figure 2.3 (a) Unit cell of the turbostratic structure (b) Structural unit of the crystallites in CFs (A-A' is the fibre axis direction) and (c) Schematic diagram of the microstructure of PAN-derived CF.

Qin *et al.* [62] investigated the evolution of the microstructure during high-temperature heat treatments of both kinds of CFs with TEM. Their results illustrated that a turbostratic structure was formed by wrinkled and entangled crystallites at 1300 °C graphitisation for PAN-derived CFs. When increasing the temperature, larger unwrinkled crystallites gradually appeared, and a locally ordered but overall disordered structure was formed. On

the other hand, the ordered graphitic planes in pitch-derived CFs were still parallel to each other and ran in the radial direction without mutual entanglements.

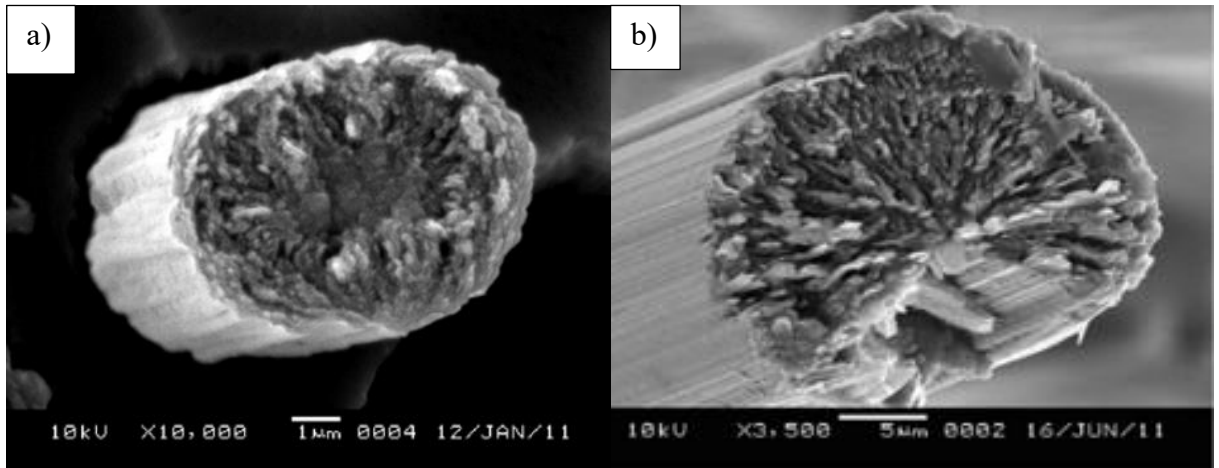


Figure 2.4 SEM micrographs of the cross-section of (a) PAN-derived CF and (b) pitch-derived CF.

TEM micrographs also reveal the presence of various defects in between the crystallites of both kinds of CFs [62], such as micro-pores, dislocations, and vacancies, which are formed by the enclosing of the distorted crystallites. When the CFs are subjected to higher-temperature graphitisation, the micro-porosity tends to decrease while the size of the micropores increases. Qin *et al.* [62, 63] reported a similar evolution of the micro-porosity for pitch-derived CFs. However, they observed that the micro-porosity for PAN-derived CFs firstly increased before the temperatures were elevated to 2000 °C and then decreased. They attributed the differences to the various structure evolutions based on the original structure. Another type of defect is surface flaws which are normally introduced during the spinning process of the PAN fibres (for example, adjacent fibres sticking together) and retained after carbonisation, resulting in misaligned graphite basal planes at the fibre surfaces.

The crystalline size and orientation in the structure of CFs can be detected by wide-angle X-ray diffraction [64]. As shown in Figure 2.3 (b), the geometry of the crystallite is defined

with the average layer plane length, L_a , and the average thickness of the parallel layers, L_c . The values of L_a and L_c can be calculated by a method proposed by Biscoe and Warren [65], in which the value of L_a is derived from the (100) and (110) XRD planes' reflections and the value of L_c is determined from the (002) and (004) XRD planes. The orientation of the (002) basal plane can be determined from the azimuthal scan of the (002) plane. Generally, high-modulus pitch-derived CFs possess larger crystalline sizes and higher orientation than PAN-derived CFs. Additionally, the crystallite size, as well as the orientation of the crystallites, is expected to increase with increasing graphitisation temperature. A more ordered structure is presented in CFs after higher temperature graphitisation, in which more crystallite growth is observed for pitch-derived CFs.

2.2.3.2 Properties of carbon fibre

2.2.3.2.1 Tensile properties

The tensile properties of CFs are related to their microstructure and morphology, which vary with the processing conditions. The high tensile modulus of CFs comes from the high degree of crystallinity and the good alignment of the crystallites in the fibre direction. Meanwhile, the tensile strength of the CFs is primarily affected by the presence of structural defects, either on the fibre surface or within the fibre internal structure [63]. Therefore, pitch-derived CFs usually show higher tensile modulus than PAN-derived CFs due to their larger crystallite size and the higher crystalline orientation. However, larger crystallites also lead to higher stress concentrations at the edge of the pseudo-crystallites, and the extended graphitic structure makes the pitch-derived CFs more sensitive to defects. Moreover, the entanglements of the carbon ribbons in the turbostratic structure of the PAN-derived CFs contribute to developing a large shear modulus between layer-planes. Hence, PAN-derived

CFs generally offer a higher tensile strength than pitch-derived CFs. Both tensile modulus and tensile strength of PAN-derived CFs and pitch-derived CFs increase with increasing the graphitisation temperature. The increased tensile modulus is attributed to the increased crystalline size and the better orientation of the crystallites. The improved tensile strength directly correlates with decreased micro-porosity density [66].

2.2.3.2.2 Compressive property

Owing to the weak Van der Waals forces between the graphene layers, CFs usually exhibit low axial compressive strength, which decreases with increasing modulus [67]. Thus, PAN-derived CFs offer a higher axial compressive strength than pitch-derived CFs [67, 68]. The compressive failure mode of CFs has been investigated using a single-fibre-recoil test by Dobb *et al* [69]. They observed that PAN-derived CFs buckled on compression and formed kink bands at the innermost compression side. A tensile crack was initiated on the tension side when increasing the compressive force, and then propagated inwards. The fibres finally failed when the tensile crack propagated transversely across the fibre, and the kink bands propagated inwards along the opposite direction across the fibre, simultaneously. While high modulus pitch-derived CFs failed by a shear mechanism, where kink bands were formed at 45 ° angle to the fibre axis because of the high orientation of the graphene layers.

2.2.3.2.3 Thermal conductivity and electrical conductivity

CFs display good thermal and electrical conductivities in the fibre direction as a result of the high density of electrons and phonon, as well as the parallel arrangement of graphene layers along the fibre axis. The thermal and electrical conductivity of commercially available PAN-derived CFs at room temperature are in the range of 5 - 156 W/m.K and 10^4 - 10^5 S/m respectively, while that of the pitch-derived CFs is in the range of 200 - 1000 W/m.K and

$10^5 - 10^6$ S/m [70]. The concentration of the point defects, including vacancies, interstitial atoms, and impurities, as well as the crystalline perfection and orientation affect the longitudinal thermal and electrical conductivity. Increasing the carbonisation temperature reduces the concentration of point defects and increase crystalline perfection, resulting in improved thermal conductivity [63, 71]. The improved crystalline orientation allows greater electron movements along the fibre direction, leading to an increased electrical conductivity as well. However, the presence of defects increases the local electrical resistivity, thereby lowering the electrical conductivity. It should be noted that the CFs possess a small but negative coefficient of linear thermal expansion in the fibre axial direction due to the high crystalline alignment in the structure, which can cause residual stresses at the interface of the resulting composite when temperature changes [72]. Furthermore, by increasing the carbonisation temperature it is possible to further improve the electrical and thermal conductivities [66].

2.3 Carbon fibre-reinforced composites (CFRCs)

Composites are fabricated to take advantages of each component and achieve desirable properties through the combination of the different components. Currently, composites are gradually becoming a valuable alternative to conventional materials in various fields, mainly due to their high mechanical properties, strength to weight ratio and damage tolerance. Composites can be designed by dispersing high-performance fibres or partials into a matrix (polymer, metal, ceramic or carbon), which acts as a binder and transfer forces to the fibres across the interface, to yield properties unobtainable by either the reinforcing material or the matrix exhibits. Therefore, composites show potential for fulfilling the requirements of advancing technologies that require a combination of properties. Typically, the strength and stiffness of composites mainly rely on the reinforcing material, but the ability to conduct heat and current is heavily influenced by the conductivity of the matrix. CFs, glass fibres, ceramic fibres and aramid fibres are commercially available reinforcing materials for different structural applications. Among these fibres, CFs are competitive as a reinforcing material due to the superior properties they possess, as discussed in Section 2.2.3.2, especially in regards to their compressive strength, which is the most important parameter for structural applications [73]. Additionally, CFs exhibit the lowest coefficient of thermal expansion, therefore giving them improved dimensional stability and extended applications in comparison to the other reinforcement materials [74]. The commercially available CFs used for composite fabrication are mainly short and continuous CFs. Composites reinforced by continuous CFs have higher mechanical properties than by short CFs, whereas short CFs-reinforced composites are superior for making components for low-cost commercial structural applications. The most common type of matrix materials used for composite fabrication is polymer-based, and this arises due to their light weight and low processing

temperature [75]. Thermoset polymeric matrices (mainly epoxy) have been extensively used for commercial applications due to their ease of handling, low-cost and adaptable properties (ability to balance mechanical, chemical and electrical properties). All of these confer the composites with high performance, long durability, and low cost on maintenance.

2.3.1 Fabrication process for composites

There are several methods for fabricating fibre-reinforced composites. The selection of the method depends on the selection of the constituents, the part design and the end-use application.

2.3.1.1 Hand lay-up

Continuous CF composites are commonly prepared by hand lay-up technique, in which either the unidirectional fibre tapes or woven fabrics are impregnated with a resin and then placed into a mould. High pressure or vacuum is employed to force the individual piles together and reduce voids during the curing process. This technique is used commercially to fabricate the skin of aircraft components [76].

2.3.1.2 Resin transfer moulding (RTM)

Resin transfer moulding can be used to produce continuous fibre composites of intricate shapes, and it is one of the suitable techniques that can fulfil the current market requirements. The flow diagram of the RTM process is shown in Figure 2.5, the first step of the process is to place the required shape into the cavity of the preform tool. After closing the mould, the resin is then injected under pressure into the mould cavity, where the braided fibre has already been placed. Finally, the material is cured, cooled, and taken out [77]. This method

has a short production cycle, a large production rate, and can produce intricate parts for applications in the aerospace, civil and automobile industries.

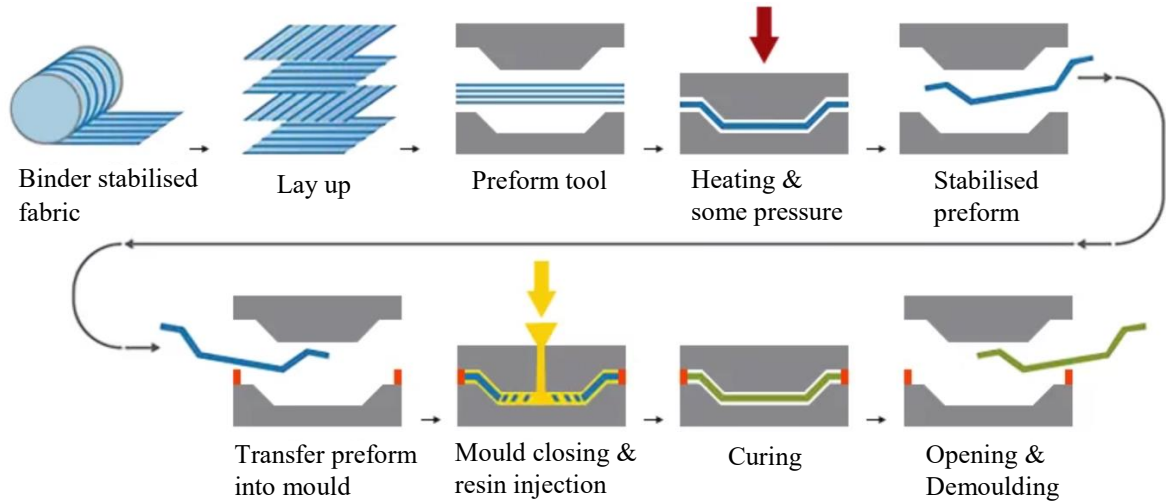


Figure 2.5 Sequence of main steps of RTM process [77].

2.3.1.3 Pultrusion

The pultrusion technique is used for making unidirectional fibre-reinforced composites, in which the fibres are pulled from a creel, dipped through an impregnation bath and then clamped together according to their particular shape before entering into a heated die as shown in Figure 2.6. The die regulates the resin content and cures the combined material into its final shape [78]. This technique is a relatively simple, low-cost and continuous process, which is capable of producing composites with a constant cross-section.

2.3.1.4 Filament winding

The filament winding method is suitable for making hollow, circular or oval sectioned components. Firstly, fibres are gathered into a band by passing them through separator combs. After passing a resin bath, the impregnated fibres are wrapped onto a rotating mandrel through a wiping device that removes the surplus resin from the fibres and controls

the resin coating thickness. The filament wound mandrel is subjected to the curing process and then eject the product. During the curing process, the mandrel needs to be rotated constantly to maintain the uniformity of the resin content. Three typical types of filament winding are hoop, helical and multi-directional winding [79]. The filament winding process is rapid and highly automated, therefore produces a product with a great strength-to-weight ratio, which is important for pressure vessels, aerospace components and military armaments. The schematic of the filament winding process is shown in Figure 2.7.

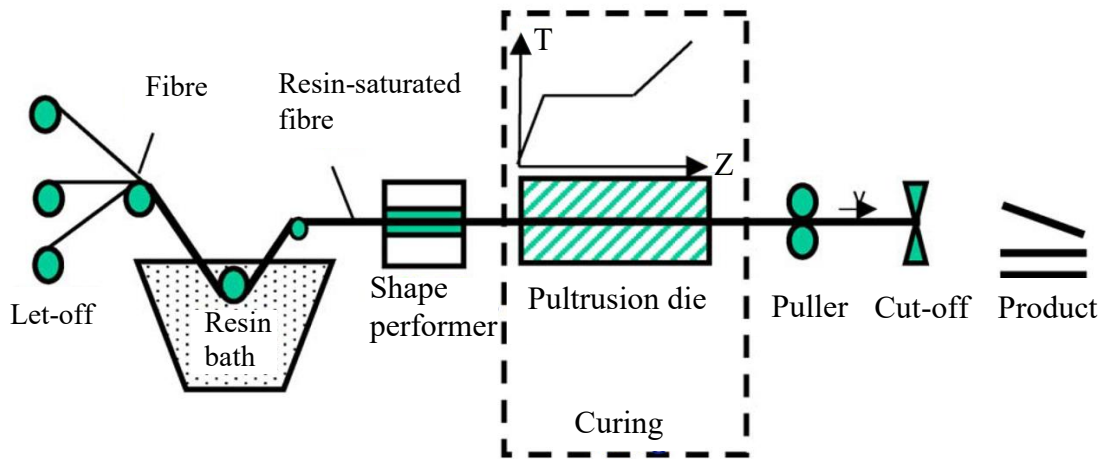


Figure 2.6 Schematic of the pultrusion process for composite fabrication [78].

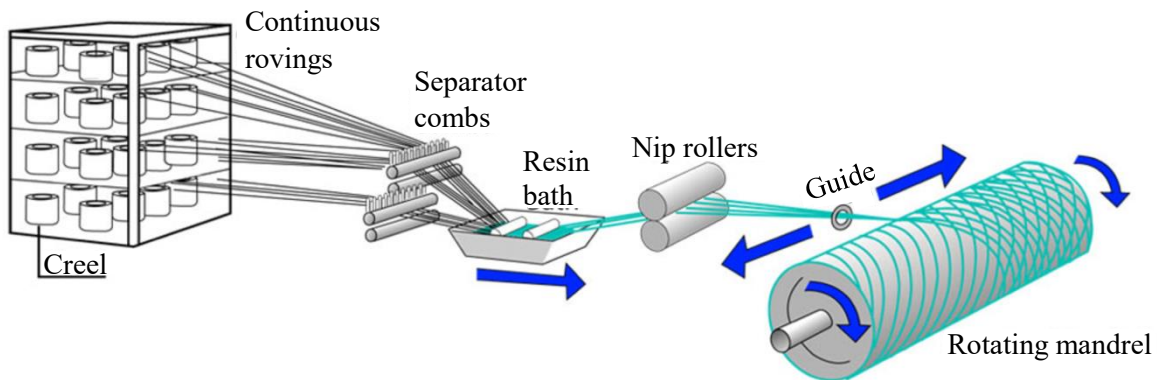


Figure 2.7 Schematic of filament winding process [80].

2.3.2 Properties of CF-reinforced composites

The performance of CFRCs is affected by many factors, including the moduli and strengths of the fibre and the matrix, the aspect ratios, the length distribution, the volume fraction, the uniformity and orientation of the fibres, the integrity of the fibre/matrix interface, and the manufacturing process. Generally, CFRCs possess the following properties [81]:

- light weight and low density,
- high strength and stiffness,
- good creep resistance,
- long fatigue life,
- high abrasion resistance and low coefficient of friction,
- outstanding chemical resistance,
- excellent corrosion resistance,
- great dimensional flexibility and diversity,
- high thermal conductivity,
- low electrical resistivity.

2.3.3 Applications

In the 1960s when CFs were first commercialised, CFRCs were fabricated only for defence aircraft because of their high strength to weight ratio and high manufacturing cost. More recently, they have been used in many structural applications, ranging from parts for aircraft, satellites, components of launch vehicles, fuel tanks, and missiles in the aerospace industry, as well as other areas including automobile, sports, marine, biomedical, construction and other industries [45].

2.3.3.1 Aerospace industry

The aerospace industry remains the dominant market for CF-based composites, where the high strength to weight ratio, thermal stability, high stiffness and good fatigue resistance have always been the key performance criteria for materials within these applications. CFRCs are used extensively in aircraft wings, fuselage sections (such as the undercarriage and rear end of the fuselage), tail surfaces and doors. For example, CFRCs make up nearly 50% of materials, by weight, found in a Boeing 787 (on fuselage, wings, tail, doors and interior) [82]. This has offered a weight reduction of 20% over its alternative of aluminium alloys. The high stiffness and excellent thermal stability over a wide temperature range also make CFRCs ideal for space applications. Examples of their use include fairings, manipulator arms, antennae reflectors, solar array panels, and optical platforms and benches. They have also recently been used for the primary structure of spacecraft [83].

2.3.3.2 Automotive industry

In the automotive industry, CFRCs are mainly used for making structural and lightweight components, such as wheels, body panels, engine components, structural members and leaf springs [84]. The main advantages CFRCs offer to automotive applications are excellent crash performance, reduced cost and weight, and recyclability, which meet the European directives and standards for vehicles (The 2000/53/EC End Life of Vehicles) [84]. This provides great incentive, and future potential for further uptake CFRCs in the automotive industry.

2.3.3.3 Sports equipment industry

The applications of CFRCs in sports equipment started very early, and this was the largest market for CFRCs prior to significant uptake for aerospace applications. This is mainly due

to the lightweight structure and excellent stiffness of CFRCs, which enable the production of sports equipment with improved performance. Composite golf club shafts, archery bows, fishing rods, racquets and skis equipment are now well-established products utilising CFRCs. Recent developments include bicycle components and major parts of formula 1 racing cars [85].

2.3.3.4 Construction industry

Owing to their good corrosion and fatigue resistance, and high specific strength and stiffness, the application of CFRCs has also branched into the construction industries, for applications such as load-bearing and infill panels, pressure pipes, tank liners and roofs [86]. Thermosetting continuous CFRCs are hoped to replace steels for making grids used for concrete reinforcement, which can contribute to reducing weight and extending service life. In Japan, thermoplastic-based CF composites are also used to build earthquake-proof buildings [86].

Apart from the mentioned applications, the conducting nature of CFs makes the resulting composites applicable for various fields, such as electromagnetic interference shielding, fuel cells, sensors and conductors [45]. The environmental resistance makes CFRCs a good choice for boat hulls, keels and masts [87]. The biocompatibility of CFRCs can expand its applications in the medical sector [88]. New applications of CFRCs are still developing rapidly.

2.4 Carbon fibre/matrix interface

The performance of CFRCs is governed not only by the original physic-chemical properties of the reinforcing CFs and the matrix, but also by a factor that is distinct for composite materials, the CF/matrix interface which provides composites with structural integrity and efficient load transfer from the matrix to the CFs. An enhanced interfacial bonding has the potential to produce composites with improved properties, such as high ultimate strength and interlaminar shear strength, good resistance to delamination and fatigue, which are essential for structural applications. Composites with less than optimal interfacial adhesion have reduced maximum structural load capabilities, and therefore their applications are more limited.

2.4.1 Introduction of interface

The interface in CFRCs is an interlayer formed by the interaction of the fibre and the matrix for transfer of loads, and whose structure and properties are different from those of the individual bulk fibre or matrix. Herrera-France and Drzal [89] described and expanded the interface from a two-dimensional region based on previous studies to a three-dimensional region that exists between the bulk fibre and the bulk matrix, starting from some point on the fibre, through the actual interface, and into the matrix. In other words, the three-dimensional interface is a region of material affected by the interaction at the interface, including the interlayer between the fibre and the matrix (the actual interface), and the layers of finite thickness extending either side of the interlayer. They used Figure 2.8 to illustrate the complexity of the three-dimensional interface between the fibre and the matrix. Thus, this region has been defined as an interphase by some researchers, for the purpose of

conveying that such interlayer will lead to a gradual rather than abrupt change of properties [90-92].

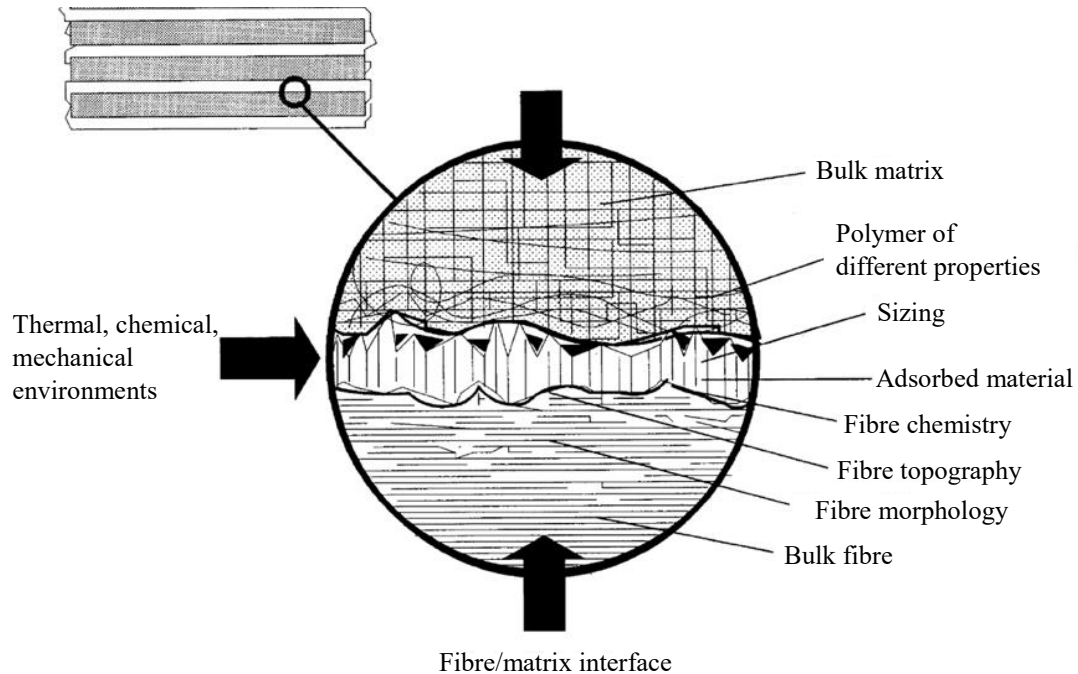


Figure 2.8 Characteristics of the fibre/matrix interface in a composite material [71].

Several mechanisms have been proposed to explain the interfacial adhesion, including adsorption and wetting, interdiffusion, Van der Waals attraction, chemical bonding and mechanical bonding [93]. Chemical bonding is created between the well-matched chemical groups on the CFs and the matrix. The bonding strength is decided by the amount and the type of bonds [94]. The typical functional groups on the CF surface following oxidation include -COOH , C-OH and C=O , which possess good chemical bonding with lots of matrices. The good wettability of the fibre by the matrix is undoubtedly beneficial for the proper consolidation of the composites, where microstructure (mainly roughness and polarity) and free energy of the surface are the key factors that affect the wettability of the fibres [95]. Contact angle measurements are widely used for evaluating the wettability and surface energy of the fibres. Mechanical bonding refers to the interlocking between the fibre

surface and the matrix, which can be promoted by increasing the CF surface area and/or increasing the roughness of the CF surface [96].

2.4.2 Interfacial shear strength (IFSS)

Interfacial shear stress is induced mainly due to the Poisson ratio difference between the ductile resin and the stiff fibre. The elongation at break is about 0.45% for epoxy resin and 0.025% for CF [97]. When the load is applied to the composite, the greater Poisson contraction of the matrix exerts shear forces, gradually building stress onto the fibre through the interface region. If the matrix is well bonded to the fibre, the Poisson contraction of the matrix can be suppressed by the fibre. Furthermore, even when the fibre breaks with the broken ends of the fibre being pulled apart, the fragments continue to contribute some reinforcement to the composite through load transfer. The stress on surrounding intact fibres increases less than it would in the absence of the matrix, and the composite is still able to bear more stress without fracturing. Thus, a good interfacial bonding can strengthen and toughen the composite [97]. In other words, a composite with higher interfacial shear strength shows better mechanical properties. In addition to this, the interface suffers differential thermal expansion, as well as a non-linear stress/strain response of both fibre and matrix, which make the stress pattern at the interface region further complicated [97].

2.5 Characterisation of interfacial adhesion

Many testing techniques have been developed to evaluate the interfacial adhesion in fibre reinforced composites. All such approaches can broadly be divided into two groups depending on the nature of the specimens adopted and the scale of testing. One group encompasses the tests on the micro-composites where the individual fibres are embedded in a matrix to directly examine the interfacial shear strength (IFSS) of an individual fibre, such as micro-bond test [98, 99], single fibre pull-out test [100, 101], three-fibre test [105], single fibre push-out test [102-104] and single fibre fragmentation test [106-108]. The other group employs bulk laminate composites to predict the fibre-matrix adhesion by inference from the gross mechanical properties of CFRCs, such as interlaminar shear strength (ILSS) [4, 109, 110], interlaminar fracture toughness [111], transverse tensile strength [112, 113] and translaminar shear strength [114]. Some of these techniques have now been adopted as ASTM standards [115, 116].

2.5.1 Interfacial shear strength testing

2.5.1.1 Single fibre fragmentation test

The single fibre fragmentation test is one of the most popular microscale experiments used to evaluate the interfacial properties of the fibre/matrix composites. It was developed from the early work of Kelly and Tyson in 1965 [117]. In this test, a single fibre filament is embedded entirely into the middle of the matrix which is shaped into a dog-bone specimen. The elongation percentage of the matrix material must be at least three times greater than that of the fibre filament, so that shearing can occur at the fibre-matrix interface between the stiff fibre and the ductile matrix. When the specimen is elongated along the axis of the fibre by a load applied on the matrix, the embedded fibre will break due to the shear stress

transferred from the matrix. As loading continues, the fibre fragment breaks into smaller lengths at locations where the tensile strain in the fibre exceeds the failure strain of the fibre. The fibre fragments continue to fracture into even shorter lengths until the maximum stress on the fibre fragments can no longer cause any more fibre breakage. This is known as “fragment saturation”, as illustrated in Figure 2.9. The final fibre fragment length, which can be measured with an optical microscope, is referred to as the critical length.

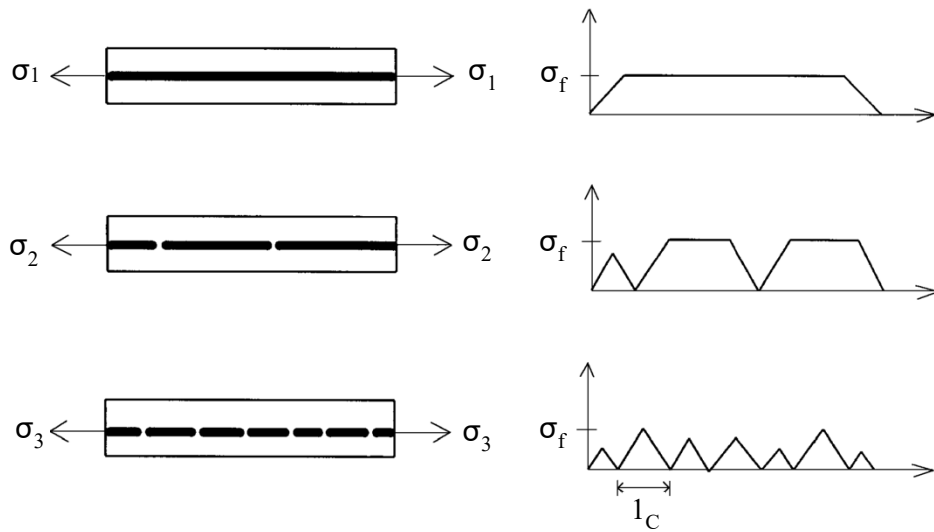


Figure 2.9 Schematic illustration of the single fibre fragmentation test [118].

The Interfacial shear strength (IFSS, τ) can be determined based on the constant shear model proposed by Kelly and Tyson [117]:

$$\tau = K \frac{\sigma d}{2l} \quad (2-1)$$

where K is a correction factor determined from the Weibull/Poisson model, for fibres, a mean value of 0.889 is an appropriate correction factor; d is the fibre diameter, m; σ is the fibre strength, Pa; l is the critical fibre fragment length, m. Although this method is simple and

quantifiable for determining IFSS, some limitations exist with this approach, such as limited matrix material that can be used for this test as it must have an appropriate elongation property; the results could be unduly influenced by the shrinkage pressure which is unrelated to adhesion [106, 119, 120].

2.5.1.2 Pull-out test & micro-bond test

The fibre pull-out test and micro-bond test share some similar characteristics, consisting of a fibre or a filament partially embedded in a matrix box, a thin disc or a droplet (as shown in Figure 2.10). These tests are easy to conduct, but they were developed in the early stages of composite research with thick fibres. In order to pull the fibre out of the matrix, a steadily increasing load is applied axially to the free end of the fibre while the matrix block is gripped. Load and displacement are recorded during the whole de-bond or pull-out process until either fibre fractures, or is pulled out of the matrix. The schematic set-ups of the micro-bond test and pull-out test are shown in Figure 2.10.

The IFSS can be determined using these two methods under the assumption that the shear stress is uniformly distributed along the embedded length of fibre with the following equation:

$$\tau = \frac{F_{max}}{\pi dl} \quad (2-2)$$

where F_{max} is the maximum load applied for debonding or pulling the fibre out of the matrix, N; d is the fibre diameter and l is the embedded fibre length, m. These two techniques can be used for almost any fibre-matrix combination and the value of force at the debonding moment can be easily obtained. However, there are some inherent limitations to these approaches, such as the presence of the meniscus formed on the fibre by the resin, which has

an inevitable effect on the measurement of the embedded length and the interfacial stress, leading to a relatively large deviation in the obtained shear strength. Also, the state of stress at the exit creates a tensile interfacial force, and no information can be obtained about the failure mode.

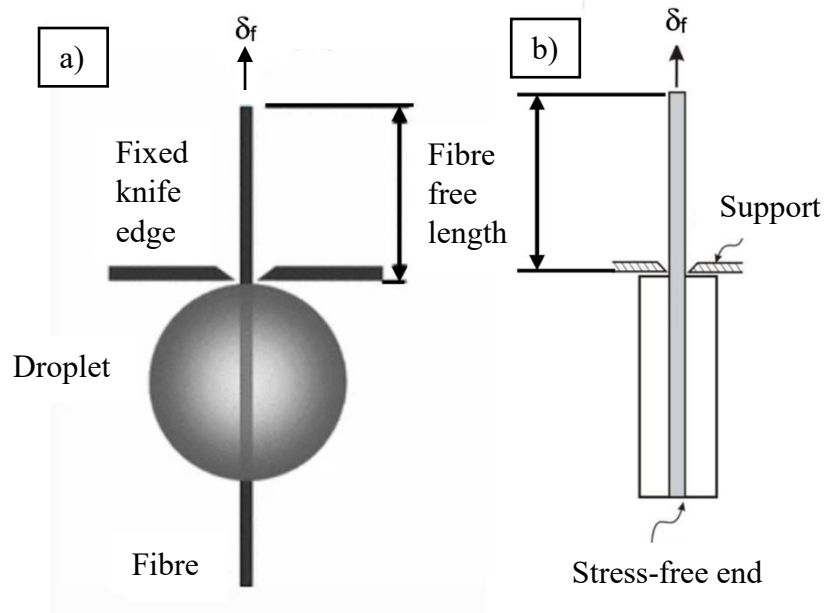


Figure 2.10 Schematic set-up of (a) micro bond test [121] and (b) pull-out test [122].

2.5.1.3 Single fibre push-out test

The single fibre push-out technique is widely used for measuring the interfacial shear strength for many fibre-matrix combinations. The single fibre perpendicular to a polished surface of a thin composite is compressively loaded using a diamond indenter to push the fibre out of the matrix. A sample holder with grooves located below the fibres is used for providing space for the pushed-out portions of the single fibres, while preventing specimen slice from bending. Compared to a pyramidal indenter tip, the conical indenter tip and the flat-end indenter tip are preferred due to the increased contact area they provide between tips and the fibre, which can effectively reduce the tip penetration into the fibre cross-section. A

typical load-displacement curve of a single fibre push-out test performed with a conical indenter tip is shown in Figure 2.11. Stage C to D in the figure represents the debonding process, as characterised by the significant increase in displacement under a constant load.

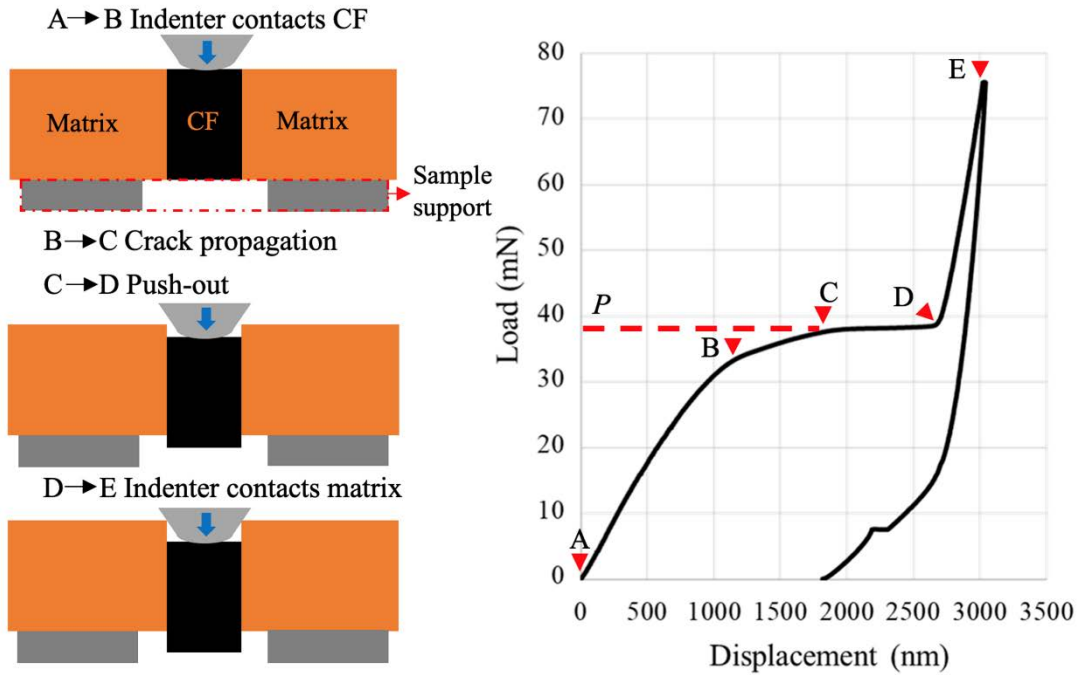


Figure 2.11 Schematic diagrams and a typical load-displacement curve of a single fibre push-out test with a conical indenter tip.

The IFSS at the fibre/matrix interface is given by:

$$\tau = \frac{F}{\pi dl} \tag{2-3}$$

where F is the load at the instance when the interfacial sliding occurs (the plateau load in between C and D in Figure 2.11), N ; d is the diameter of the fibre, and l is the fibre length (the thickness of the specimen), m.

Compared with other methods, the push-out technique is an in-situ interfacial test for real composites and it reflects actual processing conditions. The use of flat-end and conical tips

also contributes to reducing the fibre's radial Poisson expansion, which occurs during sharp indenter tip penetration.

2.5.2 Mechanical properties testing of composites

2.5.2.1 Short-beam shear test

The short beam shear test is one of the most widely used laminate techniques to measure the ILSS of composites, and has been documented as an ASTM standard [116]. In this test, a beam fabricated from unidirectional laminate composites is loaded under three-point bending. The specimen has a span-to-width ratio (l/h) chosen to produce interlaminar shear failure.

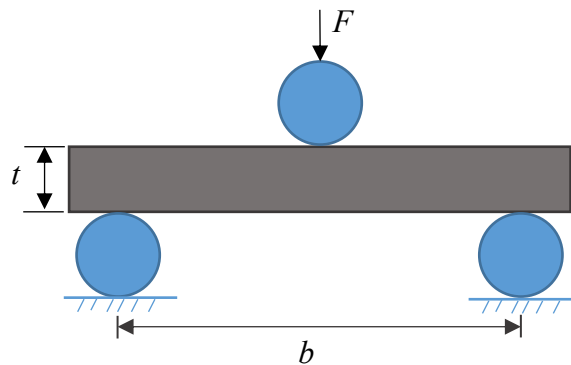


Figure 2.12 Schematic diagram of short beam shear test.

The ILSS is given by:

$$\tau = \frac{3F_{max}}{4bt} \quad (2-4)$$

where F_{max} is the maximum applied load, N; b is the specimen width and t is the specimen thickness, m. An inherent problem associated with this technique is that the loading nose of small diameter induces stress concentration and non-linear plastic deformation.

2.5.2.2 Double cantilever beam test (DCB)

The double cantilever beam test is widely used to measure the Mode I interlaminar fracture toughness (G_{IC}) in composites. As shown in Figure 2.12, a typical specimen for DCB test requires a non-adhesive insert on the midplane that acts as a delamination initiator. Opening forces are applied to the end of the specimen on the attached metallic blocks or hinges. The hinges must be configured to avoid inducing any bending moment on the specimen. The ends of the DCB are opened by controlling either the crosshead movement or the opening displacement. As the delamination grows by loading from the insert, a resistance-type fracture behaviour develops and gradually stabilises with further delamination growth. A resistance curve, illustrating the G_{IC} as a function of delamination length, is obtained to characterise the initiation and propagation of the delamination in a specimen. The interlaminar fracture toughness G_{IC} can be calculated with the following equations:

$$G_{IC} = \frac{3F\delta}{2ba} \quad (2-5)$$

where F is the applied load, N; δ is the load point displacement, m; b is the width of DCB specimen and a is the delamination length, m. In practice, this expression will overestimate G_{IC} because there may exist rotation and bending at the delamination front. Compliance calibration based on the beam theory is normally used to modify the data interpretation.

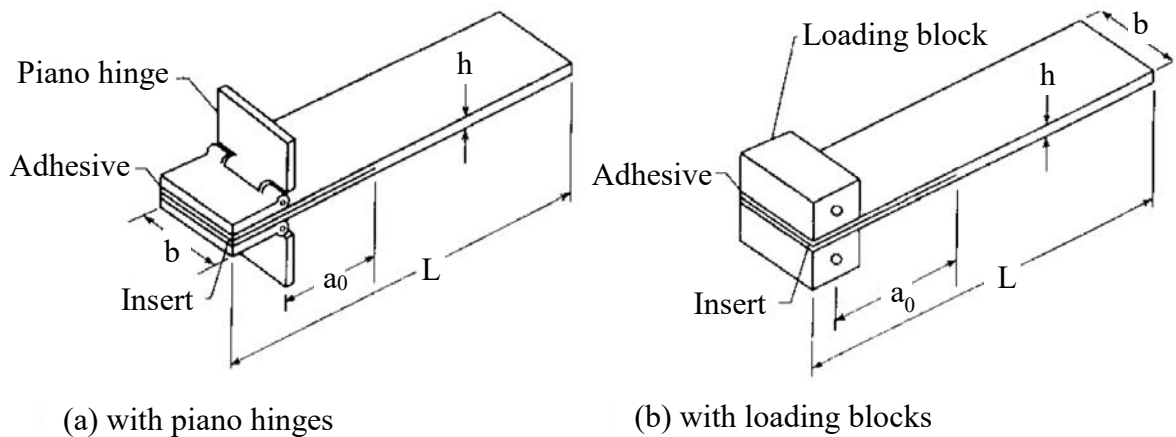


Figure 2.13 Double cantilever beam specimen [115].

Each of these methods has been used effectively in many studies to characterise interfacial adhesion. However, the reliability and validity of these results are poor, as revealed by the variance in the literature obtained values, which are frequently attributed to the poor reproducibility of the sample preparation and stress distribution [123]. Moreover, the IFSS values determined by the microscopic test are difficult to translate to macroscopic laminates, making it is difficult, if not impossible, to compare the IFSS values across different mechanical testing scales. Attempts have been made by Drzal *et al.* [124], Madhakur *et al.* [125], Herrera-franco *et al.* [89] and Filip *et al.* [123] to establish a link between the microscopic test results and the macroscopic results. Unfortunately, the only commentary of IFSS comparison between micro and macro scales was provided. Nevertheless, all testing methods reached the same conclusions, which was that these tests were valuable tools to investigate the adhesion properties, and can be used to compare the interfacial shear strength of identical composites containing fibres with different surface treatments, and to predict the behaviour of composite materials.

2.6 Surface modification on CF

Owing to the excellent properties of CFs, they have become materials of choice for the reinforcements in composites, provided that the stress applied to the matrix can fully transfer to the CFs. However, because of the chemical inertness and low free energy of CF surfaces with high density graphitic basal planes, the interfacial bonding is not strong enough to fully transfer the stress from the substrate to the CFs [3]. Therefore, further increase in the performance of CFRCs is restricted by the low CF/matrix interfacial shear strength. This challenge can be addressed through different surface treatments of CFs, which can potentially modify their surface microstructure, introduce new surface chemical groups to the CF surface, and change the surface free energy of the fibres. Although varying in details, these surface treatments generally fall into the following categories:

- a) gas-phase oxidative surface treatments;
- b) liquid-phase oxidative surface treatments;
- c) electrochemical oxidative surface treatments;
- d) thin coatings or nanostructures on the surface;
- e) plasma surface treatments with oxidative or non-oxidative gases (both atmospheric and low-pressure).

2.6.1 Surface modification effects

Extensive studies have been conducted to investigate the response of CFs to different surface modifications [99-126]. Typically, all these techniques involve physical and/or chemical modifications of the CF surfaces.

Physically alteration of the surface morphology and the structure of CFs can result in a larger surface area and an increased number of contact points, micro-voids, or surfaces. The surface

morphology of CFs varies with different surface treatments, as observed by Bijwe and Sharma [126]: compared to the unmodified surface, deeper perforations were introduced by HNO_3 modification; deeper and wider grooves were presented on the surface after oxygen plasma modification; nano-particles were revealed on YBF_3 -nano ytterbium fluoride particle modified surfaces. The surface roughness was increased from 167 nm for the unmodified surface to 245 nm, 232 nm and 234 nm following the HNO_3 , oxygen plasma and YBF_3 modifications, respectively [126]. The turbostratic structure of CFs tends to be more disordered following most of the surface treatments, revealed by the increased intensity ratio of the disordered structure, in comparison with graphitic structures [12, 127, 128].

The second modification approaches involve the formation of more chemical groups, leading to the increase of surface energy and inclusion of reactive functional groups that improve chemical bonding with the matrix in the resulting composite. Oxidation reactions initiate from the pre-existing voids on the lateral graphitic planes, as the binding energy of these planes is lower than that of the highly ordered basal planes. The preferential oxidation contributes to opening these pre-existing voids, creating more carbon elements with dangling bonds for further chemical oxidation [129]. The increased surface energy of these regions, together with the oxidised functional groups, are responsible for forming bonds and reactions with the matrix.

Most CF modification techniques can produce both effects described above. The exposure of pre-existing voids by preferential oxidation increases the surface area, which provides more mechanical interlocking sites with the matrix, as well as available surface sites for the attachment of functional groups.

Preservation of fibre mechanical strength after surface modification is essential for the resulting composites as the on-axial properties of the composites, such as longitudinal tensile, compressive, and flexural properties, are dominated by the fibre mechanical properties [124]. However, it is also widely recognised that these surface treatments, especially ones which involve the severe etching of the fibre surface, can increase the adhesion capacity of CFs with the matrix but at the cost of fibre strength, mainly due to the introduction of excessive surface defects, which act as stress concentrators. Bijwe and Sharma [126] investigated the relationship between the tensile strength and the structural disorder ratio of CFs modified by acid, plasma, gamma-ray and nanoparticles. They reported that the reduction in the tensile property of CFs by surface modification is accompanied by an increase in the structural disorder ratio (I_D/I_G) and a decrease in the surface crystallite size (L_a).

According to the analysis of the approaches for various surface modifications of CFs, Hughes [97] and Dilsiz [95] summarised the potential mechanisms of surface modification in improving the CF/matrix adhesion through the following routes:

- by removing the weakly bonded regions on the fibre surface to provide a more intimate contact between the fibre and the matrix, thus leading to the increase of the Van der Waals force,
- by promoting mechanical interlocking between the fibre and the matrix through roughening the surface,
- by supporting the matrix molecules physically to entangle with or diffuse into the polymer coating on the fibres through the molecular network,
- by increasing the wettability of the fibre surface,
- by introducing new functional groups on the fibre surface for subsequent chemical bonding,

- by using a thin layer of ‘coupling agent’ that will chemically bond to both the fibre and the matrix.

2.6.2 Gas-phase oxidative surface treatments

Air, oxygen, fluorine, oxygen-containing gases (e.g. ozone, steam and carbon dioxide) can be used for gas-phase oxidative treatments [130]. The uneven burning away of CF surface layers during gas-phase oxidative surface treatments can produce more active sites but cause inevitable weaknesses in the fibre structure and reduction in fibre strength. As a result, these gas-phase oxidative treatments introduce the surface chemical reactions at a price of the fibre strength if the treatment is extended. Thus far, oxidative treatments of CFs in air have not been effective in enhancing the interfacial shear properties of the resulting composites. For example, Herrick *et al.* [130] and Kucera *et al.* [131] reported that the oxidation in air or oxygen at elevated temperatures may lead to notable pitting of CF surfaces, which reduced the fibre strength. High temperature (> 400 °C) is needed for efficient oxygen oxidative treatment of CFs, but the risk of spontaneous ignition at such temperatures is very high. Molleyre and Bastick [132] treated PAN-derived CFs in oxygen at 550 °C and the external and internal structures of the untreated and treated CFs were examined by adsorption and scanning electron microscopy (SEM). They proposed that the increase in IFSS was due to the increase in surface area of the fibres. Molleyre *et al.* [132] also oxidised CFs using CO₂ at temperatures between 850 and 925 °C, and observed that morphology changes on the fibre surface were similar to the treatments with oxygen diluted with nitrogen. Seo and Park [133] investigated the effect of oxy-fluorination on CF surfaces. X-ray photoelectron spectroscopy (XPS) confirmed the hydrophilic surface of modified fibres were due to the introduced functional groups: C-O, C=O, HO-C=O and C-F, which contributed to the chemical reaction with the matrix.

2.6.3 Liquid-phase oxidative surface treatments

Comparing with gas-phase oxidative treatments, liquid-phase oxidative treatments are milder and more effective in improving the interfacial shear properties of CFRCs by mainly altering the chemical composition of the CF surfaces through a direct chemical reaction in a given solution. The chemical solutions adopted in these oxidative treatments are usually acid solutions, organic solutions or other specific types of solutions, such as nitric acid (HNO₃), sodium hypochlorite (NaClO), acidic potassium permanganate (KMnO₄), sodium hydroxide (NaOH) and maleic anhydride [134]. The liquid-phase oxidative treatments can corrode the surface of the CFs and/or create perforations to improve the mechanical interlocking between the fibre and the matrix, simultaneously. However, pits, crevasses, micro-voids and flaws are induced on the surface of CFs during these treatments, which will reduce the single fibre strength. The influence of HNO₃, NaOH and maleic anhydride on CFs was investigated with surface enhanced Raman scattering (SERS), X-ray photoelectron spectroscopy (XPS), Fourier transform infrared spectroscopy (FTIR) and mechanical property testing. The Raman characterisation showed that the vibration modes of -C=C-, -CH₂- and C-O were found on the maleic anhydride treated CFs. Acidic functional groups were introduced on the HNO₃ treated CF surface and the acidic capacities of CFs increased with oxidation time [135]. The acid-oxidised fibre surfaces treated with re-fluxion in aqueous NaOH after the HNO₃ oxidation removed weakly bound, partially oxidised, graphitic fragments and generated some new immobilised acidic functional groups, while simultaneously losing acidic functional groups on the CF surface [136]. The weight and graphite layer losses were 0.23 % and 29 Å in thickness respectively with the re-fluxing NaOH solution for 1 hour [136]. The introduction of functional groups (-COOH and -COOR), β-carbon and bridged structure contributed to the compatibility of modified fibre surface with the

bismaleimide (BMI) matrix. It should be pointed out that liquid-phase modification has been criticised by researchers for the environmental pollutions, as well as the time-consuming processes for removing the acid adsorbed on the fibre surface [135].

2.6.4 Electrochemical oxidative surface treatments

Electrochemical oxidative modification is becoming an attractive route for surface treatment of CFs, as it offers more control over surface chemistry and allows continuous processing. The electron transfer in the electrolyte solution alters the oxidation state, and hence leads to the modification of the CF surface. A variety of electrolytes, such as sodium hydroxide, ammonium hydrogen carbonate, sulphuric acid and nitric acid, are employed to create desired functional groups and alter the surface morphology of CFs [137]. The adsorbed electrolyte on the fibre surface increases the surface activity by extending surface areas via the formation of ultra-micro pores and by introducing polar oxygen-containing functional groups over the extended porous surface. Therefore, the electrochemically treated CFs possess enhanced adhesion with most matrices. However, some discrepancies can be found in the literature, with Donnet and Ehrburger [138], pioneers in this field, finding that oxidation in the alkaline medium did not change the oxygen content of CFs, whereas anodic oxidation in nitric acid solution considerably increased the amount of oxygen functional groups. On the other hand, Yumitori and Nakanishi [139] observed that the oxygen concentration on the fibre surface increased rapidly as the electrical charges were increased in both alkaline (NaOH) and acidic (H₂SO₄) solutions. Bader and Baillie [140] studied the effect of electrochemical oxidative treatment on fibre/epoxy-resin matrix adhesion. High-strength PAN-derived CFs were electrolytically oxidised with the current density varying from 1 to 100 A.m⁻². The results of embedded-fibre fragmentation tests demonstrated that

the interfacial strength of the composites had been effectively increased, which was attributed to the increase of the number of acidic groups in the interfacial region.

2.6.5 Thin coatings or nanostructures

The application of thin coatings or nanostructures, such as silicon carbide (SiC), silicon dioxide (SiO₂), titanium dioxide (TiO₂), graphene oxides, carbon and carbon nano tubes (CNT) onto the CF surface, has been proven to be an effective technique for the modification of fibre surfaces through increase of the surface area and roughness, and enhancement of the surface wettability [141]. Many organic polymeric materials such as polyvinyl benzene, polyimide and organ silanes are grafted on to CF surface as well, in order to improve the interfacial bonding of CFs with the resin matrix through covalent or ionic bonding [142]. CNTs are in the lead in this regard, owing to their intrinsic properties, such as remarkable electrical and thermal conductivity, exceptional tensile strength and good optical properties. Hence, the CNTs coated CFs can be applied to electrodes for super-capacitors, fuel cell electrodes and conductive layers. The key challenge in the CNTs coating is how to homogeneously distribute the CNTs onto the CF surface. Typical techniques used for CNTs attachment on CF surface involve chemical vapour deposition (CVD) [143-145], injection chemical vapour deposition (ICVD) [146-148], chemical vapour infiltration (CVI) [149], electrophoretic deposition (EPD) [150, 151] and chemical/electrochemical grafting [152-154]. The efficiency of CNT coatings depends on the distribution, orientation and length of the coated CNTs. Lv *et al.* [146] reported that CNTs with a perpendicular alignment and long length showed a remarkable improvement of IFFS in epoxy composites due to the improved wettability and the increased contact interfacial area. The improved wettability was attributed to the increase in specific surface roughness and the capillary action of the grafted CNTs. An increase of two orders of magnitude was found in the specific surface area

of CNT coated CFs. However, reduction in the single fibre strength following CNT coating of CFs has been reported by many researchers, which is attributed to the adsorption of iron particles on the fibre surface and the increased surface flaws [147, 155, 156]. For example, Sager *et al.* [155] found that the ultimate tensile strength of the single fibre significantly decreased by 37% in the case of the radially aligned CNTs, and by 30% in the case of randomly oriented CNTs, introduced using CVD processing. Similarly, a slight decrease was also observed in the tensile modulus of the fibre, with a 9% reduction and a 13% reduction for the radially aligned and randomly oriented CNTs coated fibres, respectively.

2.6.6 Plasma surface treatments

Plasma treatment has become a promising method to improve the adhesion between the CF surface and matrix materials, since it offers an economic and environmentally-friendly approach to modify the fibre surface chemistry with limited influence on the bulk properties. As the fourth state of matter, plasma is an ionised gas medium containing a variety of highly excited species, such as electrons, ions, free radicals, molecules and other metastable excited species. It can be obtained when gases are activated to higher energetic states and ionised. Typical gases used to create a plasma include air, hydrogen, oxygen, nitrogen, ammonia, methane, helium and argon. When the CFs are subjected to plasma, the electrons, ions and radicals collide with the exposed CF surface, thus rupturing covalent bonds and creating new free radicals. The activated CF surface can then readily react with the excited gas species and create chemically reactive groups, such as hydroxyls, ethers, carbonyls, aromatics and ammoniacals. These reactive functional groups can improve the CF surface reactivity and polarity, and hence enhance the adhesion potential with the matrix in the resulting composites. In addition, the etching effect caused by the ion bombardment from the direct plasma treatment has the potential to remove surface contaminations from the CFs, therefore

allowing better contact and alter the fibre surface morphology, and hence enhance the mechanical interlocking between the fibre and the matrix.

The techniques used to produce plasma include radio frequency (RF), microwave (MW), corona discharge (CD), direct current (DC), dielectric barrier discharge (DBD) and plasma immersion ion implantation (PI³) [129]. CD and DBD treatments are typical methods conducted under atmospheric pressure, and therefore, they are convenient and easy to produce continuously. On the other hand, RF, MW and DC plasmas are typically carried out in a vacuum, and thus they have been named as low-pressure plasmas (LPP). As a result, the collision frequency between the energetic species and the gas molecules of the LPP plasma is much lower than that of atmospheric plasma, resulting in less destructive damage of the fibre surfaces.

2.6.6.1 Low-pressure plasma treatments

Due to its capacity in improving the interfacial adhesion with less reduction of the fibre strength, low-pressure plasma is an attractive option for surface modification. Among the LPP techniques, conventional DC plasma and corona discharge require the use of electrically conductive electrodes and hence they can only be used to modify the surface of conductive materials. RF and MW plasmas can be applied to non-conductive material, but the equipment is very exquisite and expensive.

The proposed mechanisms involved in the plasma surface modifications of CFs are through removing containments and roughening the surface through mild ion bombardment from the surface of CFs, as well as introducing functional groups and altering the surface polarity. For example, the micro-bond fibre pull-out test conducted by Wu et al [13] revealed a 29% improvement of IFSS for a 5 min oxygen DC plasma treatment, which was attributed to the

increase of the surface oxygenated functional groups and the increase of surface energy (41% enhancement). Lee *et al* [157] found that the surface roughness and density of functional groups were increased for both oxygen and hydrogen plasma treatments, which contributed to the adhesion with the polyetherimide matrix. However, such plasma treatments can still damage the fibre surface due to bombardment, even with their less destructive nature when compared to other methods [11, 158]. For example, Jang [14] reported that oxygen RF plasma treatment improved the fibre/matrix interfacial adhesion but at a cost of reduced average tensile strength from 3.80 to 3.01 GPa; ammonia gas plasma had a less damaging effect, but still reduced the filament tensile strength from 3.80 to 3.65 GPa. The explanation given for the tensile strength degradation is the inevitable surface damage during the direct plasma treatments, in which samples were directly immersed in the plasma. With this regard, Inagaki *et al.* [159] proposed remote plasma treatment, in which samples to be treated are placed away from the plasma formation zone. They proposed that the surface degradation was initiated by the bombardment of the ions and the electrons, while the desirable surface functionalisation came from the interaction with radicals in the plasma. Therefore, the remote plasma treatment could eliminate ions bombardment induced degradation while still providing the radicals necessary for surface modification, since radicals have longer lifetime than ions and electrons. However, it should be noted that it is difficult to scale up their laboratory experimental set-up to a large production reactor.

2.6.6.2 Active screen plasma (ASP) treatment

2.6.6.2.1 Fundamentals of active screen plasma technology

Recently, a more advanced plasma technology, active screen plasma (ASP), has been developed based on the glow discharge in DC plasma and the principle of remote plasma to avoid the undesirable effects associated with traditional direct plasma treatment [160]. In

this technique, the worktable and samples are surrounded by a metal screen. The high potential is applied between the metal screen and the equipment wall. The worktable and the samples to be treated are instead placed at a floating potential. Thus, the plasma is generated on the metal screen and works on the samples assisted with a specially designed fan on the top of the plasma equipment.

2.6.6.2.2 Advantages of active screen plasma technology

The advanced ASP has gradually become a practical industrial technology due to its several distinct advantages. The most significant advantage of ASP surface treatment, compared with the conventional plasma treatment processes, is that surface damaging phenomena, such as arcing, edge effects and hollow-cathode damage, are completely avoided. This occurs due to the cathode potential being applied to the active screen, rather than to the samples to be treated, and hence there is no direct ion bombardment to the sample surface during ASP treatment. Secondly, ASP technology can be applied to both conductive and non-conductive materials, such as metals, ceramics, polymers and composites. This is because the samples to be treated by ASP treatment are placed in a floating potential so that the electrical conductivity of the samples is not necessary. Additionally, the samples are typically directly heated by the plasma in a conventional plasma furnace, leading to a temperature difference between the outside and the centre. This problem can be partially solved using the ASP technique, as the samples are heated by the thermal radiation from the plasma generated on the screen. The temperature can be controlled very closely by adjusting the current provided to the screen, and precisely measured by the thermal couples. Furthermore, ASP technology is economic and environmentally friendly. ASP treatments usually operate with low voltage (under 500 V) and low vacuum (under 100 Pa), which will contribute to reducing the cost of operation and equipment. No harmful by-products, toxic or hazardous liquids or gases are

produced during the treatment process, meaning that ASP treatment is non-destructive to the environment. Finally, ASP technology is regarded as reliable, reproducible, and applicable to different sample geometries, and has the ability to alter the surface characteristics, including surface tribology, morphology, chemical, electrical, biological and mechanical properties.

2.6.6.2.3 ASP surface modification of CF

a) Plasma interaction with CF

The technical feasibility of ASP for surface modification of fibres relies on its energetic species and relatively low gas temperature. The former provides the possibility of chemical reactions and ion bombardment on the fibre surface upon contact. The latter, being a cold plasma, is beneficial for allowing the fibres to be modified without loss of their mechanical properties. The temperature difference between the energetic species and the gas molecules is mainly determined by the mean free path of the particles between collisions, which primarily depends on the gas pressure. These energetic plasma species (ions and radicals) can travel longer distance between collisions, and the CFs interacting with such plasma are mainly subjected to radicals and a low-energy ion bombardment. Free radicals readily promote chemical modification on the surface of CFs due to their longer lifetime than the other energetic species. The mild ion bombardment has a positive effect for initiating chemical modification by generating new defects and active sites, and for increasing the surface area through roughening of the fibre surface. Also, the binding strength of the most common chemical bonds on CFs is lower than the energy of these energetic species found in the plasma. Therefore, the interaction of these energetic species with the CF surface can trigger chemical reactions and alter structures, while the average temperature of the gas remains low.

b) General mechanisms of plasma modification on the adhesion of CF to the matrix

The plasma contains highly activated species, such as electrons, ions and radicals, which interact with CFs to modify the surface. Generally, three potential mechanisms are involved in the ASP modification that contribute to the improved adhesion of the two components:

- removal of surface contaminants and weak bonds by mild ion bombardment;
- enhancement of wettability through the incorporation of polar groups that facilitate the spontaneous spreading of adhesive or matrix resins;
- formation of the functional groups on the surface.

2.6.6.2.4 Research status of ASP treatment of CF

A feasibility study has been conducted by Santiago *et al.* to explore the potential of ASP for the surface treatment of CFs. The optical emission spectroscopy (OES) results for different ASP conditions confirmed that the ASP modified surface of CFs was enriched with nitrogen functional groups. XPS results and contact angle measurements have revealed functionalised hydrophilic surfaces, which can potentially contribute to further adhesion with the matrix. However, the modified surface was found to have a hydrophobic recovery when exposed to air with a loss of 78% of the polar regions after only 3.4 days. In addition, it is still not clear if and how the ASP treatment will affect the strength of CFs and improve the interaction with the matrix (i.e. IFSS).

2.7 Summary

In this chapter, the development of carbon fibre (CF) and related research was briefly reviewed (Section 2.1), followed by an overview of the production processes for both PAN-derived CF and pitch-derived CF, with an introduction to their structures and main properties (Section 2.2). Owing to the excellent properties of CFs, they have been used as reinforcing materials in composites (Section 2.3). However, the application of CF reinforced composites (CFRCs) is limited by poor interfacial bonding. The composition of the interface and the mechanisms of the interfacial bonding are illustrated (Section 2.4), followed by the estimation methods of interfacial shear strength (IFSS).

Being the main scope of this project, the surface modifications of CF are reviewed in detail (Section 2.6). Although numerous surface modification methods have been developed to improve interfacial adhesion of CFs to the matrix in composites, most of these treatments either lead to environmental concerns due to the use of toxic chemicals or reduce the mechanical properties of CFs due to surface damage. Active screen plasma (ASP) offers an economic and environmentally-friendly way to modify fibre surface chemistry while avoiding the undesirable effects associated with traditional direct plasma treatments. However, few reports were found on the physical and chemical interaction between the active screen plasma and CFs and the direct evaluation of the interfacial bonding between ASP modified CFs and the matrix in resulting real composites.

Therefore, this PhD project was aimed at exploring the potential of ASP technology for the surface modification of CFs to improve their adhesion to epoxy matrix and the mechanical property of the resulting CF-reinforced composites. To this end, advanced ASP technology was utilised to modify the surface of PAN-derived CFs using different gas mixtures. The

modified CF surfaces were fully characterised by scanning electron microscopy (SEM), atomic force microscopy (AFM), X-ray diffraction (XRD), Raman spectroscopy, X-ray photoelectron spectroscopy (XPS), contact angle and dynamic vapour sorption (DVS) to understand the response of CFs to the ASP. Tensile tests on single fibre and fibre bundle were carried out to directly study the effect of ASP treatment on fibre tensile strength. Nano-indentation enabled single fibre push-out testing method was used to investigate the interfacial behaviours between the single fibre and the epoxy substrate. The mechanical properties of CF-reinforced composites were examined by tensile strength, flexural strength, interlaminar shear strength (ILSS) and interlaminar fracture toughness.

CHAPTER 3 EXPERIMENTAL

3.1 Materials

The carbon fibre (CF) used in this work was HTA40 E13 6K 400 tex provided by Toho Tenax[®]-E. It is poly-acrylonitrile (PAN) derived CF and commercially available as epoxy sized. 5H satin weave carbon fibre fabric G0926 based on HTA40, with a typical density of around 370 g/m² and a thickness of 0.38 mm, was obtained from HEXCEL Industries Inc (USA). It was used as reinforcement for manufacturing composites in this work. A three-part epoxy-based resin system (Araldite[®] LY 556, Aradur[®] 917 and Accelerator[®] DY 070) were purchased from HUNTSMAN industries (USA) and used as the matrix material for the sample preparation of the push-out tests. The documented physical and mechanical properties of HTA40 CFs and epoxy resin system are summarised in Table 3.1 and Table 3.2, respectively.

Table 3.1 Documented properties of HTA40 carbon fibres.

Diameter (µm)	Strength (GPa)	Modulus (GPa)	Strain (%)	Density (g/cm ³)	Sizing type	Sizing volume
7	3.95	238	1.7	1.76	Epoxy	1.3%

Table 3.2 Documented properties of three-part resin system at 25 °C.

	Epoxy Content (eq/kg)	Viscosity (mPa s)	Density (g/cm ³)	Flashpoint (°C)
Araldite	5.3-5.45	10000-12000	1.15-1.20	> 200
Aradur 917	-	50-100	1.20-1.25	195
Accelerator DY 070	-	≤ 50	0.95-1.05	92

3.2 Active screen plasma treatment

Active screen plasma (ASP) treatments were carried out at a pressure of 75 Pa in an AS Plasma Metal 75kVA + 15KV industrial scale plasma furnace, which is equipped with an austenitic stainless-steel mesh cylinder as the active screen. The temperature within the furnace was measured by placing a thermocouple next to the samples. The voltage, which was controlled between 300 to 400 V, was applied between the active screen (cathode) and the walls of the furnace (anode) during all treatments. The CFs were hung on a stainless-steel rack with a distance of 30 mm to the active screen (Figure 3.1). The treatment current was recorded to be between 60 and 70 A, and the temperature in the furnace increased from the room temperature ($\sim 25\text{ }^{\circ}\text{C}$) to approximately $32\text{ }^{\circ}\text{C}$ for all treatments.

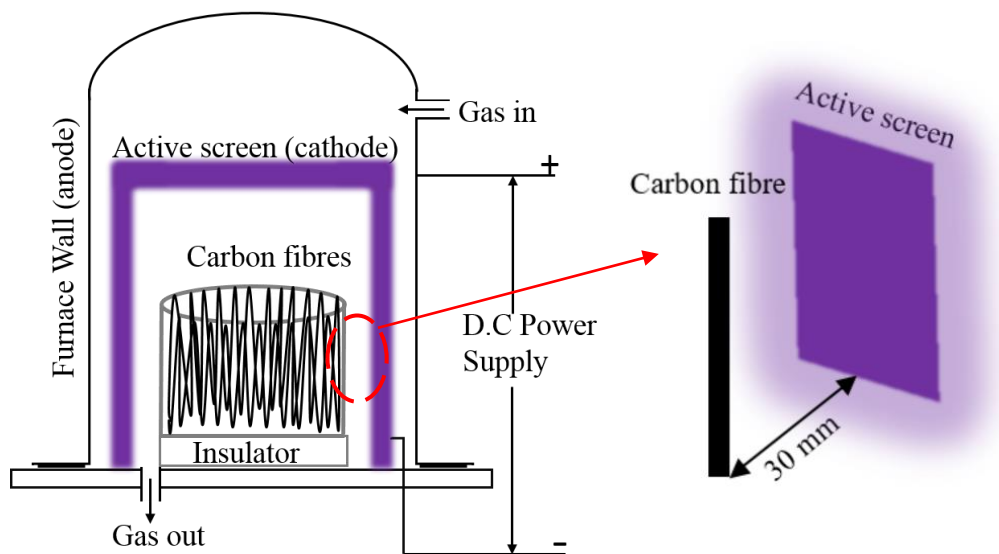


Figure 3.1 Schematic diagram of active screen plasma treatments.

As shown in Table 3.3, two groups of ASP treatments were designed to study the effect of gas mixtures and treatment durations. The first group of ASP treatments were conducted for 2, 5 and 8 minutes in a gas mixture of 25% N_2 and 75% H_2 (ASPN). The second group of ASP treatments were carried out for 5 minutes with 5 to 15% Ar in the gas mixtures (ASPAr).

The ratio of gases was chosen based on previous work in this Group. De-sized CFs were set for investigating the effect of commercial epoxy resin. They were obtained by immersing the pristine CFs in acetone at 45 °C for 24 hours and then dried in a desiccator.

Table 3.3 Active screen plasma treatment conditions and the corresponding sample codes.

Sample code	Gas mixture	Duration (minute)	Pressure (Pa)	Power (W)
Pristine				
De-sized	none	none		
ASPN2	25%N ₂ + 75%H ₂	2		
ASPN5	25%N ₂ + 75%H ₂	5		
ASPN8	25%N ₂ + 75%H ₂	8		
ASPAr5-5%	23.75%N ₂ + 71.25%H ₂ + 5%Ar		~75	25000
ASPAr5-10%	22.50%N ₂ + 67.50%H ₂ + 10%Ar	5		
ASPAr5-15%	21.25%N ₂ + 63.75%H ₂ + 15%Ar			

3.3 General characterisation

3.3.1 Scanning electron microscopy (SEM)

A JEOL 7000 field emission scanning electron microscopy (FESEM) was utilised to observe the surface morphology, pushed-out fibres and fractography throughout this study. In most cases, the accelerating voltage and working distance were fixed at 20 kV and 10 mm respectively, but the surface morphologies of CFs were observed at 5 kV and 5-6 mm working distance due to the relatively low electrical conductivity of the CFs. Specimens for push-out tests were coated by a nanogold sputter for 1 minute (coating rate 10 -12 nm every 3 min) to improve the electron conductivity prior to the SEM observation.

3.3.2 Atomic force microscope (AFM)

A Bruker Innova AFM was used in tapping mode with Bruker MSNL-10 probes to obtain the detailed topographies of the CF surfaces and evaluate the surface roughness. All the images were collected in a $5\ \mu\text{m} \times 5\ \mu\text{m}$ area.

3.3.3 Raman spectra

Raman spectra of pristine and ASP treated CFs were collected by using a Renishaw inVia Raman microscope fitted with a diode laser source giving monochromatic red light of 488 nm wavelength. A super long 100X objective was used to focus the laser beam on the specimen and to collect the scattered radiation. The beam power was set at 10% out of the 35 W to minimise damage to the samples. The exposure time was 10 seconds per scan and 10 accumulations were taken for every sample. At least three different positions were examined for pristine and for all ASP treated CFs. The raw experimental data of the Raman

spectra were analysed using the WiRE software (version 4.2) by Renishaw and peak-fitted by Gaussian curves in order to determine the peak intensities and Raman shifts [12].

3.3.4 X-ray diffraction (XRD)

The crystallisation status of CFs before and after ASP treatments were analysed by X-ray diffraction using a Bruker D8 Advance X-ray diffractometer working with Cu-K α radiation ($\lambda = 0.154$ nm). The CF samples were ground to powder by cryo-miller (SPEX CertiPrep 6750, HORIBA Jobin Yvon) and then scanned between 2θ angles of 10° to 90° at a speed of 10 seconds per step (0.01418°). The obtained XRD patterns were analysed with X'Pert Highscore Plus software and fitted with Gaussian functions to calculate the fibre structure parameters L_c (crystallite height) and L_a (crystallite width) using Scherrer's formula:

$$L = K\lambda/(\beta \cos \theta) \quad (3-1)$$

where K is a dimensionless shape factor ($K_c = 0.89$, $K_a = 1.84$); λ is the X-ray wavelength, nm; β is the full peak width at the half maximum (FWHM); and θ is the Bragg angle of the corresponding peak.

3.3.5 X-ray photoelectron spectroscopy (XPS)

The surface bonding and chemical composition of pristine and ASP treated CFs were examined by XPS (PHI 5000 VersaProbe III) in a Thermo Scientific Sigma instrument using a monochromatic Al X-ray source (1486.6 eV, 15 kV and 1mA anode current). Full-range survey spectra, as well as detailed C 1s, O 1s and N 1s spectra, were collected in order to understand the functionalisation following ASP treatments. The resulting spectra were analysed using Matlab $\text{\textcircled{R}}$ software and the peak-envelops of the detailed spectra were fitted with a set of Gaussian functions [97].

3.3.6 Contact angle

Contact angle measurements were performed with resin microdroplets on the CFs before and after each surface modification to study the effect of ASP treatment on the wettability of the CFs. The quantitative assessment of the wettability of single CF filaments proved to be very challenging. Therefore, the surface wettability of pristine and modified CFs was assessed by measuring the contact angle of microdroplets of epoxy resin LY 556 on CFs using optical microscopy (Zeiss Axioskop 2). Single fibres were separated from the bundle and attached to the edge of a petri dish. The petri dish was then tilted to 45 ° and the epoxy resin LY 556 was dropped using a 1 ml syringe and allowed to move down the fibre through gravitational forces. As a result, the single fibre was wetted with many epoxy microdroplets (Figure 3.2). The microdroplets were observed and the contact angles were measured using a Zeiss Axioskop 2 microscopes. At least 10 microdroplets were examined for each sample. All the measurements were conducted at room temperature.

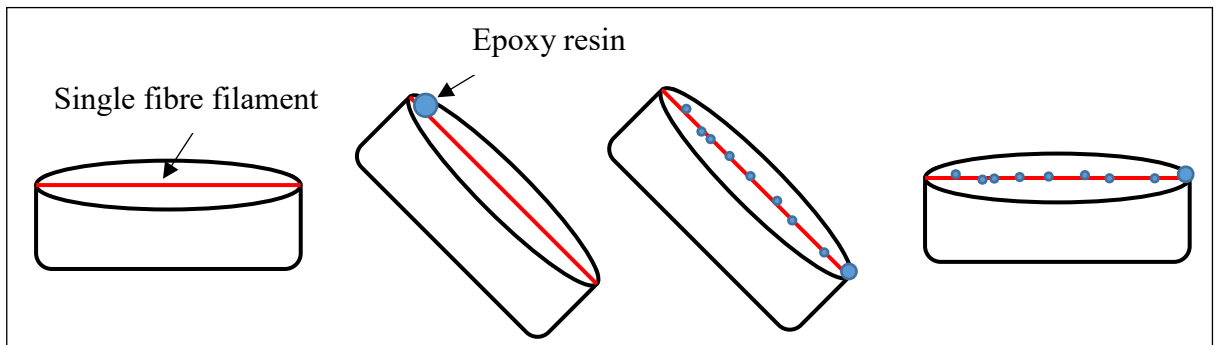


Figure 3.2 Schematic diagram of the petri dish holder used for contact angle measurements.

3.3.7 Dynamic vapour sorption (DVS)

A dynamic vapour sorption (DVS) gravimetric analyser (DVS advantage) was used to measure the adsorption characteristics of pristine and ASP treated CFs. The absorbent mass was measured directly by a recording microbalance with a sensitivity of 0.1 µg housed in a

controlled temperature chamber. The pristine and ASP treated CFs were cut into appropriate 5 mm lengths and then fed into the sample pan with mass in the range of 10.0 to 10.5 mg. All samples were first dried for 2 hours at 120 °C, before going through the adsorption process carried out at room temperature (25 °C) for 10 hours with a relative humidity of 60%. Desorption conducted at room temperature (25 °C) for 10 hours with a relative humidity of 0% was performed following the adsorption process, as illustrated in Figure 3.3. The same procedure was carried out over a period of 2 months after the plasma treatments, to investigate the aging of the functionalised surfaces in air.

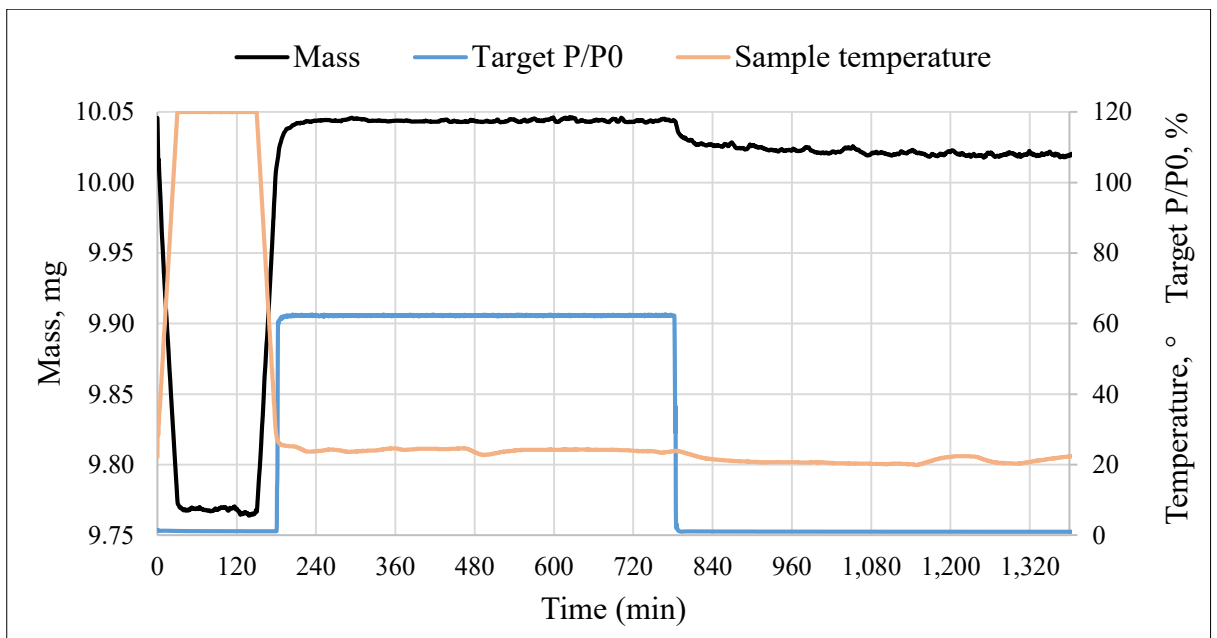


Figure 3.3 An example of DVS test procedure.

3.3.8 Tensile test of single fibre

Single fibre tensile strength tests were performed using a universal testing machine INSTRON with a load cell of 10 N and crosshead speed of 0.2 mm/min. Individual fibres were separated from fibre bundles carefully and glued each end to a paper frame, with a gauge of 25.0 ± 0.5 mm, as illustrated in Figure 3.4. The paper frame was gripped to the

testing machine and was then cut into two parts before testing. The testing procedure is in accordance with ASTM D 3379-75 and at least thirty specimens were tested for each type of CFs. The fibre tensile strengths δ were fitted to a Weibull distribution function of the form of

$$P_f = 1 - \exp(-(\delta/\delta_0)^m) \quad (3-2)$$

where P_f is the failure probability to yield the values of the fibre reference tensile strength δ_0 , and m is the Weibull modulus.

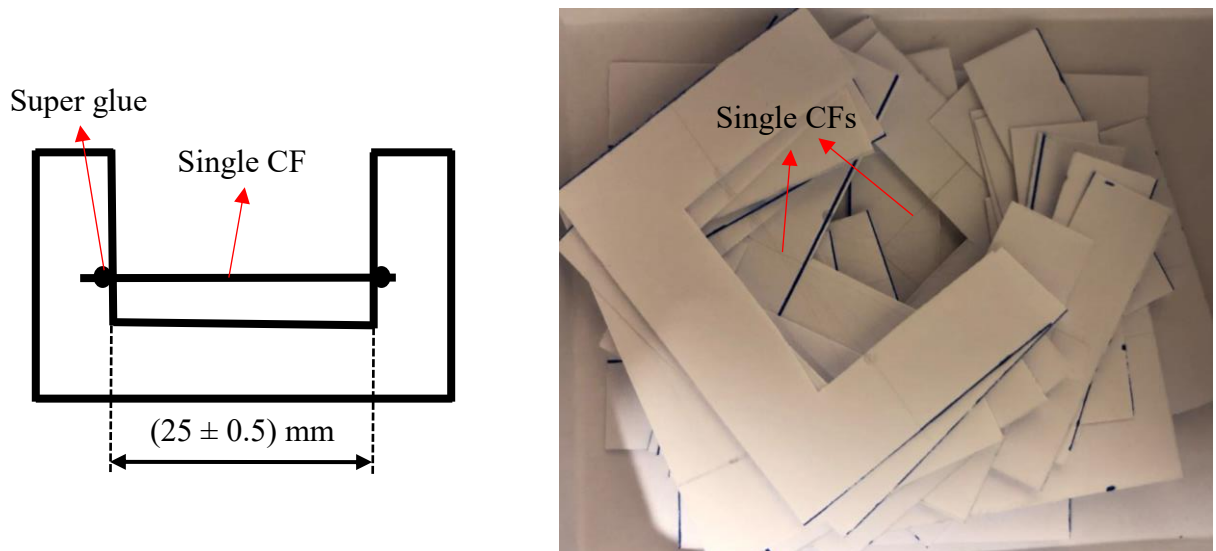


Figure 3.4 Paper frames with attached single fibre for tensile tests.

3.3.9 Tensile test of fibre bundle

Tensile tests of CF bundles were conducted using a universal testing machine INSTRON with a load cell of 10 N. To prepare specimens for fibre bundle tensile test, pristine CF bundles and modified bundles were cut into 300 mm long sections and set in a self-prepared frame. Both ends of the bundles were sandwiched between two aluminium pieces with the epoxy adhesive 9323 B/A (3M Scotch-Weld), and then cured at least for 12 h. The working length of fibre bundles for tensile tests was designed to be 150 mm. Then 70 g weights were

added to one end of bundles to keep the fibres straight. The image of the self-made frame with the fibre bundles attached for tensile tests is shown in Figure 3.5. The specimens were then clamped in the testing machine and tensile tests were carried out at a ramp rate of 2 mm/min. At least 7 specimens were tested for each sample type.

The average tensile stress of fibre bundles is given by the following equation,

$$\delta = \frac{F_{max}}{6000\pi r^2} \quad (3-3)$$

where F_{max} is the maximum load for each test, N; r is the radius of the fibre, m; and $6000\pi r^2$ refers to the cross-sectional area of fibre bundle (6000 fibre filaments).



Figure 3.5 Frame and attached fibre bundles for tensile tests.

3.4 Evaluation of CF/epoxy interfacial adhesion

3.4.1 Preparation of composite slice and sample support

Pristine and ASP treated CFs were impregnated into the epoxy resin system (Araldite® LY 556, Aradur® 917 hardener and DY 070 accelerator in a ratio of 100:90:1). After being degassed in a vacuum desiccator, the CFs/epoxy resin systems were heated at 80 °C for 4 hours (gelation process) and then heated at 140 °C for 8 hours (post-cure) to form the composites bar, as shown in Figure 3.6 (a).

Thin composite slices, as shown in Figure 3.6 (b), were cut from the produced composite bars with a thickness of approximately 1 mm. Then the thin slices were glued onto a GATAN disc grinder for grinding and polishing with a sequence of silicon carbide papers of 1200, 2500, and 4000 grit size, before oxide polishing using a colloidal silica suspension (Struers OP-S) until the thickness of the composite slices was reduced to ~35 µm. The surface of the slices was observed using an optical microscope to confirm the damage-free state following the grinding and polishing procedures. As shown in Figure 3.6 (c), the fibres of the polished composites slice were observed to be surrounded by the matrix without interface debonding.

The thinned composite slices were then glued onto the top of a purposely designed metallic sample support, as shown in Figure 3.7 (a). Parallel narrow grooves with a width of 20 µm (Figure 3.7 (b)) were cut into the surface of the metal support using a femtosecond pulsed laser beam. These narrow grooves facilitated the push-out of single fibres from the composite slice, while preventing excessive deformation of the thin specimen slice from bending.

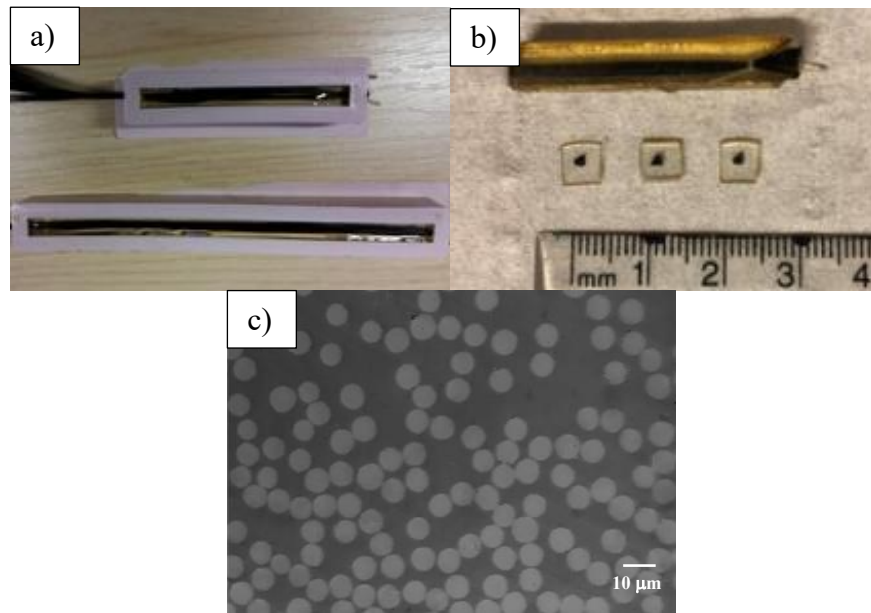


Figure 3.6 Images of (a) produced composite bars, (b) composite slices and (c) surface of polished thin composites slice.

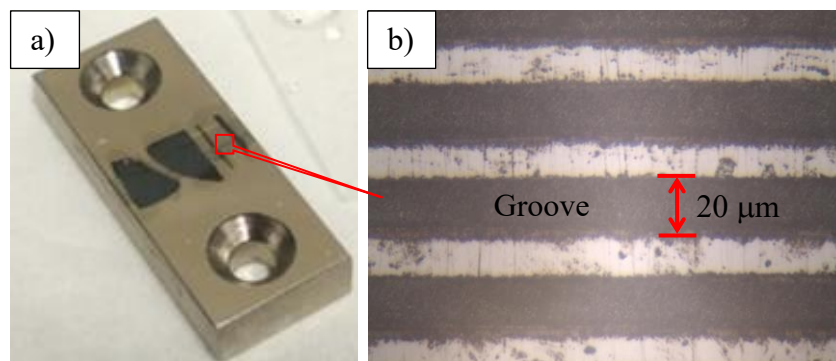


Figure 3.7 Images of (a) thin composite slices mounted on the metal sample support and (b) magnified grooves made on the sample support.

3.4.2 Interfacial shear strength (IFSS) test

3.4.2.1 Test set-up

The push-out tests were performed using a NanoTest Vantage system (Micro Materials Ltd, Figure 3.8) to determine the IFSS between the CF and the matrix. A customised diamond indenter was used for the push-out tests, and the geometric schematics for this indenter is

schematically are illustrated in Figure 3.9. A conical indenter tip with a diameter of 9.3 μm was used for the push-out tests, thus, allowing single fibres, with a diameter of 7 μm , to be pushed out of the matrix by 1.6 μm before any contact was made with the adjacent matrix. The purpose of the conical indenter tip shape was to increase the contact area between the indenter tip and the fibre cross-section. Therefore, this limited penetration of the tip into the cross-section of the fibre, when compared with the more frequently used Berkovich indenter tip, which could exert forces onto the interface and hence lead to an overestimation of interface bonding. The loading and unloading were carried out at a constant rate of 0.5 mN/s, with a dwell time of 5 seconds at the maximum load. A 400X optical microscope attached to the NanoTest system was used to select appropriate individual fibres, with typical fibre-matrix distribution and no appreciable interface defects or damages, to be pushed out from the matrix.

The thickness of the composite specimens, at the location of the pushed-out fibre, were measured using an optical focus depth approach, using the onsite high-resolution optical microscope. To measure this, the microscope was first focused on the peaks of the sample support, and then the top surface of the selected fibre. By moving the samples, and focus point, away from the lens, it was possible to measure the local thickness of the composite material using the displacement change recorded for the sample stage holder. After completing the push-out tests, the specimens and the most representative fibres were observed on both, the top and back surfaces, using SEM imaging (JEOL 7000). Longitudinal cross-sectional cuts of the pushed-out fibre with the resin aside were performed using a dual-beam FIB-SEM (FEI Quanta 3D FEG), which made it possible to view the interface between the carbon fibre and the matrix.

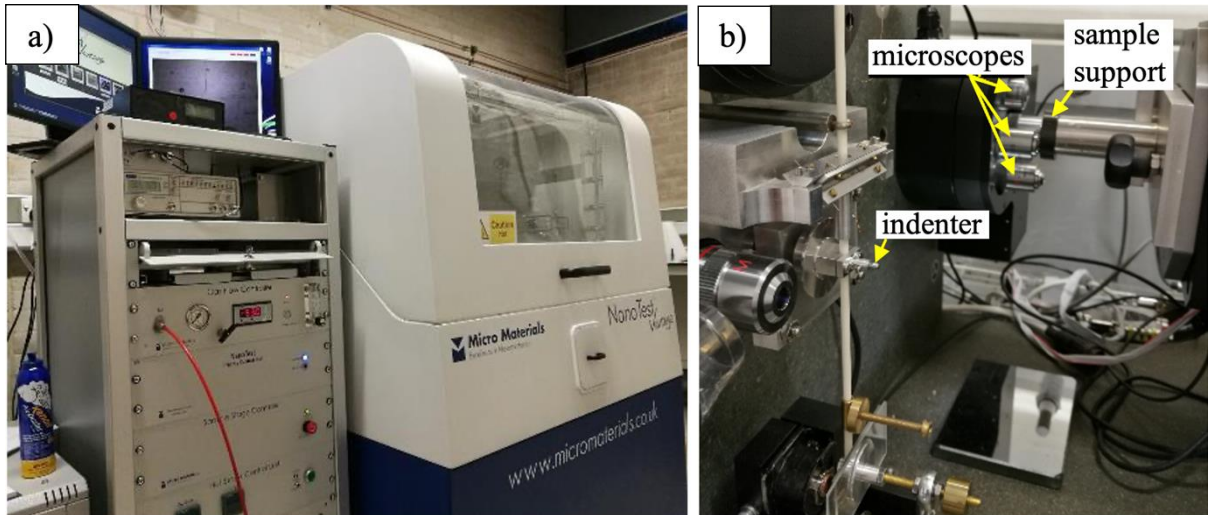


Figure 3.8 (a) Nano indentation equipment and (b) close look of indentation configuration.

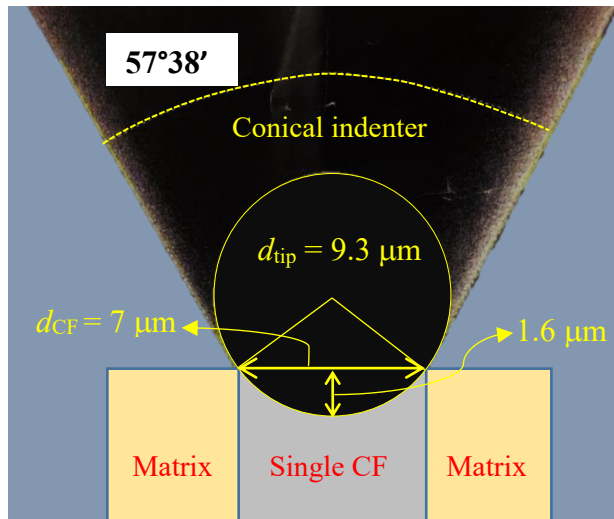


Figure 3.9 Geometry schematics of the conical indenter aligned with a single CF during the push-out test.

3.4.2.2 Evaluation of interfacial shear strength

The average interfacial shear stress at the fibre/matrix interface was calculated using the following equation,

$$\tau = \frac{F}{\pi dh} \quad (3-4)$$

where F is the load at the instance when the interfacial sliding occurs; d is the diameter of the fibre; h is the thickness of the sample; πdh is hence the contact area between the single fibre and the surrounding resin. Individual fibre diameters were measured from the SEM micrographs for each tested sample.

Although the failure mechanism of the fibre/matrix system is still a matter of debate, interface crack initiation and propagation are believed to be related to the randomly distributed defects on the CF surface and/or at the CF/matrix interface. The experimental work carried out within this study has revealed a certain level of distribution for the measured critical load. Therefore, the weakest-link theory can be adopted, and the Weibull distribution was applied in this research to statistically evaluate the probability of IFSS and describe its scattering. The cumulative probability of failure is given by

$$P_f = 1 - \exp(-(\tau/\tau_0)^m) \quad (3-5)$$

where τ is the shear strength; τ_0 is a Weibull scaling parameter and m is the Weibull modulus.

3.4.3 Nano-indentation creep test

Creep refers to the time-dependent deformation of material at constant stress below the yield stress of this material. To conduct the creep test with the nano-indentation system, a constant load was applied to the indenter and the change in indentation depth (displacement) was monitored as a function of time. Thus, after an individual fibre was identified, it was load-controlled to different peak loads (6 mN, 8 mN and 10 mN) at a loading rate of 0.5 mN/s. Following that, the individual fibre was held for 90 seconds with the peak load and then released. The test was carried out five times under the same conditions at room temperature

for each peak load and an average creep displacement and creep rate were used in the statistics. The indentation creep rate was calculated according to the following equation,

$$creep\ rate = \frac{d_1 - d_0}{d_0} \quad (3-6)$$

where d_0 is the indentation depth at the time of reaching the peak load (which is kept constant), nm; d_1 is the indentation depth at the end of dwell time of holding the constant test, nm; and the creep displacement is the difference of displacement ($d_1 - d_0$).

3.5 Evaluation of the mechanical properties of composites

3.5.1 Fabrication of CF reinforced composites

Unidirectional CF reinforced composites and woven carbon fabric reinforced composites were fabricated in this study to evaluate the mechanical properties of bulk composites. The unidirectional CF prepreg and composite specimens (14 layers of prepreg), as shown in Figure 3.10 (a) and (b), were produced using filament winding method with a MAW20FB5/1 winding machine. Woven carbon fabric reinforced laminate composite panels (Figure 3.10 (c)) were fabricated using resin transfer moulding (RTM) technique and then cut into specimens through water jet CNC machining according to the test requirements. The degassed resin was transferred into the mould cavity, where 8 piles of woven carbon fabrics (300 mm× 300 mm) were placed. The detailed fabrication procedures have been introduced in Section 2.3. All composites samples were cured in a furnace for 4 hours at 80 °C for 4 hours, and then post-cured at 140 °C for 4 hours, before cooling down to the room temperature. The epoxy resin used for all composite fabrication was the LY556 resin system from Huntsman.

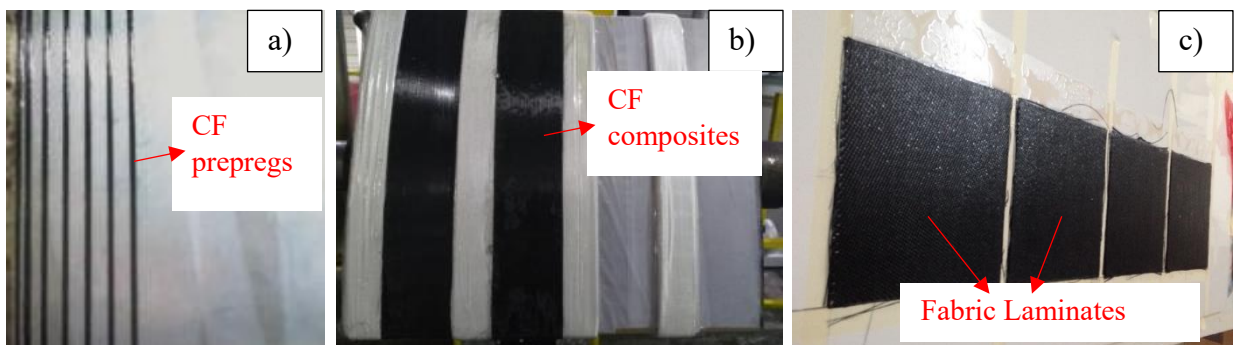


Figure 3.10 Images of (a) unidirectional CF prepregs, (b) unidirectional CF reinforced composites on winding mandrel and (c) woven carbon fabric reinforced laminate composite panels.

3.5.2 Tensile test

The tensile tests were conducted with the unidirectional CF preregs with a length of 250 mm and width of 15 mm using a TIRAtest Universal Testing Machine according to the ISO10618 standard. The ultimate breaking load was recorded with a dynamometer sensor. Each sample was fixed with grips (Figure 3.11) before the tensile load was applied at a speed of 40 - 50 mm/min. The tensile test was repeated five times for each type of specimen. The ultimate tensile strength (σ_t) was then calculated with the following formula:

$$\sigma_t = F_t \cdot \left(\frac{T_d}{\rho}\right) \quad (3-7)$$

where F_t is the breaking load at rupture, N; T_d is the linear density of dry fibre yarn, kg/m; and ρ is the fibre bulk density, kg/m³.

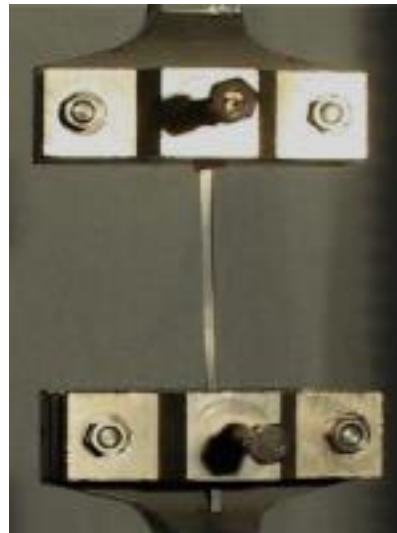


Figure 3.11 Images of unidirectional CF preregs on the tensile testing machine.

3.5.3 Short beam shear test

The short beam shear test was conducted with both unidirectional CF reinforced composite and woven carbon fabric reinforced composite specimens with dimensions of 60 × 15 mm

and 60 mm × 12.7 mm, respectively. The interlaminar shear strength of these samples was measured using the ASTM 2344 standard protocol. The shear test for each type of composites was repeated with five specimens and the stress was recorded using an analog compression force dynamometer sensor (Tiedemann Instruments). During the shear strength test, the composite specimens were broken into two segments, and the untouched fracture surfaces were observed under SEM imaging (Jeol 6060). The interlaminar shear strength (σ_s) was calculated using the following formula:

$$\sigma_s = 0.75 \times (F/(b \times h)) \quad (3-8)$$

where F is the maximum load observed during the test, N; b is the specimen width, m; and h is the specimen thickness, m.

3.5.4 Bending test

Three-point and four-point bending tests are widely used for prediction of flexural properties of the materials. They simulate tensile and compression stresses on the specimens and their physical response behaviour are monitored. The main difference between three-point and four-point bending tests are the location of the maximum bending stresses: the maximum stress occurs directly under the loading anvil in three-point loading, but is spread over the section of the beam between the loading points in the four-points system. The flexural strength of the composite specimens was obtained by the three-point bending test, which was performed by the project partner of National Technical University of Athens according to the ASTM D790 standard. The dimensions for unidirectional CF composite and woven carbon fabric composite specimens were 100 mm × 15 mm and 127 mm × 12.7 mm, respectively. At least five specimens were tested for each kind of composite and the bending

stress was recorded with an analog compression force dynamometer sensor (Tiedemann Instruments). The maximum flexural strength (σ_f) was calculated using formulae:

$$\sigma_f = 3FL/2bh^2 \quad (3-9)$$

where F is the breaking load, N; L is the support span, m; b is the specimen width, m; and h is the specimen thickness, m.

3.5.5 Mode I interlaminar fracture test

Mode I interlaminar fracture tests were conducted using a universal testing machine (INSTRON) using a load cell of 500 N, and according to the ASTM D5528 standard. Double cantilever beam (DCB) specimens (width 25 mm and length 200 mm), as shown in Figure 3.12, were cut from the cured laminates prepared with pristine and ASPN5 modified woven fabrics. The side edge of each specimen was coated with white correction fluid to simultaneously facilitate the measurement of the delamination length. A thin polytetrafluoroethylene (PTFE) film was embedded at the mid-plane to form an initiation site for the delamination. Two piano hinges were bonded to the delaminated arms of the DCB specimen to facilitate the opening, then the load was applied to the DCB specimen perpendicular to the plane. The specimens were loaded and unloaded in two cycles at a constant crosshead speed of 2 mm/min. The initial loading was stopped after a 3-5 mm pre-crack was made from the top of the insert film. The specimens were then reloaded until the desired delamination crack length was achieved (100 mm). Visual initiation value (VIS), at which the delamination was visually observed to grow, was recorded during the loading process. 5 specimens were tested for each type of composites.

According to the Modified Beam Theory (MBT), the critical energy release rate G_{IC} is given as:

$$G_{IC} = \frac{3F\sigma}{2b(a + |\Delta|)} \quad (3-10)$$

where F is the crack initiation load value (VIS point), N; σ is the load-displacement at this point, m; b is the specimen width, m; a is the delamination length, m; and Δ represents the rotation correction of DCB arms at delamination front, determined experimentally from the plot of the cube root of the compliance, $(\sigma/P)^{1/3}$ as a function of delamination length a .



Figure 3.12 Images of (a) DCB specimen with piano hinges and (b) image of crack propagation during loading of Mode I interlaminar fracture toughness experiment.

3.5.6 Internal pressure destructive test

3.5.6.1 Propellant tank manufacture

Two propellant tanks were manufactured by research collaborators (YUZHNOYE, Ukraine) mainly using filament winding technique with 9000-m-long pristine CFs and ASPN5 treated CFs. As shown in Figure 3.13 (a), firstly, the structural shell of the propellant tank was made by winding the carbon yarns on a metal mandrel. After curing, the metal mandrel was removed from the structural shell and carbon plastic covers (Figure 3.13 (b)) were glued to the ends of the structural shell. Then, the propellant tank as shown in Figure 3.13 (c) was manufactured by winding the fibres yarns (9000-m-long) to the structural shell and cured. The obtained tanks were quality controlled by thermographic and ultrasound techniques (Figures 3.13 (d) and (e)).

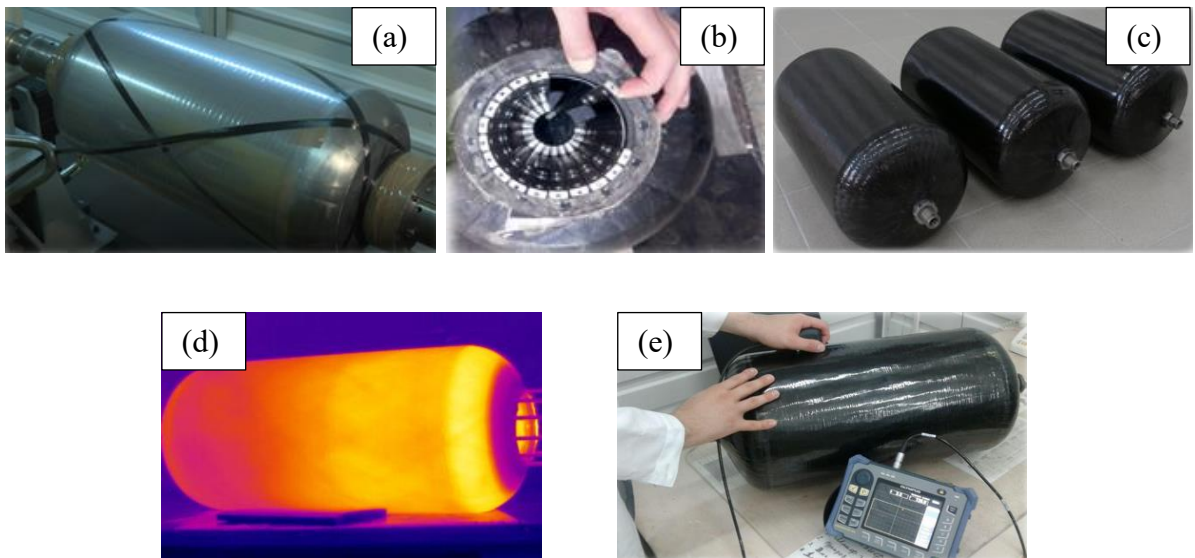


Figure 3.13 Images of (a) structure shell on the metal mandrel; (b) carbon plastic covers; (c) propellant tanks; (d) thermographic control and (e) uniformity control by ultrasound.

3.5.6.2 Test procedure

The internal pressure destructive test procedure is illustrated in Figure 3.14 (c). Prior to the internal pressure destructive test, 16 strain sensors, as shown in Figures 3.14 (a) and (b), were attached at different locations (central and ends) on the outside layer of the tank in the longitudinal and transversal directions in order to measure the deformations during the test. After hanging the tank on the purpose-made support, the test pressure was continuously and evenly applied using the air supply station connected a pipe on the top of the tank until the tank was destroyed. The pressure and strain as a function of time were monitored using sensors throughout the test.

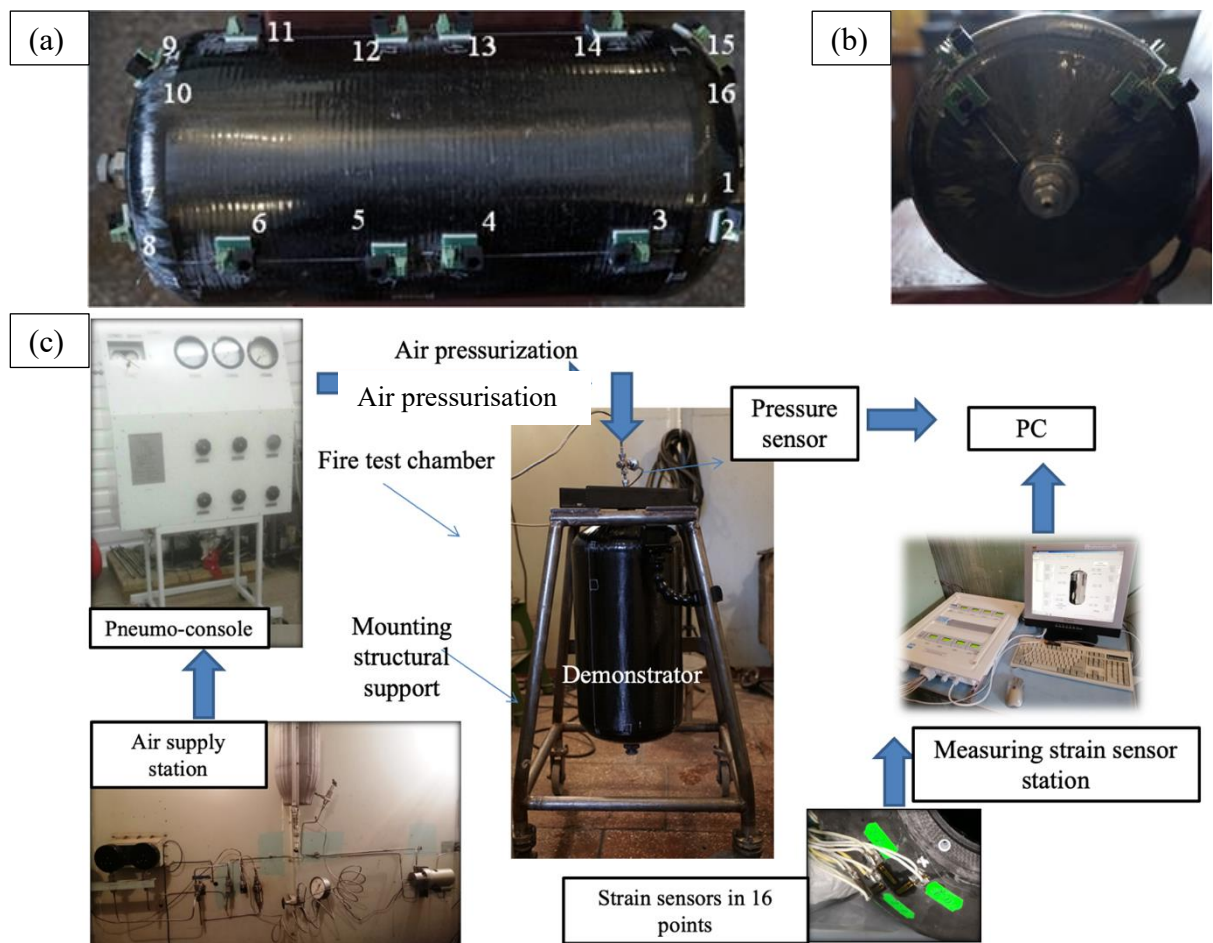


Figure 3.14 Images of (a) and (b) strain sensors on the tank outside layer and (c) internal pressure destructive test scheme.

CHAPTER 4 RESULTS AND DISCUSSION

This chapter presents the results of active screen plasma modification of CFs, including surface morphology, microstructure, surface chemistry, wettability and mechanical properties, which are reported in Section 4.1 and Section 4.2. Then the investigation of the interface between the modified CFs and the epoxy resin is reported in Section 4.3. The effect of active screen plasma modification on CF reinforced composites is finally reported and interpreted in Section 4.4.

4.1 Morphology, structure and chemistry

The interfacial property of fibre reinforced composites is usually attributed to physical, chemical and mechanical interactions between the reinforcing fibres and the matrix resin [161, 162]. For a given resin, the interfacial property is determined by the surface morphology, the surface microstructure, the surface functional groups, the surface free energy and the surface wettability by the resin. This section presents the first part of the surface characteristics, including the surface morphology (Section 4.1.1), the microstructure (Section 4.1.2-4.1.3) and the surface chemistry (Section 4.1.4).

4.1.1 Surface morphology

The surface morphologies of the pristine and the de-sized CFs observed by SEM are displayed in Figure 4.1-1. As expected, the surface of the pristine CF presented ridges and striations parallel to the fibre axial direction owing to the PAN manufacturing process even it is sized [163]. The de-sized fibre surface was stuck by some gel-like sizing materials after de-sized with acetone for 24 hours at 45 °C.

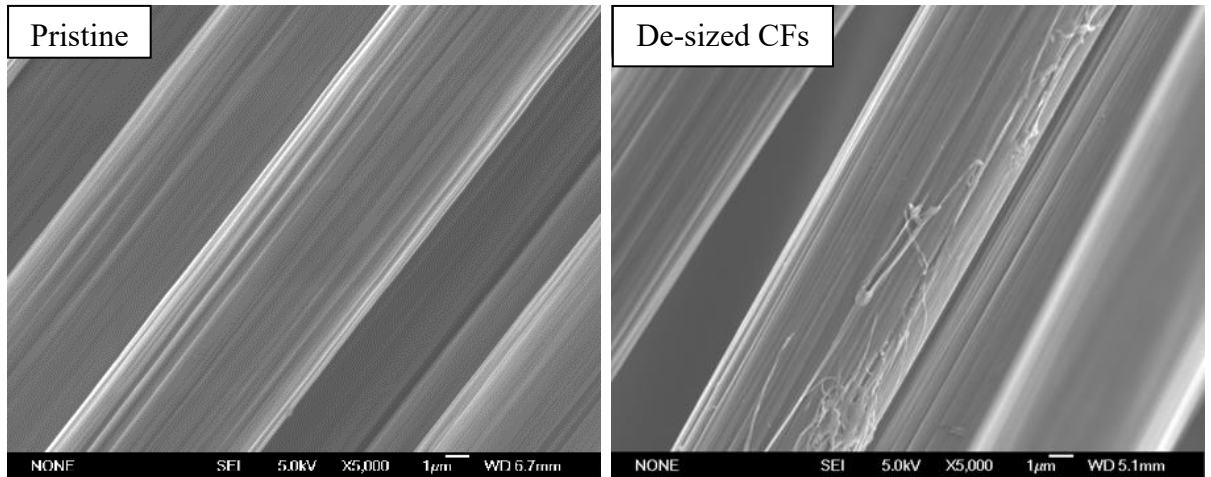


Figure 4.1-1 Surface morphologies of pristine and de-sized CFs observed by SEM.

The surface morphologies of ASP treated CFs are presented in Figure 4.1-2. It can be seen that after ASPN treatment for two minutes (ASN2), most sizing coating materials on the CFs were partially removed with some sizing patches remaining on the surface. After ASPN treatment for five minutes, no sizing patches could be observed under high magnification (5000X) SEM from the surface of the CFs (see ASPN5). No noticeable further changes could be clearly seen from the 8-minute ASPN treated CF surfaces (ASPN8) or all ASPAr treated surfaces.

Further AFM analysis (Figure 4.1-3) of the samples confirmed the above findings. The surface of the pristine CFs is fully covered by the sizing layer. While deep and wide grooves were revealed on the surface of ASPN5 treated CFs with limited sizing patches remaining. However, the surface of ASPAr5-10% treated CFs showed dense and well-defined grooves with only very limited sizing traces. This indicates that the surfaces of the treated fibres are rougher than that of the pristine CFs and the plasma treatments with both nitrogen and argon (i.e. ASPAr5-10%) produced a stronger effect on the surface morphology change as compared with using nitrogen (i.e. ASPN5).

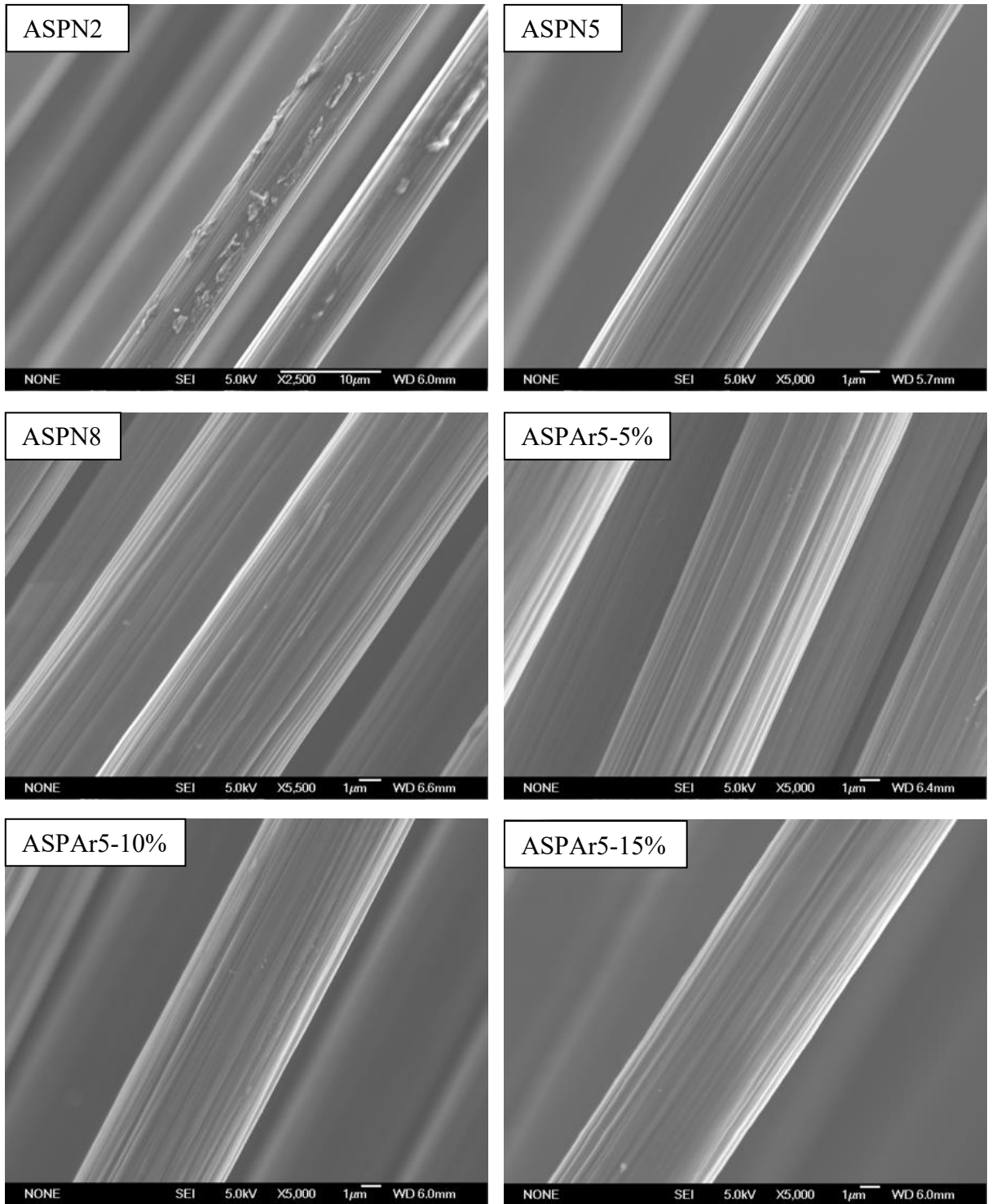


Figure 4.1-2 Surface morphologies of ASP treated CFs observed by SEM.

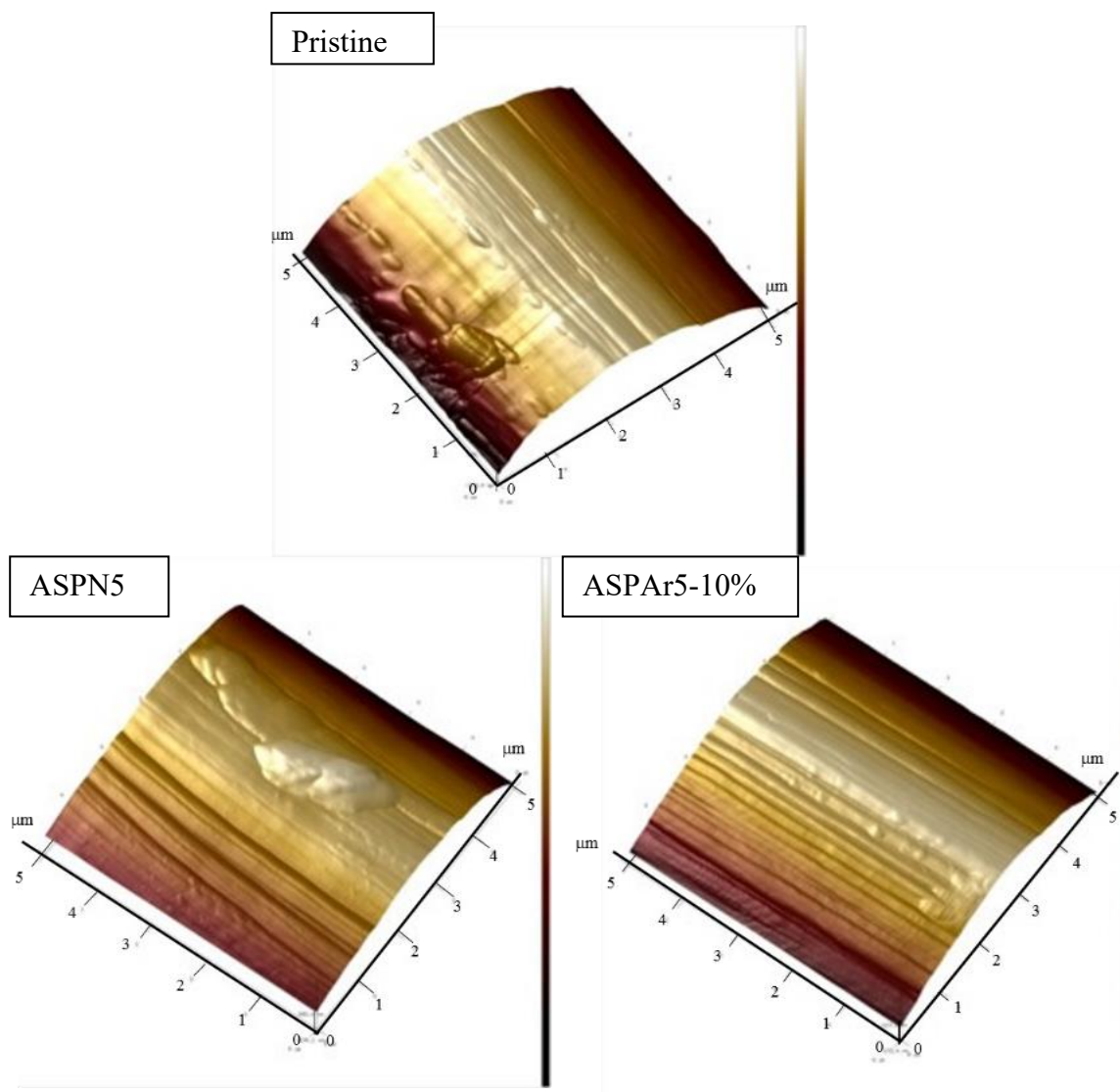


Figure 4.1-3 Surface morphologies of pristine, ASPN5 and ASPAr5-10% treated CFs observed by AFM.

Table 4.1-1 lists the diameters of the pristine and the ASP treated CFs measured from the SEM images. It can be found that the diameters of the ASPN treated CFs decreased when increasing the treatment duration from 2 minutes to 8 minutes. The 8-minute treatment produced a 3% decrease in the average diameter than the pristine one. The diameters of the ASPAr treated CFs with less concentration of argon (ASPAr5-% & ASPAr5-10%) exhibited similar values to the ASPN5 treated ones. While the higher concentration of argon (ASPAr5-

15%) in the treatment resulted in the minimal decrease in the diameter, implying that the argon has less impact on the diameter of CFs than the nitrogen. Overall, the diameter changes of CFs after ASP treatments were not significant, as examined by t tests [164] (Table 4.1-1). These minor changes are related to the removal of sizing layers and the potential etching effect from the ASP treatments.

Table 4.1-1 Diameters of the pristine and ASP treated CFs.

Sample code	Mean (μm)	Deviation	<i>P</i> (t test)
Pristine	6.76	0.32	-
ASPN2	6.63	0.33	0.22
ASPN5	6.62	0.25	0.11
ASPN8	6.55	0.29	0.15
ASPAr5-5%	6.66	0.26	0.16
ASPAr5-10%	6.63	0.28	0.16
ASPAr5-15%	6.73	0.25	0.17

4.1.2 Distortion of CF surface after ASP treatments

Raman spectroscopy is one of the most effective tools to detect the changes in the fibre surface structure and/or disorder formations following treatments. The recorded Raman spectra of the pristine and the ASP treated CFs are presented in Figure 4.1-4. As typical Raman spectrum described elsewhere [12, 165], two broadened bands exhibit on all spectra. Both bands on the spectra of ASPN treated samples are similar to these bands on the pristine CF spectrum, but sharper than bands on ASPAr treated samples. These spectra were fitted by a set of Gaussian functions as exemplified in Figure 4.1-5. In the case of ASPN5 CFs, two bands were identified on the spectrum in the region of 800-2000 cm^{-1} . The one at around 1400 cm^{-1} is D band, which is related to structural disorders on the fibre surface,

i.e. nitrogen/oxygen functional groups and structure defects [166]. The other at around 1600 cm^{-1} is G band, which is relating to the graphite carbon structure, arising from the intrinsic bond stretching of sp^2 carbon atoms [167]. The intensity ratio of the D to G bands (I_D/I_G) is hence usually used to quantify the disorder degree in carbon materials.

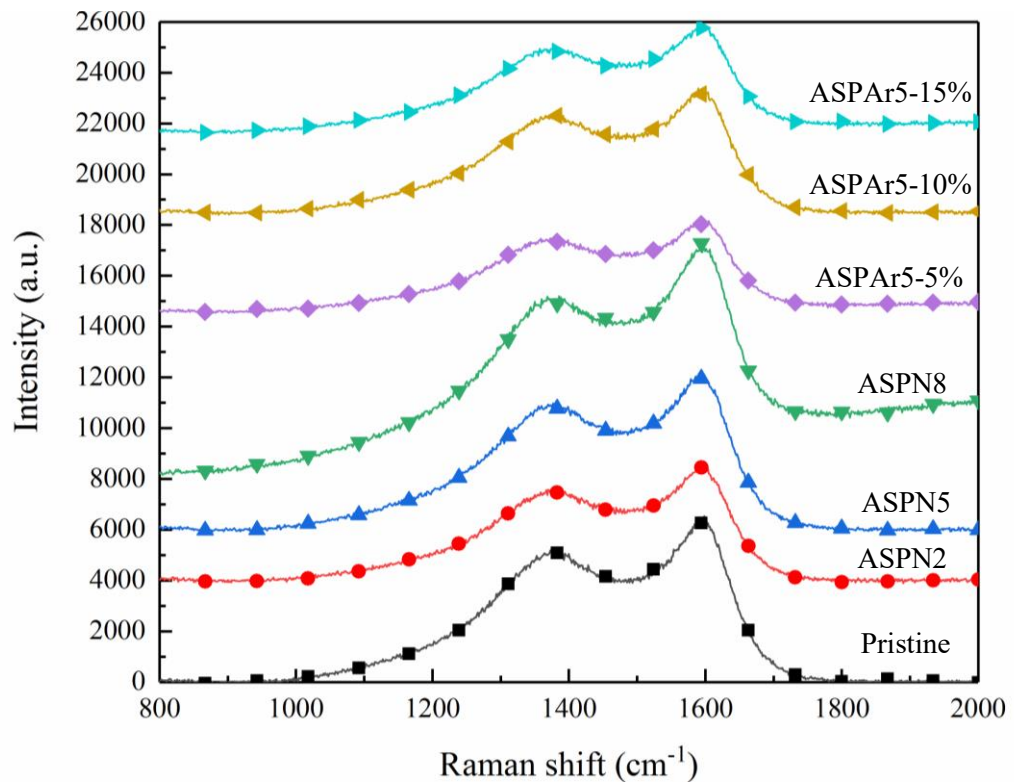


Figure 4.1-4 Raman spectra of pristine and active screen plasma treated CFs.

All Raman spectra have been peak-fitted with the mixed Gaussian-Lorentzian function as exemplified by the ASPN5 spectrum shown in Figure 4.1-5 and the relative band parameters are summarised in Table 4.1-2. The average values and standard deviations of the positions and widths (full width at the half maximum) of the two bands were calculated from 5 measurements at different sites on the fibre surface. For the ASPN treated CFs, in general, the position of D band shifted to a higher wavenumber and the width of D band increased with increasing the treatment time. The position and width values for 2-minute treated

samples (ASPN2) are almost identical to that of pristine CFs. This is mainly because the surface of the CFs has not been fully cleaned within the first two minutes, which is supported by the surface morphologies of ASPN2 shown in Figure 4.1-2. It can be also found from Table 4.1-2 that for longer time treated samples (ASPN5 & ASPN8), the D band shifted to a higher wavenumber and the D band width reduced with the treatment time. However, the position of the G band of short time treated ASPN2 CFs shifted to a slightly lower wavenumber. The intensity ratios (I_D/I_G) for ASPN5 and ASPN8 treated CFs were slightly increased or the same respectively relative to that of the pristine CFs. However, the I_D/I_G ratio of the short-time ASPN treated ASPN2 CFs was reduced to 1.002 from 1.014 for the pristine CFs. When argon was introduced into the ASPN treatments, both D and G bands shifted slightly to the lower wavenumbers. For example, D and G bands shifted from 1394.6 cm^{-1} and 1595.5 cm^{-1} in the spectrum of ASPN5 CFs to 1389.5 cm^{-1} and 1594.2 cm^{-1} respectively with 5% argon introduced (ASPAr5-5%). Meanwhile, the widths of D and G bands decreased for the ASPAr treated CFs except for G band width for ASPAr5-10% treated CFs. However, no clear trend could be identified for the effect of argon concentration on the position and width of treated CFs. All the I_D/I_G values for the ASPAr treated fibres were smaller than that of the pristine CFs and followed a decreasing trend with the Ar percentages.

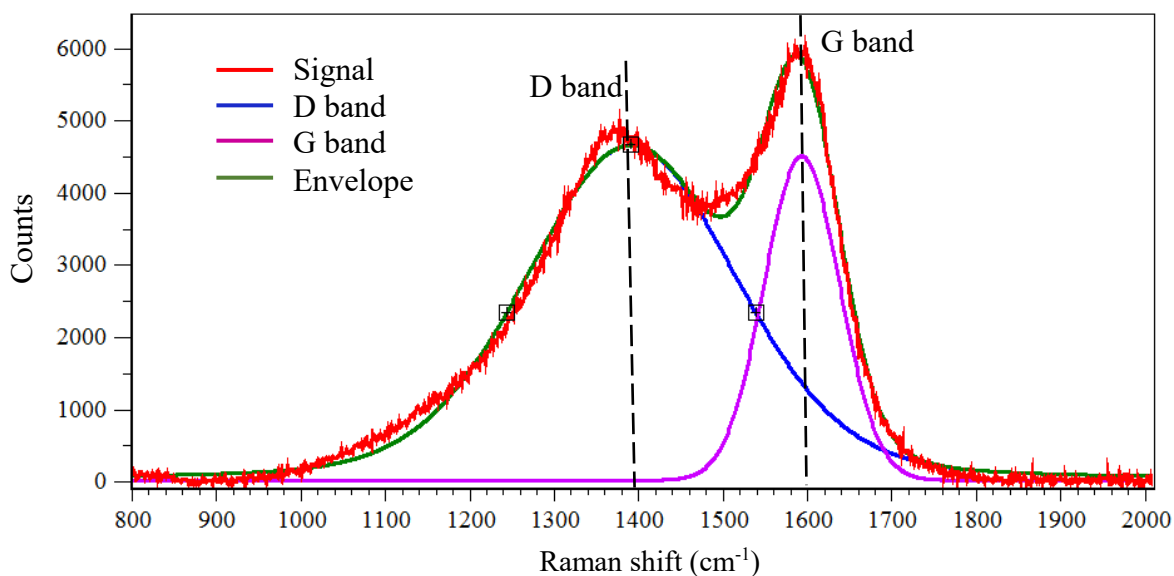


Figure 4.1-5 Peak fitting for Raman spectrum of ASPN5 treated CFs under Gaussian-Lorentzian function for D and G bands.

Table 4.1-2 Positions and widths of the D and G bands and the corresponding I_D/I_G ratio (standard deviations given in brackets).

Sample code	D band		G band		I_D/I_G
	Position [cm ⁻¹]	Width [cm ⁻¹]	Position [cm ⁻¹]	Width [cm ⁻¹]	
Pristine	1392.9 (0.59)	289.7 (2.21)	1595.2 (0.20)	105.3 (0.39)	1.014 (0.0179)
ASPN2	1392.5 (0.79)	289.3 (1.73)	1595.0 (0.29)	104.7 (0.46)	1.002 (0.0002)
ASPN5	1394.6 (3.06)	296.7 (3.68)	1595.5 (1.70)	104.8 (0.84)	1.018 (0.01273)
ASPN8	1395.0 (1.04)	295.1 (3.92)	1595.6 (0.64)	103.7 (0.78)	1.014 (0.0068)
ASPAr5-5%	1389.5 (0.88)	285.5 (1.30)	1594.2 (0.80)	104.7 (0.47)	1.009 (0.0149)
ASPAr5-10%	1392.9 (0.96)	289.3 (3.62)	1594.6 (0.33)	105.6 (0.94)	1.005 (0.0135)
ASPAr5-15%	1390.3 (1.49)	293.5 (2.12)	1594.5 (0.08)	104.2 (0.08)	1.004 (0.0078)

4.1.3 Change of CF turbostratic structure by ASP treatments

XRD diffraction patterns of ASP treated CFs, compared with that for pristine CFs are shown in Figure 4.1-6 (a). It can be seen that the (002), (100) and (101) peaks are revealed on the patterns of all types of CFs (Reference code: 00-041-1487).

The peak (002), which reflects the pseudo-graphitic structure of CFs, is very broad and shows an appreciate asymmetry on both pristine and treated CFs, indicating the presence of a certain amount of disorder in their structure (turbostratic structure). The peak (100) shown on pristine CFs faded away and overlapped with peak (101) on the XRD patterns of treated CFs, except for the 2-minutes treatment (ASPN2). Specifically, for ASPN treatments, these peaks for 2-minutes treated CFs were similar to that of the pristine CFs in terms of shape and position. When the treatment duration was increased to 5 minutes, the intensity of peak (002) decreased and the peak (100) faded away. Further increasing the treatment time to 8 minutes led to the right-shift and intensity increase of both peaks (002) and (101).

There is no significant variation of the XRD patterns among the ASPAr treated CFs and the XRD patterns of them are similar to that of ASPN5 treated CFs. Peaks (103), (110) and (112) at around 64.8° , 77.2° and 83.2° respectively, as shown in Figure 4.1-6 (b), became shaper after ASP treatments, especially in the case of ASPN8. This phenomenon again implies that a certain amount of disorder was created by ASP treatments and more disorder was found following the longer treatment time.

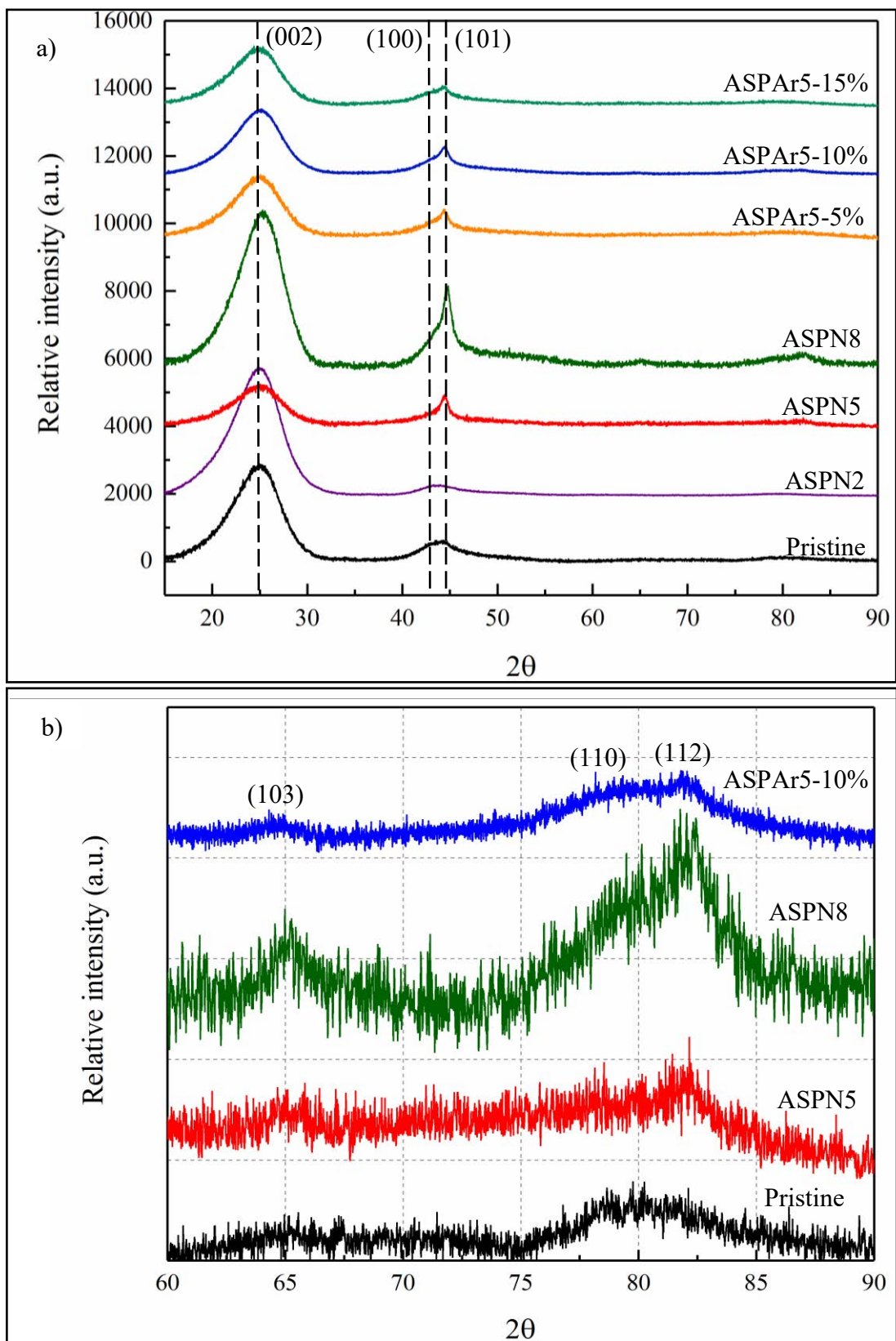


Figure 4.1-6 XRD patterns of (a) pristine and ASP treated CFs and (b) XRD patterns at higher 2θ values.

The parameters (band width at half peak maximum) of the (002) and (10) peaks were used to calculate the crystal size parameter L_c (crystallite height) and L_a (crystallite width), and the results are listed in Table 4.1-3, together with the peak position and width.

Table 4.1-3 XRD structure parameters (standard deviations given in brackets).

Sample code	Peak (002)			Peak (10)			L_a/L_c
	2θ [degree]	Width [nm]	L_c [nm]	2θ [degree]	Width [nm]	L_a [nm]	
Pristine	24.60 (± 0.011)	6.09 (± 0.027)	1.32	43.98 (± 0.054)	4.44 (± 0.131)	3.95	2.99
ASPN2	24.58 (± 0.004)	6.27 (± 0.010)	1.28	44.17 (± 0.012)	4.98 (± 0.033)	3.52	2.75
ASPN5	24.72 (± 0.017)	5.83 (± 0.042)	1.38	44.19 (± 0.024)	3.01 (± 0.058)	5.82	4.21
ASPN8	25.01 (± 0.014)	5.47 (± 0.034)	1.47	44.54 (± 0.014)	2.78 (± 0.036)	6.31	4.29
ASPAr5-5%	24.63 (± 0.011)	5.99 (± 0.022)	1.34	44.10 (± 0.024)	3.91 (± 0.077)	4.48	3.34
ASPAr5-10%	24.65 (± 0.010)	6.02 (± 0.024)	1.34	44.12 (± 0.027)	3.98 (± 0.065)	4.41	3.29
ASPAr5-15%	24.47 (± 0.008)	6.03 (± 0.020)	1.33	44.01 (± 0.030)	3.99 (± 0.073)	4.39	3.30

It can be seen that for the longer treatments (ASPN5, ASPN8 & ASPAr), the peak width values for peak (002) decreased; the fading away of the peak (100) caused by these treatments made the width values of peak (10) much smaller than that of the pristine CFs; both crystallite height L_c and width L_a increased and more growth occurred in crystallite width L_a . For example, the increase of L_a is more than 30 and 23 times of that of L_c for the ASPN5 and ASPAr5-10% treated CFs respectively. The ratio of L_a/L_c increased as well, indicating that distorted microstructures with significantly increased crystallite size were

formed on the CF surface after the activation process and that more distortion happened along the basal planes for treated CFs. Another observation from Table 4.1-3 is that the addition of argon increased the crystallite width values for both (002) and (10) peaks, reduced the L_c , L_a values and the L_a/L_c ratio when comparing the ASPN5 and ASPAr5-5% treated CFs. However, further increasing the concentration of argon in the ASPAr treatments (ASPAr5-10% & ASPAr5-10%) did not change these values significantly.

4.1.4 Surface chemistry

The surface chemistry of pristine and ASP treated CFs was examined by XPS and the typical survey spectra in the binding energy ranging 0-1200 eV are shown in Figure 4.1-7. The main resonance peaks are labelled C 1s, N 1s and O 1s. The peaks observed in higher binding energy were attributed to Auger effect.

The quantified analysis in terms of the atomic content is summarised in Table 4.1-4, revealing a slight increase in the carbon content after both ASPN and ASPAr treatments. The nitrogen and the oxygen contents of the pristine CFs were attributed to the sizing layers, which can be largely removed by 5 minutes ASP treatments as illustrated in Section 4.1.1. Thus, the increased nitrogen content of ASPN5 CFs would be associated with the introduction of the N atoms by ASPN5 treatments. This is supported by the fact that less nitrogen content can be detected on the ASPAr5-10% CFs, because the nitrogen/hydrogen was partially replaced by argon during the ASPAr5-10% treatments. The oxygen content on the surface of both ASPN 5 and ASPAr5-10% treated CFs were from the remaining sizing on the surface of CFs and the oxidation of free radicals on the treated CF surfaces when exposed to air after the treatments. In the XPS investigation, the changes of O/C and N/C atomic ratios suggest the surface activity of CF. As revealed in Table 4.1-4, the N/C ratio

derived from the XPS data shows a significant increase after the ASPN5 treatment, implying that nitrogen-functionalised groups were introduced during the treatment. However, the N/C ratio of the ASPAr5-10% CF and the O/C ratios of ASP treated CFs were a little lower than that of pristine CF.

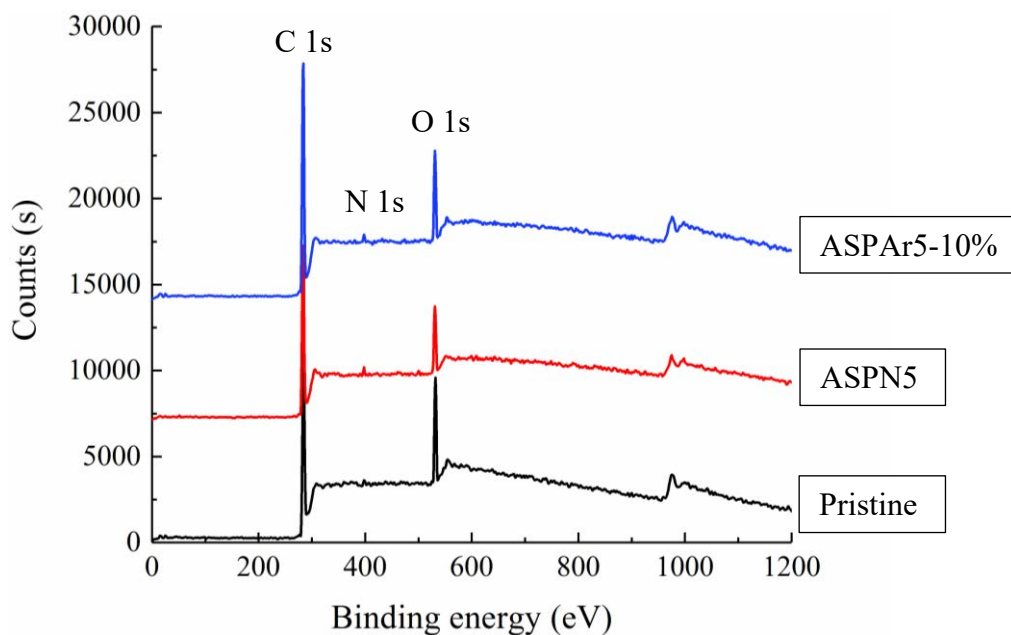


Figure 4.1-7 XPS surface survey spectra of pristine, ASPN5 and ASPAr 5-10% treated CFs.

Table 4.1-4 XPS chemical quantification of pristine and ASP treated CFs.

Sample code	C 1s (%)	N 1s (%)	O 1s (%)	N/C (%)	O/C (%)
Pristine	81.1	1.4	17.5	1.7	21.6
ASPN5	81.4	3.7	14.9	4.5	18.3
ASPAr5-10%	82.4	0.9	16.7	1.1	20.3

The high-resolution spectra corresponding to the C 1s, N 1s and O 1s regions of the pristine, ASPN5 and ASPAr5-10% CFs are depicted in Figures 4.1-8, 4.1-9 and 4.1-10, respectively.

From Figure 4.1-8, the C 1s signal of the pristine CFs presented a tailing toward high binding energy, which became less distinct after the plasma treatments. This could be partially attributed to the chemical shift of photoelectron peaks associated with functionalised carbons and partially to the sizing layer on the pristine fibre surface. Carbon atoms differ in their binding energies because of their connection with different atoms (oxygen, hydrogen or nitrogen) by different covalent bonding (a single bond or a double bond). Thus, the C 1s region was de-convoluted into two functional groups C-C and C-O with binding energies at about 284.5 and 286.2 eV respectively. The intensity of peak assigned to the latter functional group of the treated CFs was lower than that of the pristine CFs, especially in the case of the ASPN5 treated CFs.

The O 1s XPS spectrum of pristine CF, shown in Figure 4.1-9, presented one sharp peak, which became wider after the ASP treatments. This can be attributed to the two functional groups of C-O and -OH with binding energies at about 531.1 and about 531.5 eV, respectively. The peak intensity of fibres varied with different treatments. For the ASP treated CFs with the addition of 10% argon, the intensity of peak assigned to C-O group increased while -OH group decreased.

The most noticeable change in the spectra is observed in the N 1s region, where the intensity of the signal increased after both the ASPN5 and the ASPAr5-10% treatments, and the shape of the peaks changed significantly. These changes should be attributed to the introduction of N-containing groups by ASP treatments. As shown in Figures 4.1-10 (b) and (c), pyrrolic N and oxidised N groups are exhibited on both ASPN5 and ASPAr5-10% treated fibre surfaces with the corresponding binding energies at around 400.1 and 401.8-402.8 eV. Pyridinic N with binding energy at 398.6 eV can be only found on the surfaces of ASPAr5-10% treated CFs.

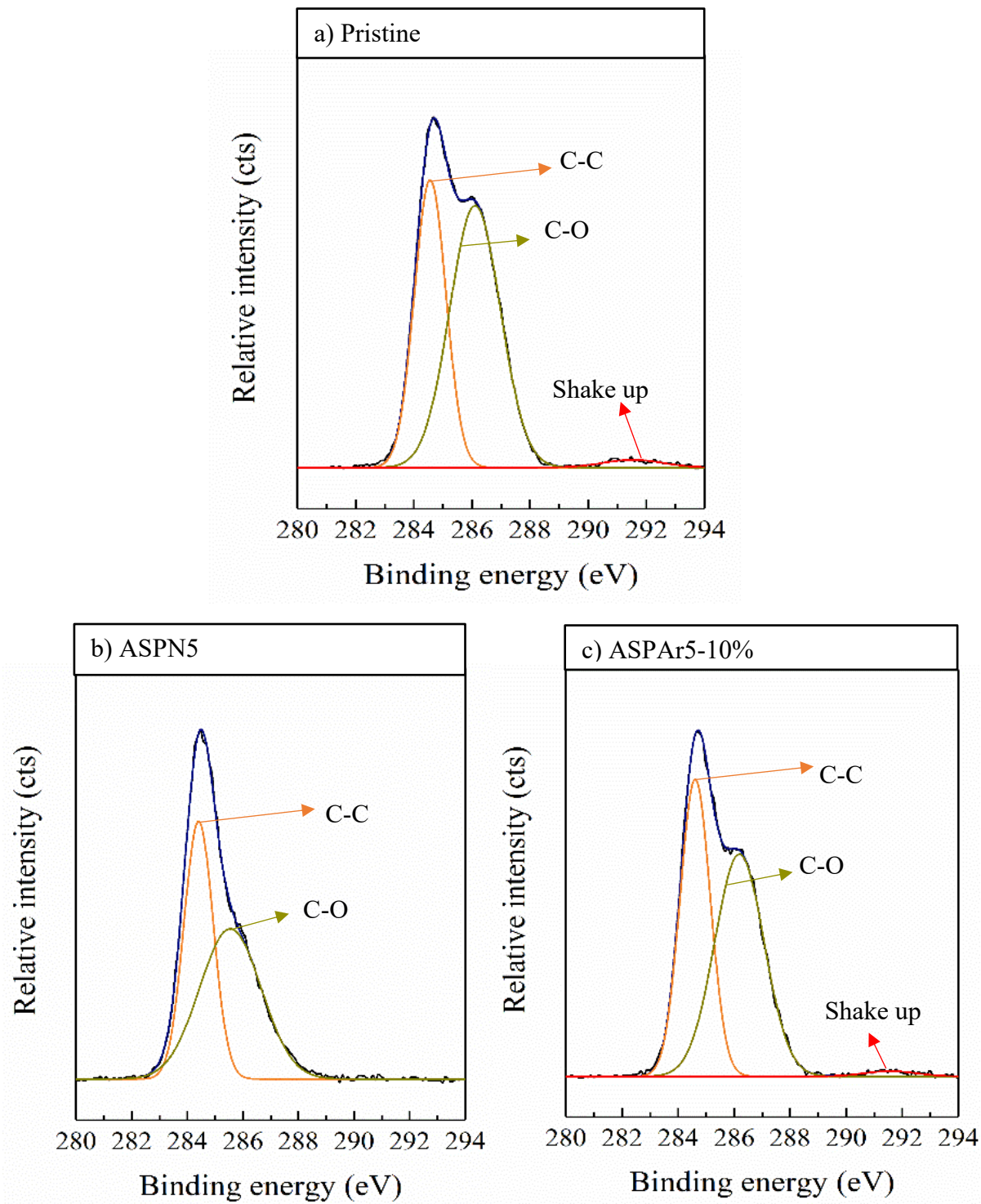


Figure 4.1-8 High-resolution XPS spectra deconvolution into surface functional groups for C 1s peaks area.

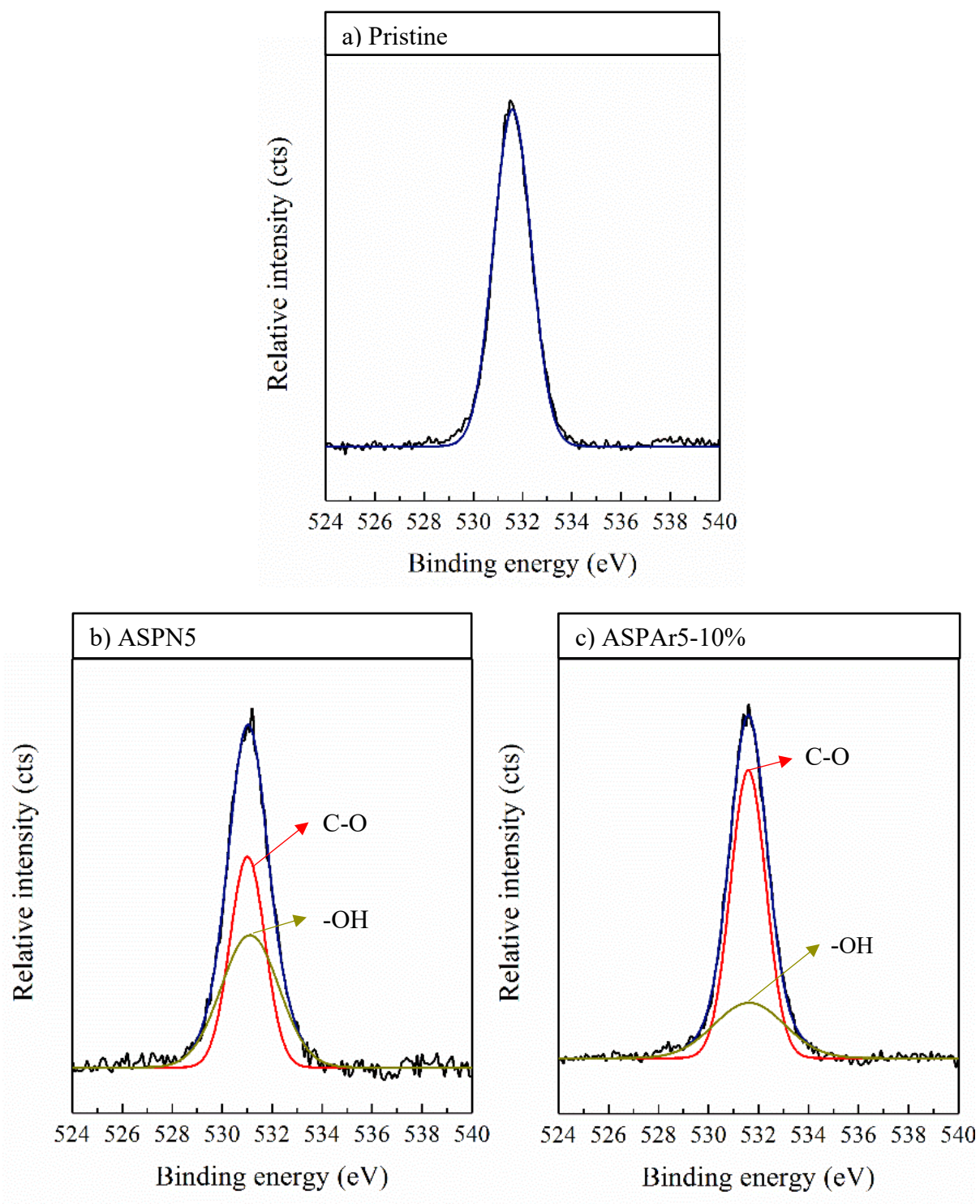


Figure 4.1-9 High-resolution XPS spectra deconvolution into surface functional groups for O 1s peaks area.

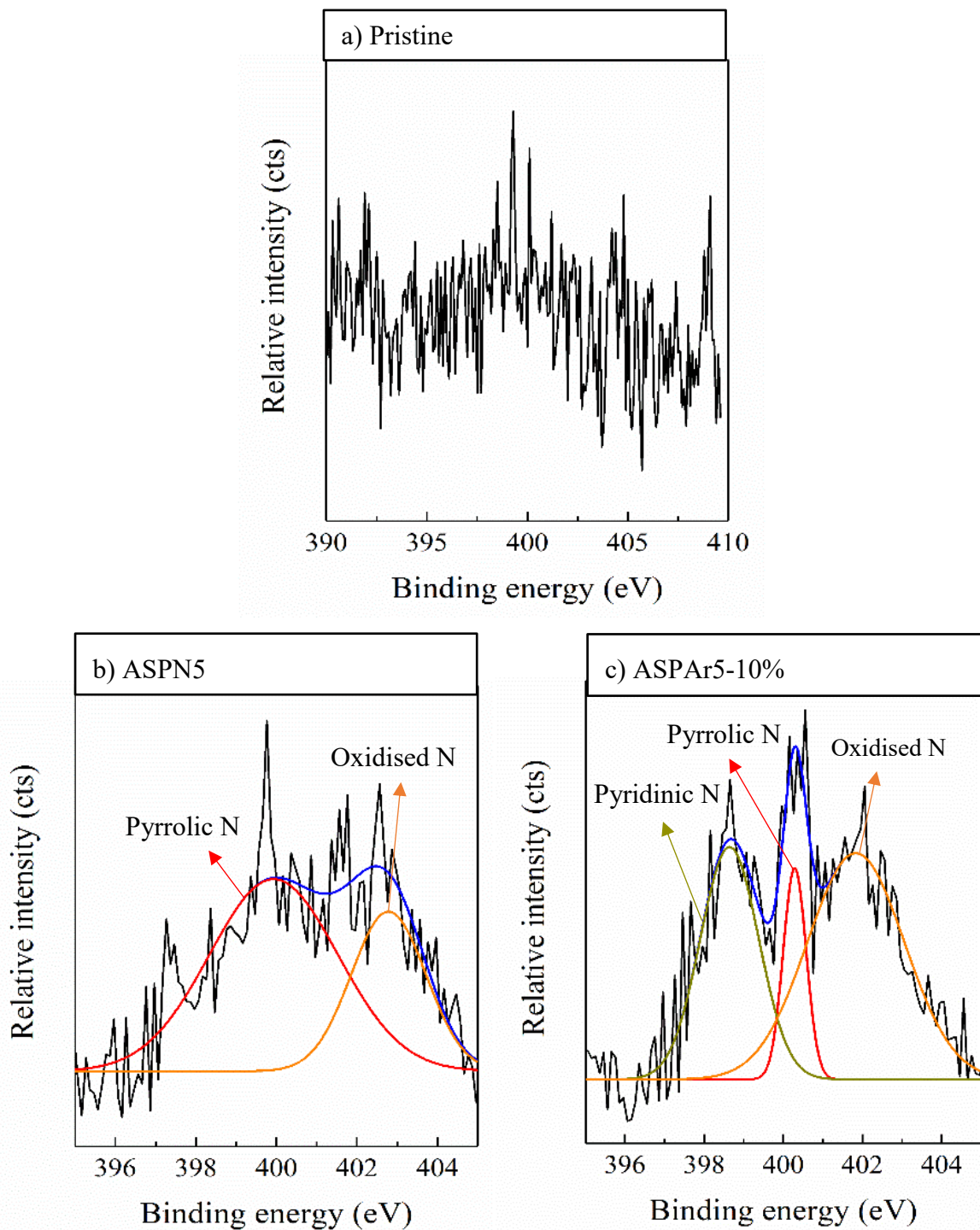


Figure 4.1-10 High-resolution XPS spectra deconvolution into surface functional groups for N 1s peaks area.

4.2 Mechanical property and surface hydrophilicity

This section reports the surface wettability of CFs before and after ASP treatments by measuring their contact angles with epoxy resin (Section 4.2.1) and measuring their water adsorptions (Section 4.2.2). This section also presents the results of tensile strength for single fibres and fibre bundles before and after ASP treatments (Section 4.2.3).

4.2.1 Surface wettability and durability

As described in Section 3.3.6, the contact angle measurements were conducted on the pristine and ASP treated CFs with resin micro-droplets. The images of resin micro-droplets on single fibres treated by different conditions and the measured contact angles are shown in Figure 4.2-1. As can be seen clearly, all ASP treatments have resulted in decreased contact angles when compared to the pristine CFs, indicating increased wetting properties by all ASP treatments. For the ASPN treatments, the 2-minutes treatment produced the most hydrophilic surfaces with a contact angle of 57.4° (ASPN2). The contact angle increased to 59.7° and 60.1° when the treatment duration was prolonged to 5 (ASPN5) and 8 minutes (ASPN8), respectively. When nitrogen-hydrogen in the treatments was partially replaced by argon with the percentages of 5%, 10% and 15% (ASPAr), the contact angles changed from 59.7° (ASPN5) to 58.4° (ASPAr5-5%), 60.0° (ASPAr5-10%) and 58.8° (ASPAr5-15%). No obvious trend can be found regarding the relationship between the contact angles and the concentration of argon used in the treatments.

Also, the representative images of resin micro-droplets in Figure 4.2-2 revealed the evolution of contact angle of ASPN5 treated CFs over time. It can be seen that the contact angle of ASPN5 treated CFs increased from 59.7° to 62.5° after exposure in air for 10 days. Same tests were conducted for all treated CFs and their changes over time are illustrated in

Figure 4.2-3 and Table 4.2-1. Obviously, such evolution can be found in all types of ASP treated CFs, but more changes are observed on the CFs treated with argon addition (i.e., ASPAr). For example, the degradation rate on contact angle over 10 days increased from 4.76% (ASPN5) to 5.04% when 10% argon was added to the treatment (ASPAr 5-10%). This is an indication that the ASP treated CFs presented a hydrophobic recovery over time when the treated surface was exposed to air for 10 days and the introduction of argon in the treatments promoted the hydrophobic recovery.

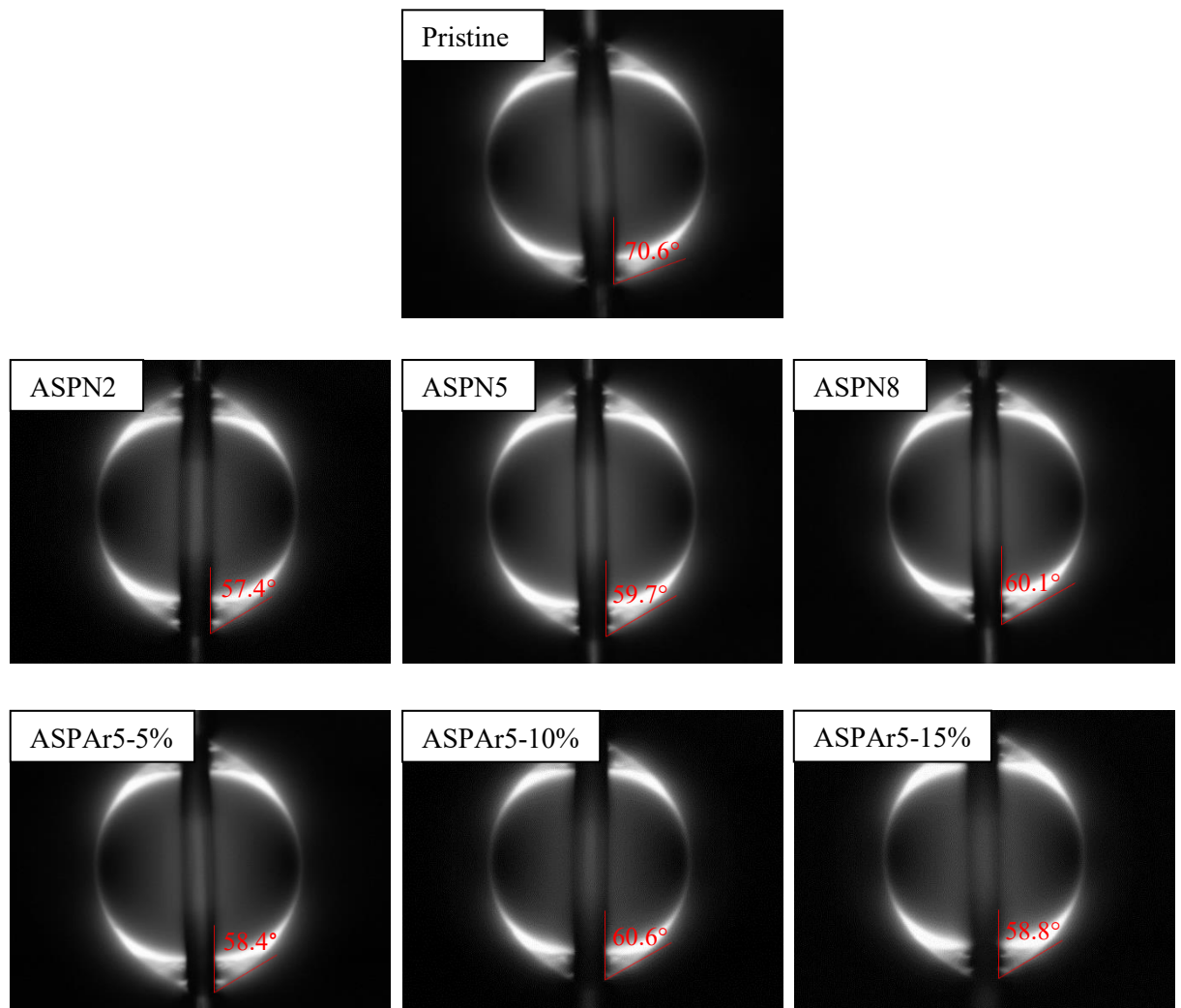


Figure 4.2-1 Optical microscope images of the resin droplets on single fibres for pristine and ASP modified CFs with average contact angles.

Another observation from the Table 4.2-1 is that the ASPN8 treated CFs experienced the least degradation during the 10 days, which could be related to the increased amount of functional groups introduced by longer active screen plasma treatment (8 minutes).

It is important to mention that the micro-droplets radius exhibits quite large standard deviations and the measurements were conducted both on large and small micro-droplets. However, for a given CFs, the contact angle of each measurement was almost constant, and the difference was within the experimental error.

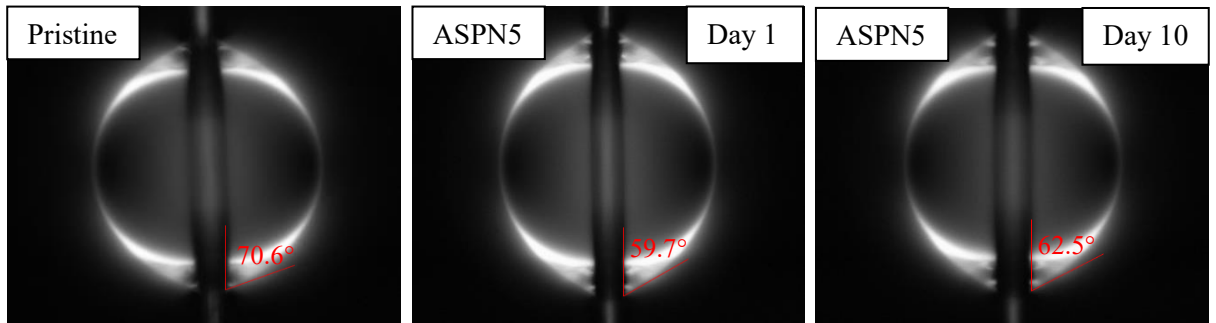


Figure 4.2-2 Evolution of the contact angle of ASPN5 treated CFs. The samples were subsequently aged in air for 10 days.

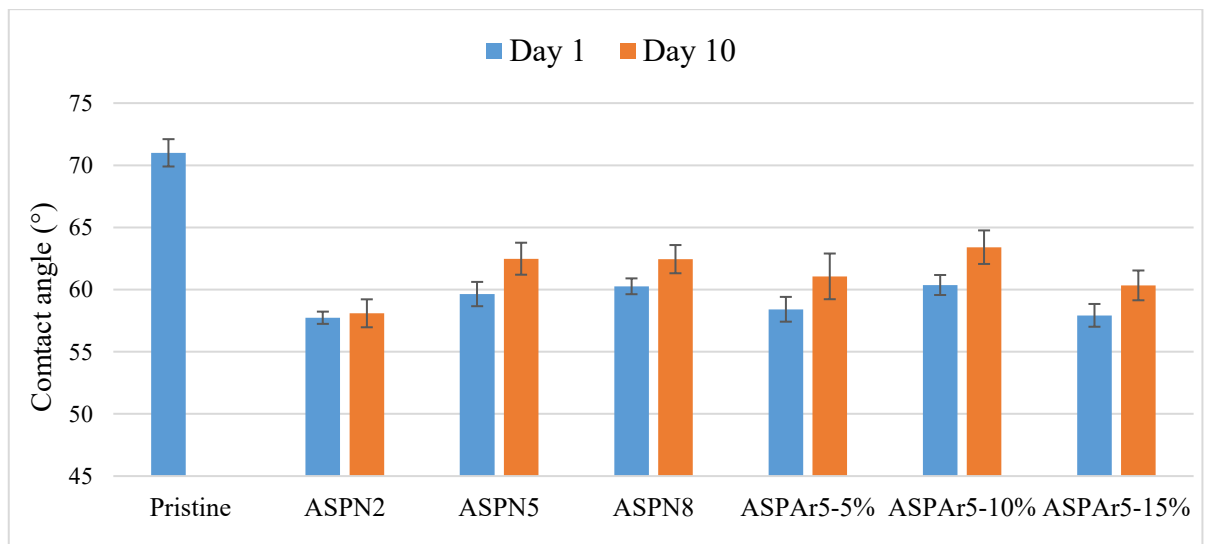


Figure 4.2-3 Contact angles for the pristine and ASP modified CFs on day 1 and day 10.

Table 4.2-1 Degradation rates on contact angle of different ASP treatments after 10 days.

Sample code	Degradation rate (%)
ASPN2	0.62
ASPN5	4.76
ASPN8	3.62
ASPAr5-5%	4.53
ASPAr5-10%	5.04
ASPAr5-15%	4.16

4.2.2 Surface water-sorption behaviour

The affinity of CFs to water following ASP treatments was investigated by the dynamic vapour sorption (DVS) technique. Figure 4.2-4 shows the images of CFs taken before feeding into the sample pan for DVS testing and after testing (adsorption and desorption processes). No obvious damage or change was observed.

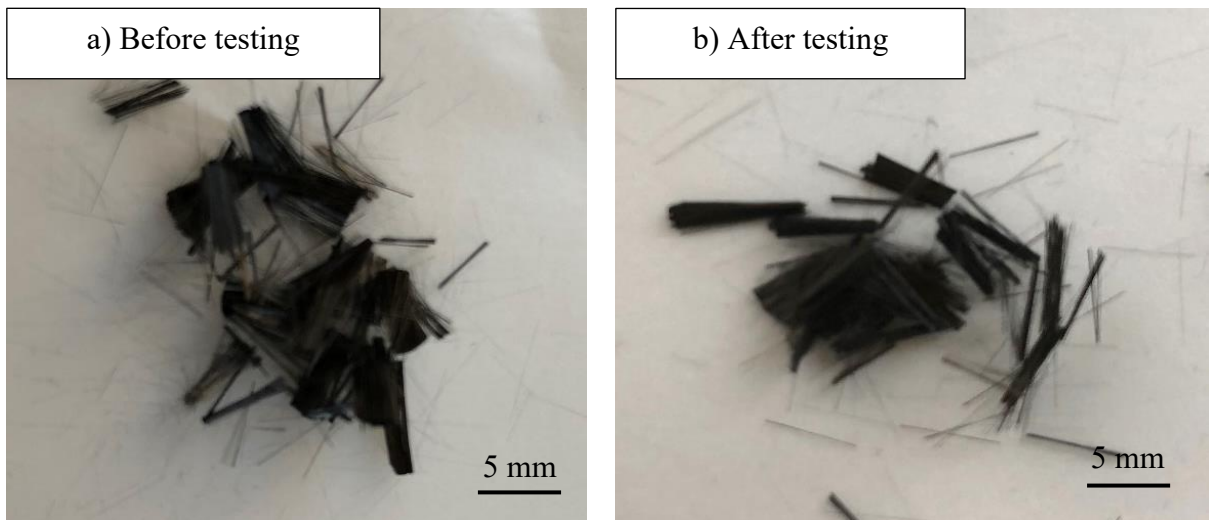


Figure 4.2-4 Images of CFs (a) before testing and (b) after testing.

Figure 4.2-5 shows the measured water-uptake variation with time at the relative humidity of 60% and 0% for the pristine and ASP treated CFs, manifesting the adsorption process and

desorption process. It can be seen that the actual relative humidity for the adsorption and desorption processes is very stable and slightly higher than the pre-set humidity values of 60% and 0%.

The water sorption process is mainly dominated by the water-functional groups (chemisorption) and the water-water interactions (physisorption) [168]. That is, water clusters are initially formed via hydrogen bonding on the functional groups, which act as nucleating sites for water molecules to adsorb, followed by water cluster growth, filling micro-pores and coalescence. Thus, the adsorption branches of all CFs show a steep increase with increasing of the relative pressure at the beginning and then reach plateaus (adsorption isotherm), implying that all the chemisorption sites were occupied by water molecules and all the micro-pores and/or striations on the fibre surfaces were filled by water through capillary condensation. Then, as the relative humidity dropped to 0%, the water condensate became unstable and desorbed by means of molecular evaporation, leaving only water molecules that were bonded directly to the chemisorption sites. Thus, the water uptake decreased immediately at the beginning of the desorption process for all types of CFs and then reached the other plateaus, which were desorption isotherms.

As can be seen from Figure 4.2-5, all the treated CFs showed a higher water uptake throughout the whole process and a longer evaporation period at the beginning of the desorption process when compared to the pristine CFs. This is an indication that the ASP treatments increased the hydrophilicity of the CF surface, with the ASPAr5-10% treatment being the most effective in enhancing the hydrophilicity of CFs. However, comparing to the pristine and ASPAr5-5% treated CFs, the ASPN5 and ASPAr5-10% treated fibres took longer time to reach the adsorption isotherm, showing uphill on the curve of the adsorption

part. This different behaviour on water adsorption of treated carbon fibres is associated with the surface morphology and surface reactivity.

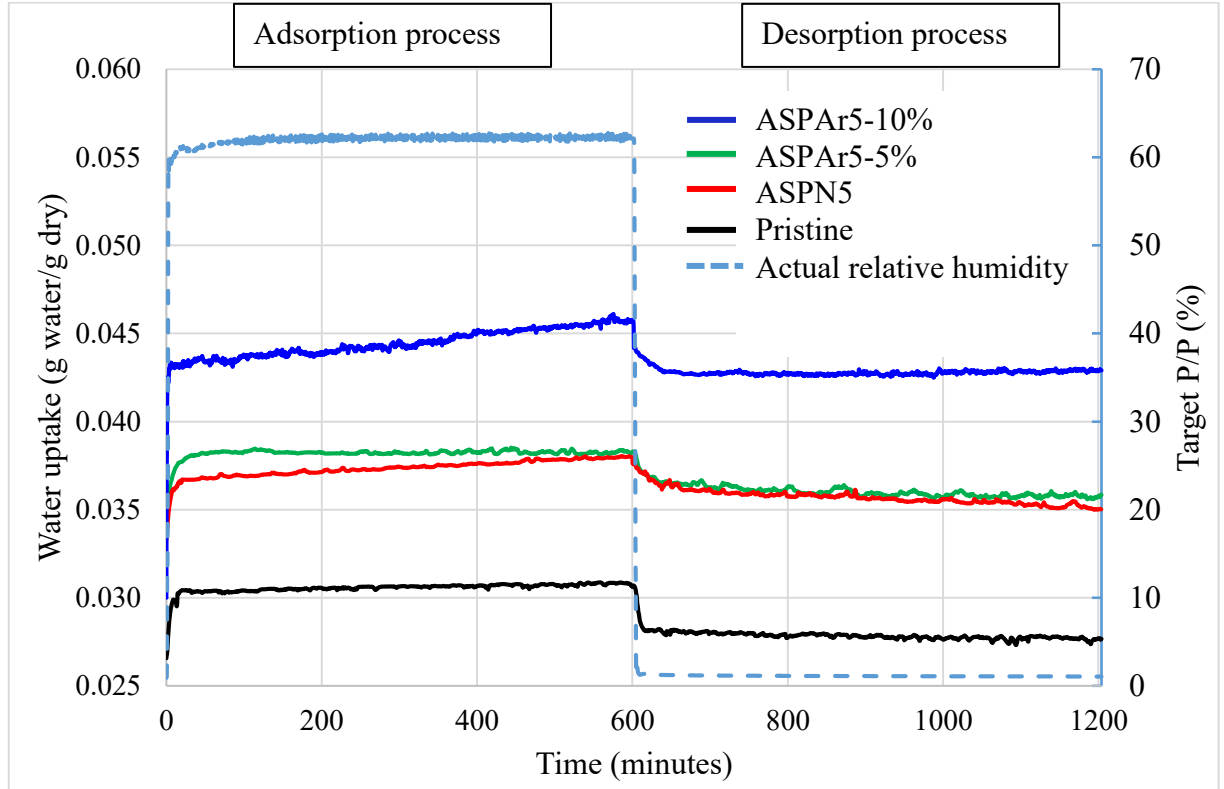


Figure 4.2-5 Dynamic vapour adsorption and desorption of pristine and ASP treated CFs within 20 hours at room temperature (25°C).

The curves in Figure 4.2-6 were obtained 60 days after the ASP treatments (exposure in air). It can be seen that the ASP treated CFs still exhibited improved hydrophilicity as compared with the pristine CFs. In the case of ASPN5 CFs, its adsorption isotherm plateau seems to almost overlap with that of the pristine CFs. But the plateau of desorption isotherm remains higher than that of pristine CFs, implying that a certain amount of water was chemisorbed to the ASPN5 treated CFs. The random fluctuations on the sorption curve of ASPAr5-5% CFs are likely a result of variation of temperature or floor vibrations. The improved hydrophilicity of ASP treated CF surface (freshly treated and aged) could be attributed to the introduced functional groups and their surrounding carbon atoms, whose affinity toward

water was increased because of the polarisation effects of introduced nitrogen (nitrogen and oxygen have stronger electron negativity than carbon). The more hydrophilic surfaces resulted in a larger absorptive capacity for water in ASP treated samples than in pristine CFs.

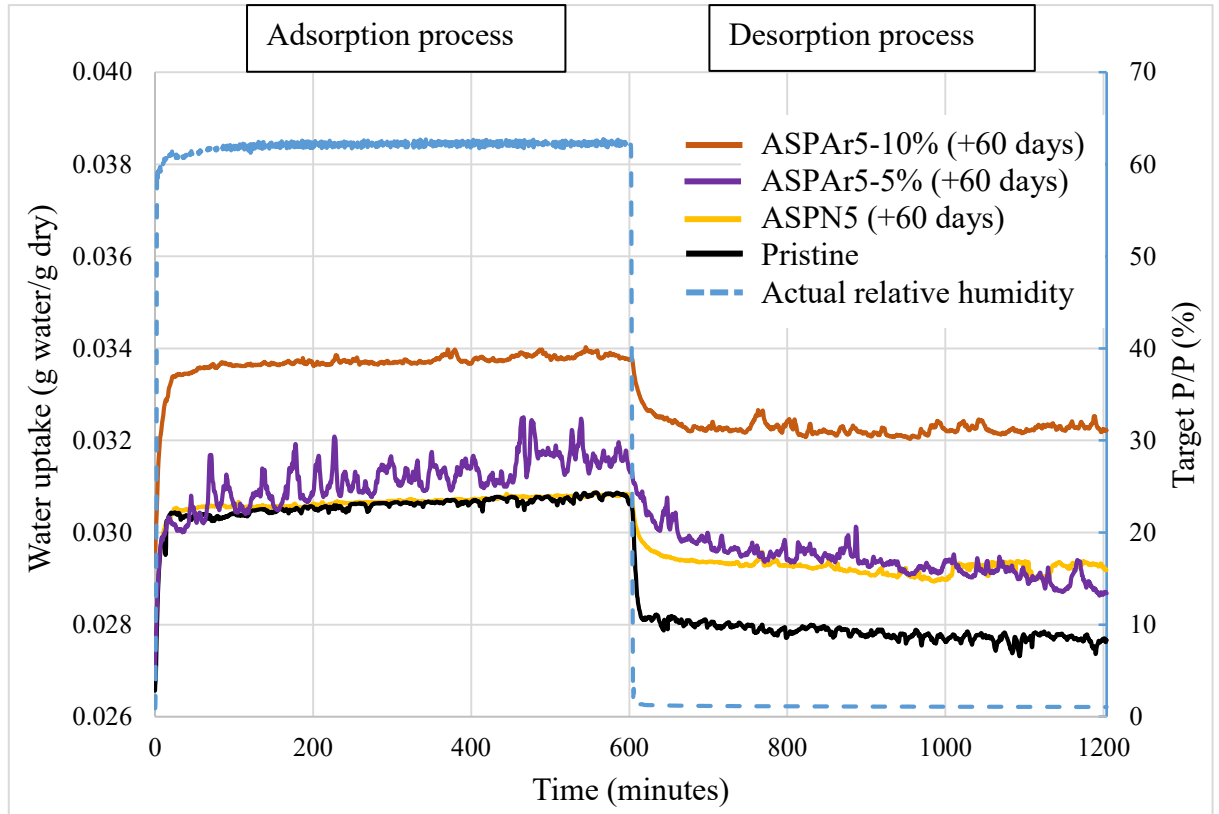


Figure 4.2-6 Dynamic vapour adsorption and desorption of aged pristine and ASP treated CFs (after 60 days) within 20 hours at room temperature (25°C).

Further quantitative analysis of the DVS data has been conducted based on the following calculation and the results are summarised in Table 4.2-2. The average water content (%) is defined based on the dry mass of the CFs as follows:

$$\text{Average water content} = \frac{M_{ad/de} - M_d}{M_d} \quad (4-1)$$

where M_{ad} is average mass during adsorption process, mg; M_{de} is average mass during desorption process, mg; and M_d is the dry weight after the preheat process, mg.

The chemisorption (%), which is the percentage of water molecules bonded directly with the functional groups, and the physisorption (%), i.e., the percentage of water molecules absorbed through the water-water interaction and evaporated after the desorption process, can be calculated as follows [169]:

$$\text{Chemisorption} = \frac{M_{de}}{M_d} \quad (4-2)$$

$$\text{Physisorption} = \frac{M_{ad} - M_{de}}{M_d} \quad (4-3)$$

From Table 4.2-2, it can be seen that the average water content for the adsorption process increased from 3.06 % for pristine CFs to 3.74 % for ASPN5, 3.82 % for ASPAr5-5% and 4.46 % for ASPAr5-10% CFs. After desorption process, the average water content dropped to 2.79 %, 3.57 %, 3.36 % and 4.38 % for pristine, ASPN5 ASPAr5-5% and ASPAr5-10% CFs, respectively. Clearly, the ASP treated CFs exhibited greater water content and chemisorption of water molecules, which indicates that more water molecules were adsorbed on the ASP treated CF surface than on the pristine CF surface. The addition of 10% argon in the ASP treatments produced the highest chemisorption of water. On the contrary, the physisorption of water decreased after all these ASP treatments. This is believed to be associated with the sizing layers on the pristine CFs and the change of surface morphology caused by the mild chemical etching of hydrogen (Figure 4.1-2). The water-sorption behaviour of the aged ASP treated CFs (60 days) shown in Table 4.2-2 demonstrates that the aged ASP treated CFs still exhibited better water-sorption properties than the pristine CFs but worse than the freshly ASP treated CFs, indicating that the introduced functional groups underwent an aging process after exposure in the air for 60 days.

Table 4.2-2 Summary of DVS tests for freshly treated and aged pristine, ASP treated CFs.

Sample code	Test time	Dry weight, M_d (mg)	Average water content (%)		Chemisorption (%)	Physisorption (%)
			Adsorption	Desorption		
Pristine		9.98 ± 0.00	3.06 ± 0.02	2.79 ± 0.02	2.79	0.27
ASPN5	1	9.75 ± 0.00	3.74 ± 0.04	3.57 ± 0.04	3.57	0.17
ASPAr5-5%	day	9.77 ± 0.00	3.82 ± 0.02	3.58 ± 0.03	3.36	0.22
ASPAr5-10%		10.02 ± 0.00	4.46 ± 0.08	4.38 ± 0.02	4.38	0.17
ASPN5	60	9.87 ± 0.00	3.07 ± 0.02	2.93 ± 0.04	2.93	0.14
ASPAr5-5%	days	9.80 ± 0.00	3.11 ± 0.09	2.94 ± 0.07	2.94	0.16
ASPAr5-10%		10.02 ± 0.00	3.37 ± 0.03	3.23 ± 0.04	3.14	0.14

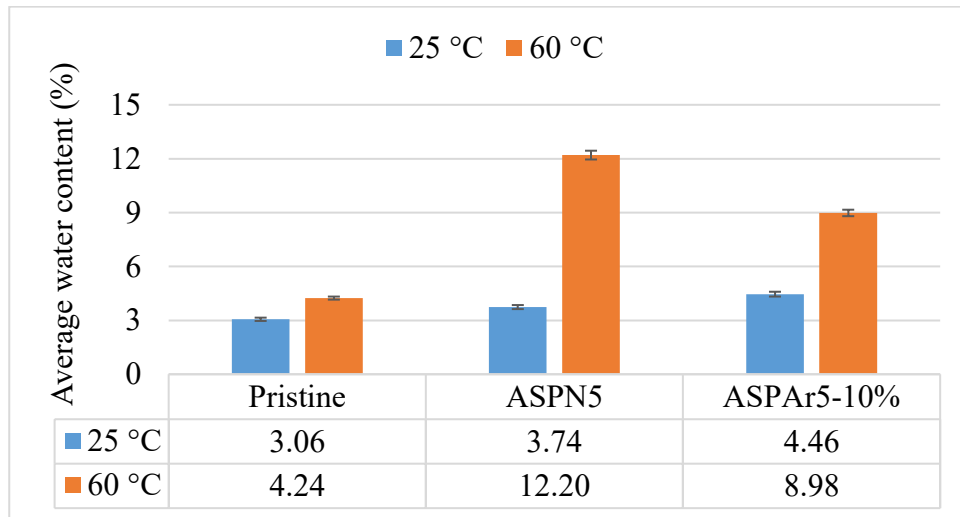


Figure 4.2-7 Average moisture absorption content of pristine, ASPN5 and ASPAr5-10% treated CFs at 25 °C and 60 °C.

The average water adsorbed contents at 60 °C were collected for the pristine, ASPN5 and ASPAr5-10% CFs as well. As can be seen obviously from Figure 4.2-7, the average absorbed water content increased from 3.06%, 3.74% and 4.46% to 4.34%, to 12.20 % and 8.98 % for pristine, ASPN5 and ASPAr5-10% treated CFs respectively when the adsorption

temperature was raised from 25 °C to 60 °C. The ASPN5 treatment produced the greatest increase in absorbed water content as temperature increased.

4.2.3 Tensile strength

Weibull distribution is often used as a good representation of fibre strength distribution and can be applied to estimate the tensile properties. Weibull plots for pristine and ASP treated CFs in this research were fitted using a two-dimensional Weibull statistical method. The Weibull cumulative probability of failure for each fibre strength value was plotted as a function of the logarithm of fibre strength in order to produce the Weibull plot. Such Weibull plots and the fitted straight lines for the tensile tested single fibres in this work are presented in Figure 4.2-8 and the results of the Weibull statistical analysis for all samples are summarised in Table 4.2-3. It can be seen that the Weibull plots are almost linear, and all the fitting coefficient values R^2 are all over 92%, signifying that the tensile strength of all CFs followed a Weibull distribution. The shape parameter m (or Weibull modulus) indicates the slope of the fitted lines and denotes the scattering of the single fibre tensile strength. As shown in Table 4.2-3, the values of the m decreased after all ASPN treatments, in which ASPN8 CFs showed the greatest reduction. For the ASPAr treated CFs, the m values were increased when comparing to that of the pristine sample except for the ASPAr5-10% treated samples, whose m value is close to that of the pristine CFs.

The tensile strength of the ASPN treated CFs increased before the treatments were prolonged to 8 minutes. This could be attributed to the change of the surface turbostratic structure and the increased crystalline components. While prolonged plasma exposure could introduce surface defects thus leading to a lower tensile strength (i.e., ASPN8).

The tensile strength of all ASPAr treated CFs increased compared to the pristine CFs. Experiment with 5% of argon (ASPAr5-5%) in gas mixture produced the most promising increase in tensile strength. Further increase in the argon percentage did not increase the strength further. It is also clear that the tensile strength of the ASPAr treated CFs is higher than that of ASPN treated ones. This should be attributed to the addition of argon to the gas mixture.

The single fibre tensile strength test and Weibull distribution were applied to the de-sized single CFs as well. As we can see from Table 4.2-3, the shape parameter m of the de-sized CFs was almost the same as that of the pristine CFs. While the tensile strength of the de-sized single fibres decreased significantly, which could be attributed to the fibre damage introduced by the de-sizing procedure.

Table 4.2-3 Summary of results from the Weibull analysis of single fibre tensile tests.

Sample code	Intercept	Slope/ m	δ_0 (GPa)	R^2
Pristine	-29.70 ± 1.85	3.81 ± 0.24	2.41	0.92
De-sized CFs	-28.04 ± 1.78	3.81 ± 0.25	1.57	0.94
ASPN2	-23.64 ± 0.84	2.98 ± 0.11	2.81	0.97
ASPN5	-26.27 ± 1.06	3.35 ± 0.14	2.56	0.96
ASPN8	-20.85 ± 0.58	2.73 ± 0.08	2.07	0.98
ASPAr5-5%	-40.93 ± 2.25	5.06 ± 0.28	3.27	0.94
ASPAr5-10%	-30.33 ± 1.31	3.79 ± 0.17	3.00	0.96
ASPAr5-15%	-31.34 ± 1.94	3.94 ± 0.25	2.83	0.92

Tensile tests were conducted on the CF bundles of selected treatments to further examine the influence of ASP treatments on a larger scale. The maximum load and the average tensile strength of CF bundles are presented in Table 4.2-4. It can be seen that the maximum load

for tensile tests of fibre bundles increased from 350.99 N for the pristine CFs to 358.19 N and 373.97 N for the ASPN5 and ASPAr5-5% treated fibre bundles, respectively. The average tensile strengths for fibre bundles are 1.62 GPa (pristine), 1.73 GPa (ASPN5) and 1.81 GPa (ASPAr5-5%), increasing 6.4% and 10.8% after ASPN5 and ASPAr5-5% treatments respectively. It is clear that the tensile strength results of the fibre bundle are consistent with the results of the single fibre tensile strength.

Table 4.2-4 Tensile strength of CF bundles.

Sample code	Maximum Load (N)	Tensile strength (GPa)
Pristine CF bundle	351 ± 25	1.62 ± 0.12
ASPN5 CF bundle	358 ± 19	1.73 ± 0.09
ASPAr5-5% CF bundle	374 ± 19	1.81 ± 0.09

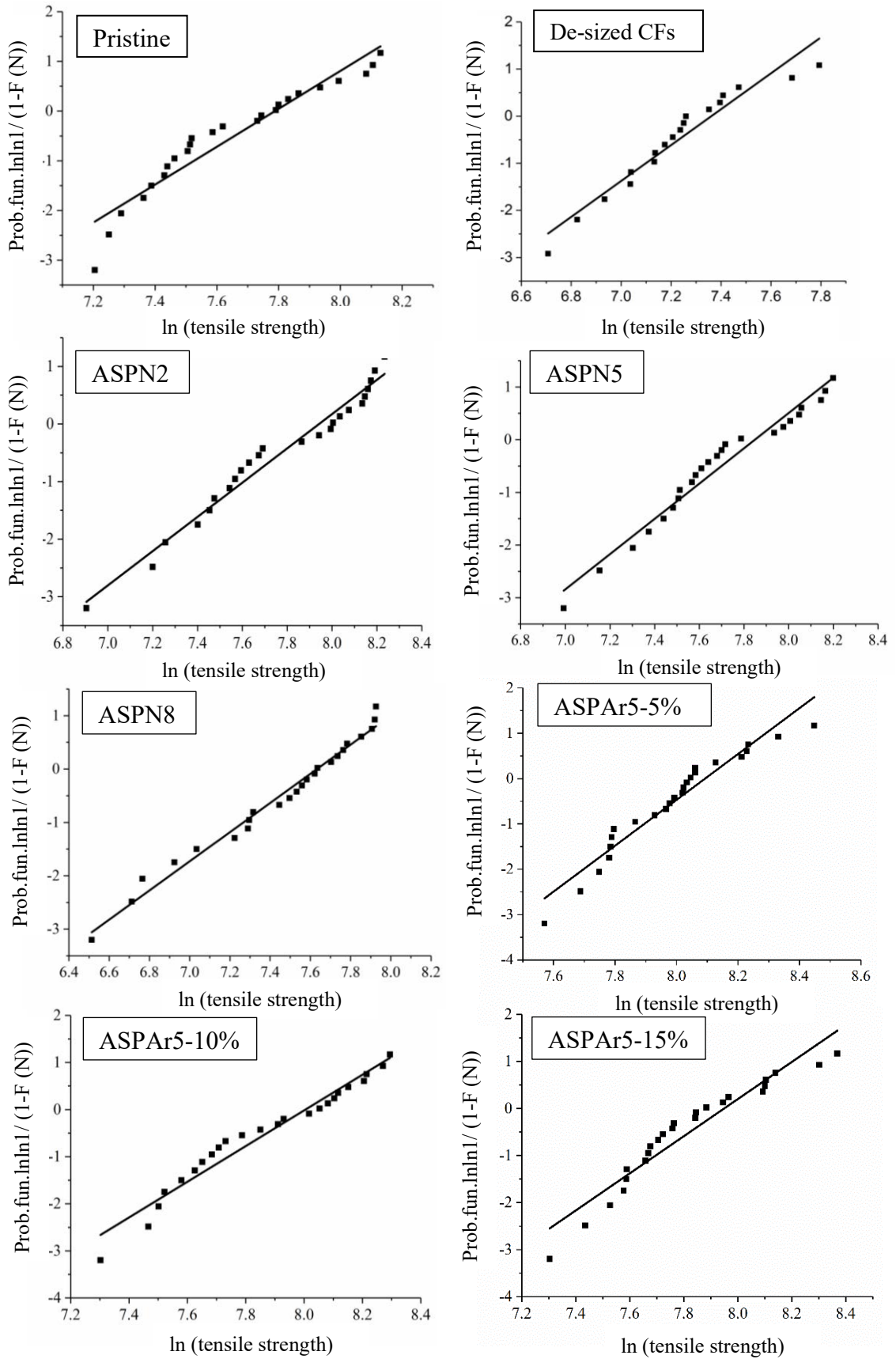


Figure 4.2-8 Weibull plots and linear fits for all groups of CFs.

4.3 Evaluation of CF/epoxy interfacial adhesion

As discussed in Chapter 2, the interfacial adhesion of CF reinforced composites can be evaluated by direct examination of interfacial shear strength (IFSS) of an individual fibre using micro-bond test, single fibre pull-out test, single fibre push-out test and single fibre fragmentation test [120]. However, except for the single fibre push-out test, all other tests are only applicable to model composites containing a single fibre. Hence it is difficult, if not impossible, to relate the measured IFSS from the model composites to the real performance of industrially manufactured composites. Therefore, nano-indentation enabled single fibre push-out testing method has further improved and used in this research to investigate and evaluate the interfacial adhesion between the single CF and the epoxy substrate. The optimisation of the push-out test and the interpretation of the experimental curves are presented in Section 4.3.1 and Section 4.3.2 respectively, which is followed by its application in evaluating the interfacial shear stress of composites made with pristine and active screen plasma treated CFs (Section 4.3.3 & Section 4.3.4). The creep behaviour of the composite is reported in Section 4.3.5.

4.3.1 Optimisation of nano-indentation enabled push-out testing

An image of the push-out tested area ($0.2 \text{ mm} \times 0.15 \text{ mm}$) is shown in Figure 4.3-1. It can be seen that the tested fibres in this area penetrated into the surrounding matrix (marked by circles and squares) and the tested resin showed clear indentation imprints (marked by triangles). By correlating the shape of the loading-unloading curves of these nano-indentation push-out tests to the corresponding SEM images taken, three types of typical curves can be identified with the positions of the indents illustrated in Figure 4.3-2.

It can be found that the curve type (a) generated from a well-aligned indenter on the centre of the fibre's cross-section, shows a clear load plateau on the load-displacement curve at about 21 mN. Curve type (b) generated from an off-centred indent on both CF and resin, that the slope of its load-displacement curve decreases after about 20 mN but no distinct load plateau is formed throughout the test. The type curve (c) was produced when the indentation was carried out on the resin, thus resulting in a large imprint because of the deformation of the resin. Thus, the slope of type (c) curve maintained until the load was reached the pre-set maximum load.

From the corresponding SEM images shown below the curves, it can be seen that both the type (a) and type (b) tests are capable of pushing the fibres into the matrix. However, comparing to the even push along the centre of the CF in the type (a) test, the off-centred push-in type (b) test tilted CF toward one side of the matrix, leading to the resin deformation as revealed by the SEM image in Figure 4.3-2 (b) and a continued increase of load as shown in the type (b) curve. Generally, no imprint of the conical indenter was traced on the top surface of the pushed-out fibres by type (a) and type (b) tests. However, when the fibre was pushed straight to the bottom of the supporter groove, an imprint in the centre of the fibre was formed due to the plastic deformation of the CF, together with the plastic deformation of the surrounding matrix, as shown in Figure 4.3-3.

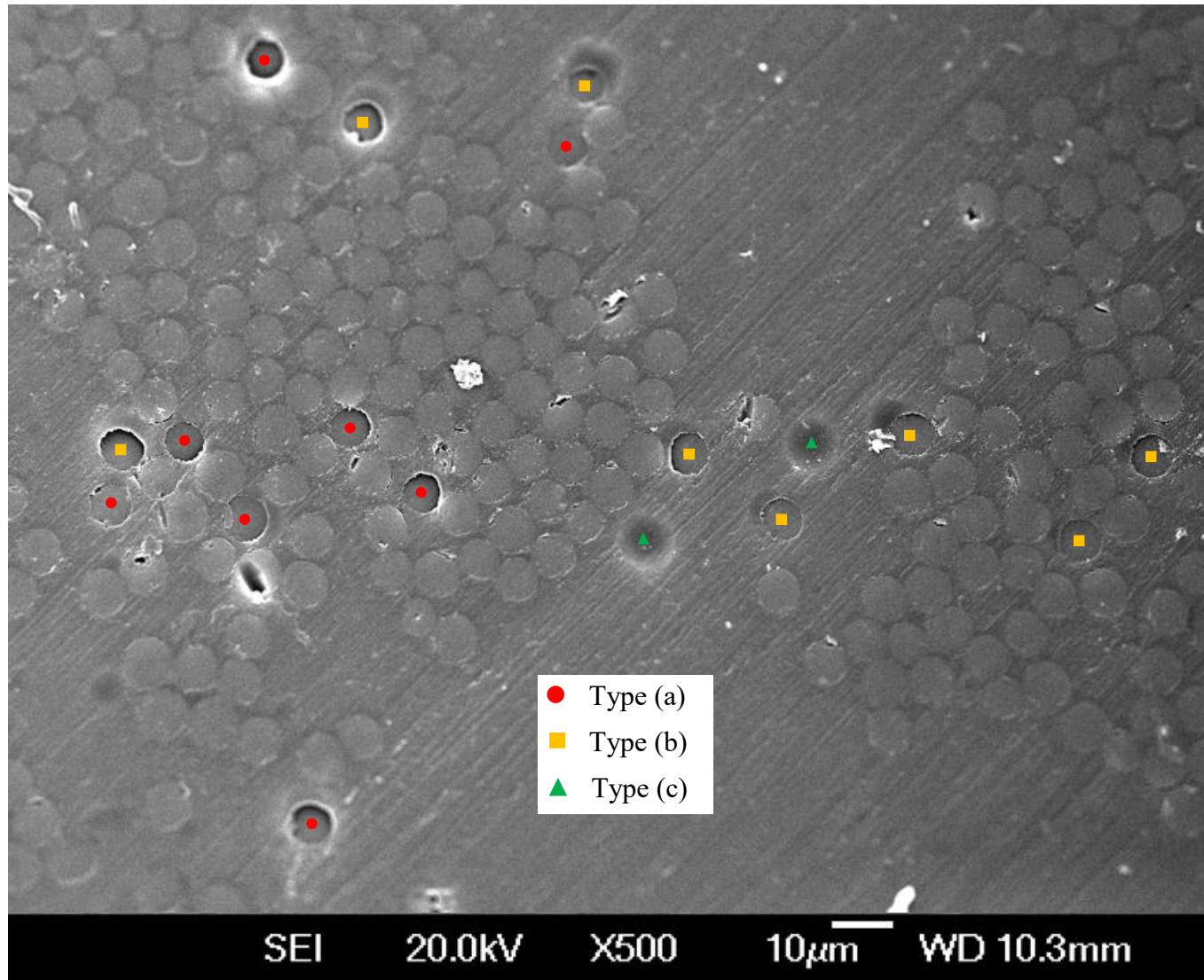


Figure 4.3-1 SEM observation of Nano-indentation tests on fibres and resin.

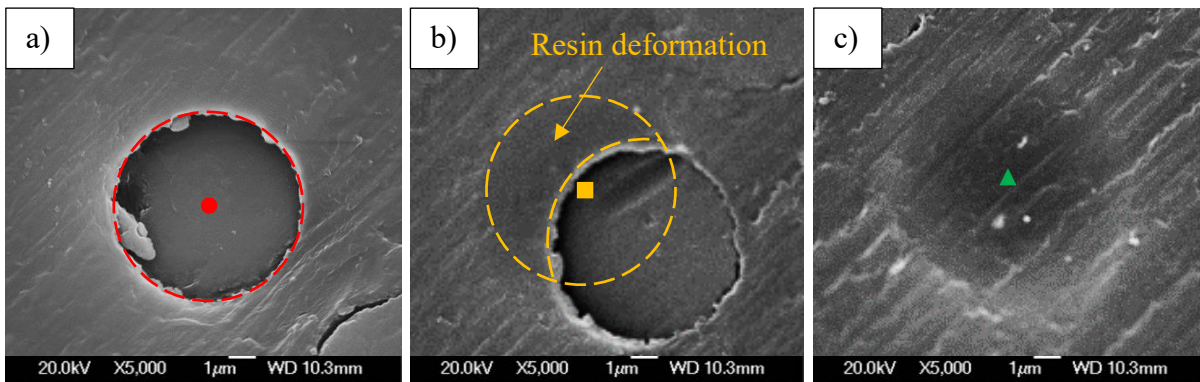
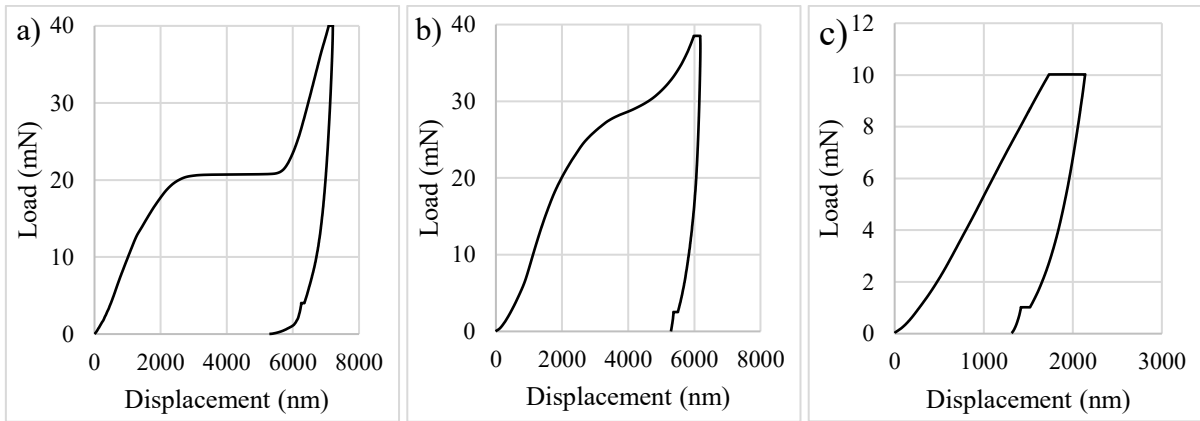


Figure 4.3-2 Typical loading-unloading curves (above) recorded from push-out tests and the corresponding SEM images of the indents positions (below).

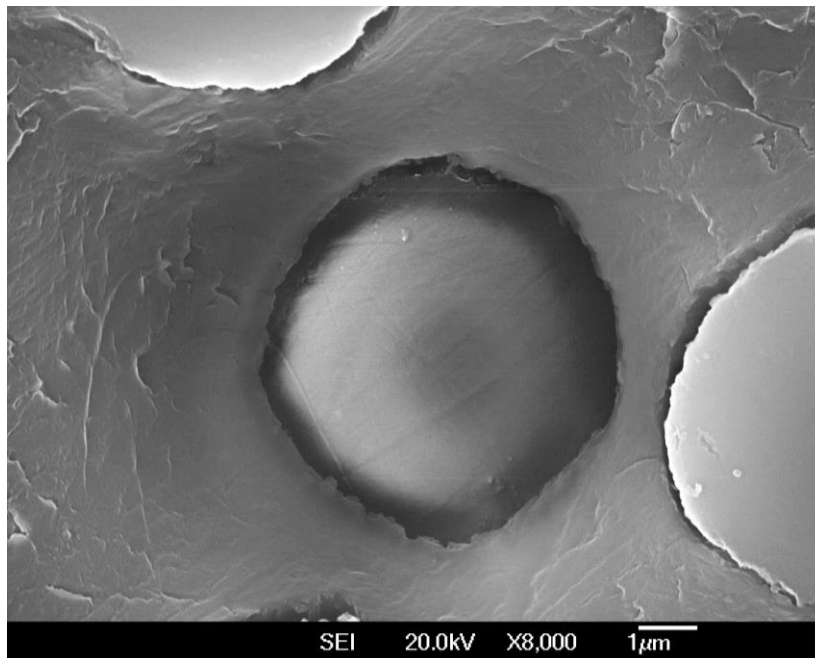


Figure 4.3-3 SEM image of pushed-out fibre with conical indenter imprint in its centre of top surfaces.

The back side of the tested CFs was observed by SEM and some typical micrographs are presented in Figure 4.3-4 (b), accompanied by the top side of the corresponding CFs (Figure 4.3-4 (a)). It can be seen clearly from both the back and the top sides that the tested CFs have been pushed out successfully. The pushed-out fibres are presented in a row in Figure 4.3-4 because of the geometry of the grooves on the sample support.

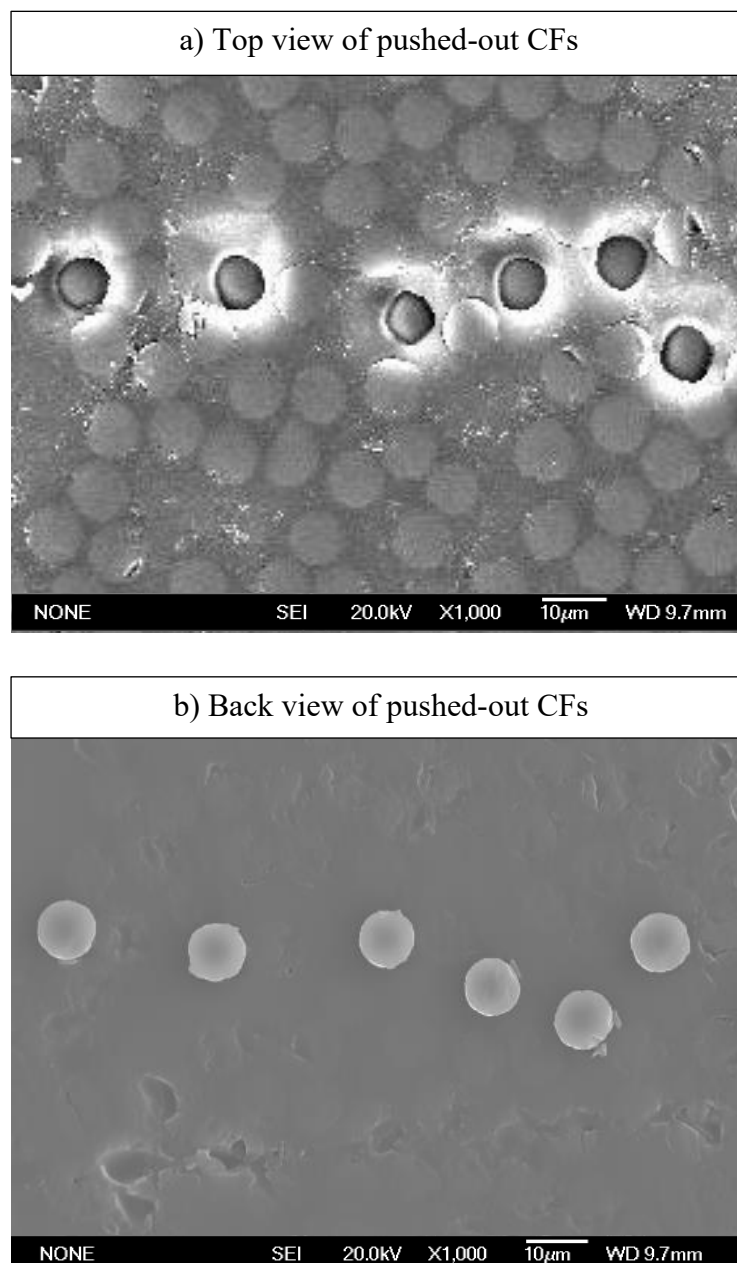


Figure 4.3-4 SEM observation of the push-out tested composite specimen from a) top view and b) back view of the pushed-out CFs.

In order to investigate the CF/resin interface, the longitudinal cross-section of a pushed-out CF (Figure 4.3-5 (a)) was cut out by Focused Ion Beam milling after *in situ* Pt deposition (Figure 4.3-5 (b)) on the top of fibre to protect the fibre from damage during ion milling. After a high ion current milling through the deposition to the fibre and a low current cleaning, the desired longitudinal cross-section of pushed-out fibre was successfully produced as shown in Figure 4.3-5 (c). From the longitudinal cross-sectional view, the longitudinal interface can be identified and the push out of the fibre is confirmed, as evidenced by a $\sim 2 \mu\text{m}$ push-out step clearly shown between the matrix and the CF on the back side. Also, plastic deformation at the adjacent matrix can be clearly seen on the top side as the dashed line shown in Figure 4.3-5 (c). Clear de-bonding and cracking can be also observed at the CF/matrix interfaces near the top surface of the CF (Sites A) and near the exit site of the matrix (Site B).

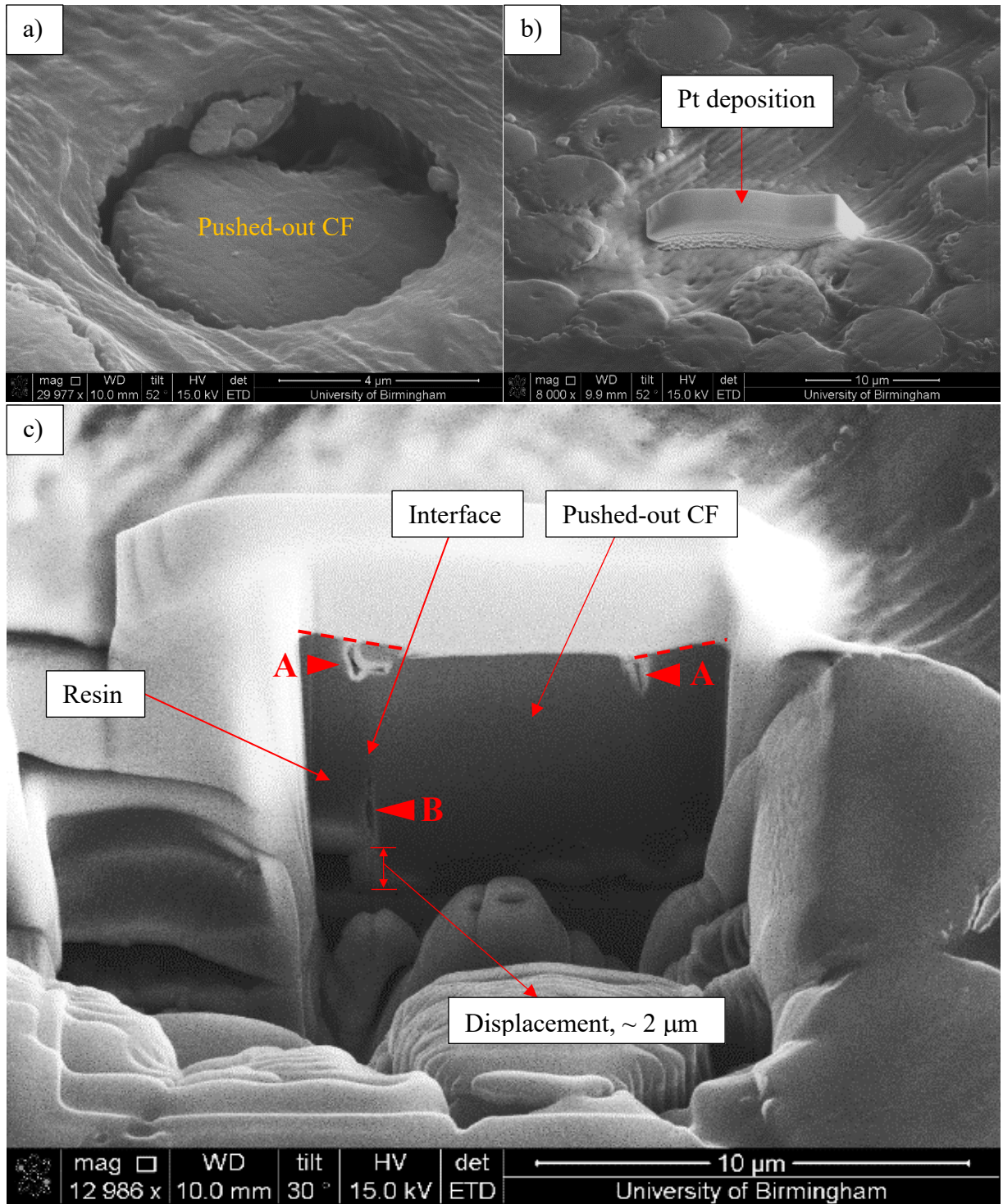


Figure 4.3-5 Sequence of cross-section preparation by Focused Ion Beam technique and the cross-sectional view of a pushed-out CF disc.

4.3.2 Interpretation of load-displacement curves

From the above analysis, it can be found that the nano-indentation push-out test requires precise positioning and alignment of the indenter with the CF sample during the experiment. A typical load-displacement curve (type (a)) combined with the schematics of the test are shown in Figure 4.3-6, illustrating various stages of the push-out test. At the beginning of the initial linear part of the load-displacement curve (Point A), the conical indenter comes into contact with the top surface of the CF. As the applied load increases (Points A to B), the indenter displacement increases to about $1.2\ \mu\text{m}$ due to the elastic deformation of the fibre/matrix system and the plastic deformation of the fibre.

The following part of the curve (Points B to C) becomes less steep, which can be attributed to the decreased elastic modulus of the fibre/matrix system. Cracks could be initiated at the top of the specimen and are about to propagate along the CF/matrix interface. This stage is described as push-in by some researchers since a shallow step between the CF and the matrix could be observed during this stage [97]. The shear stress at the CF/matrix interface increases with further increasing the applied load. When the load reaches the critical value P at point C, the elastic modulus of the CF/matrix system crashes, resulting in stress instability, and bringing a sudden increase in the displacement of the indenter tip as evidenced by a plateau (Points C to D) in the load-displacement curve. The cracks between the CF and the matrix reach the bottom side of the specimen, resulting in a completely de-bonding between the fibre and the surrounding matrix. Then, the fibre is rapidly pushed out into the groove by the critical load P . The indenter tip solely contacts with the fibre by far and the displacement of the tip is about $2.7\ \mu\text{m}$ at the end of this stage (Point D).

Further movement of the indenter tip leads to a rapid load increase as shown in the load-displacement curve (Points D to E) because the indenter tip starts to touch the adjacent matrix material. During this stage, the single fibre moves together with the adjacent matrix without the frictional sliding between them. After reaching the maximum load, unloading starts and finally the load is reduced to zero. The final displacement of the indenter tip is around 1.8 μm , which exceeds the theoretical maximum displacement (1.6 μm) of this indenter tip. This can be attributed to the plastic deformation of the fibre/matrix system and the contact stiffness between the indenter and the specimen slice.

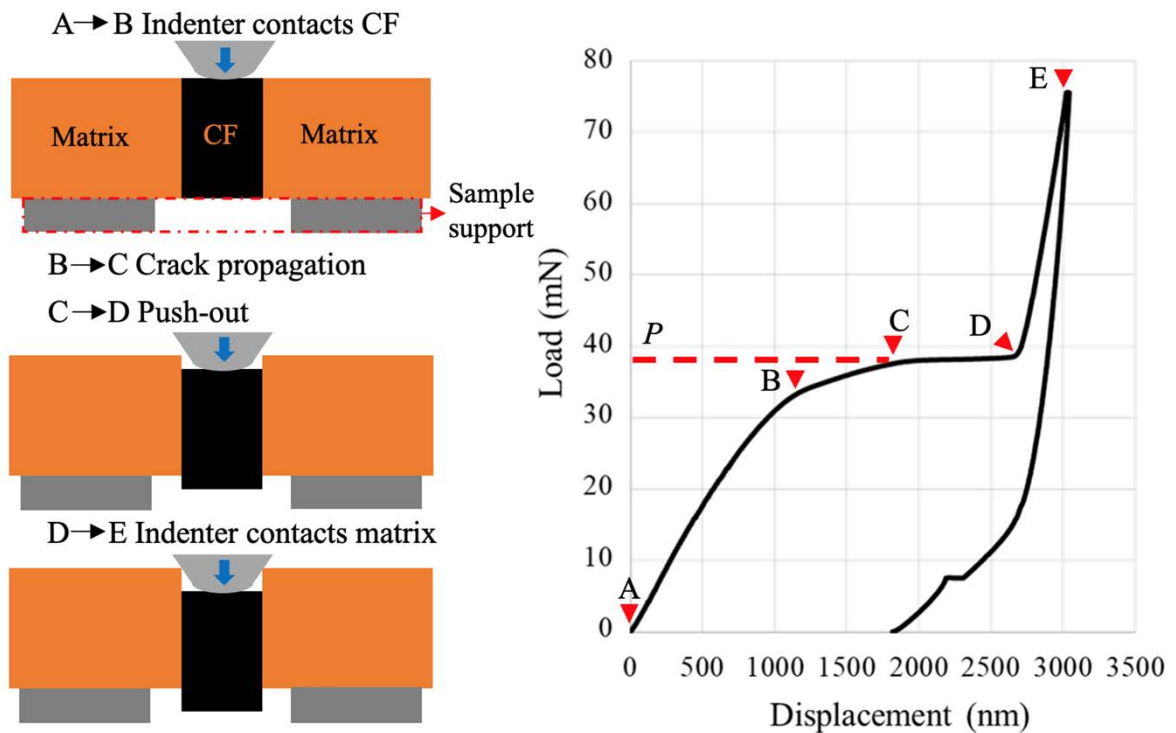


Figure 4.3-6 Schematic diagram and typical load-displacement curve of a push-out test.

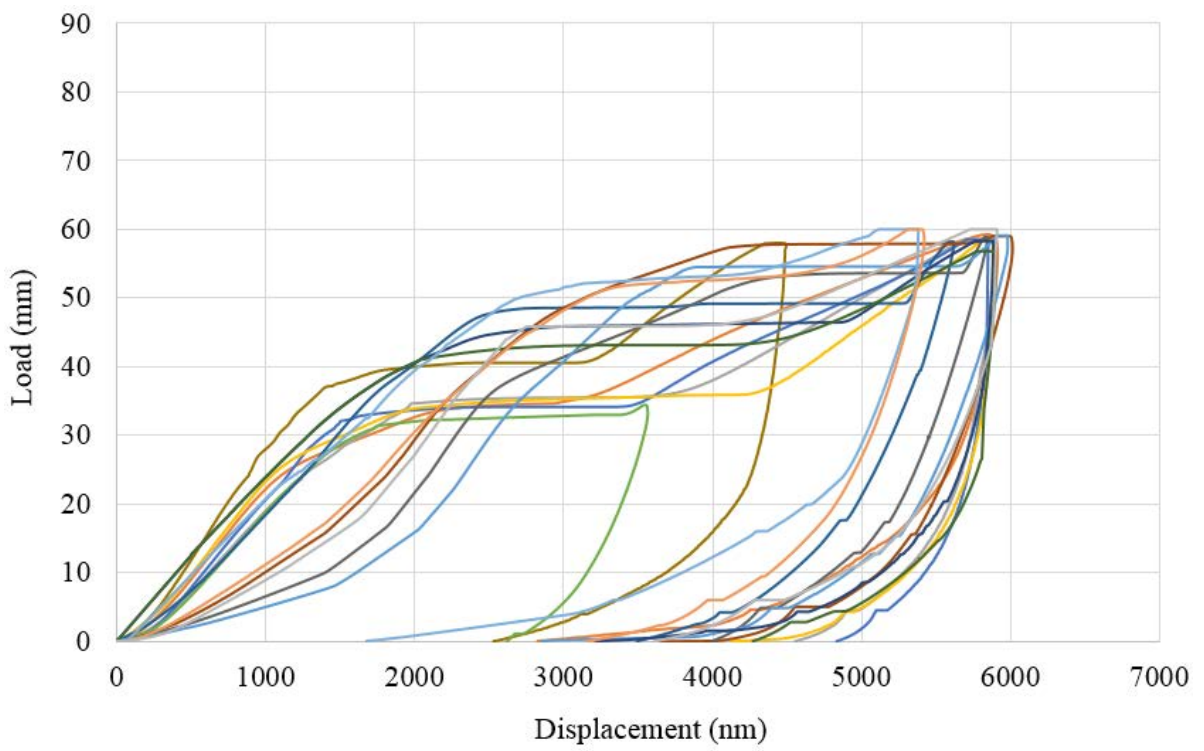
4.3.3 Load-displacement curves and post-test observations

Figure 4.3-7 shows the force-displacement curves from the push-out tests for the composites made with pristine, ASPN5 and ASPAr5-10% CFs, accompanied by detailed micrographs (Figure 4.3-8) showing typical views of the pushed-out fibres from top and bottom sides of the samples.

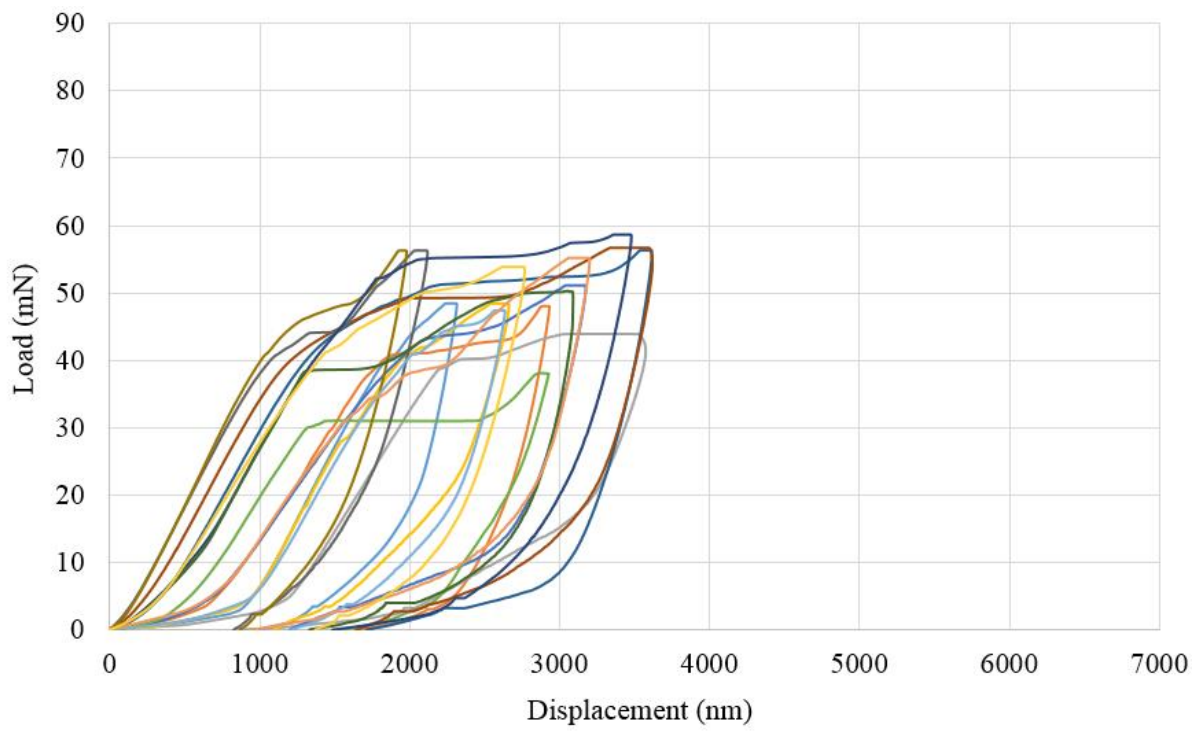
From the load-displacement curves in Figure 4.3-7, the critical load and the maximum displacement of each test can be identified. The differences in the shape of the curves are due to the actual local condition of the composite sheets on the sample supporter and the thickness of the composite samples. For instance, the bending of the composite sheet is responsible for gentle slopes of the initial part of the curves in some tests of the pristine and ASPN5 samples shown in Figures 4.3-7 (a) and (b). The local thickness of the composite sheet is the main reason for the differences in the displacement of the curves for each type of composite sample, as clearly displayed in Figure 4.3-7 (c).

Nevertheless, the critical load revealed from these tests, which dictates the interfacial shear strength, is independent of these different features of the load-displacement curves. However, it should be pointed out that the thickness difference of the composite sheets (made with pristine and ASP modified CFs) must be taken into consideration when comparing the maximum displacement or the critical load from the curves for different fibres reinforced composites, with the average sample thicknesses of 39.1 μm , 31.2 μm and 36.4 μm for the pristine, ASPN5 and ASPAr5-10% composites, respectively.

a)



b)



c)

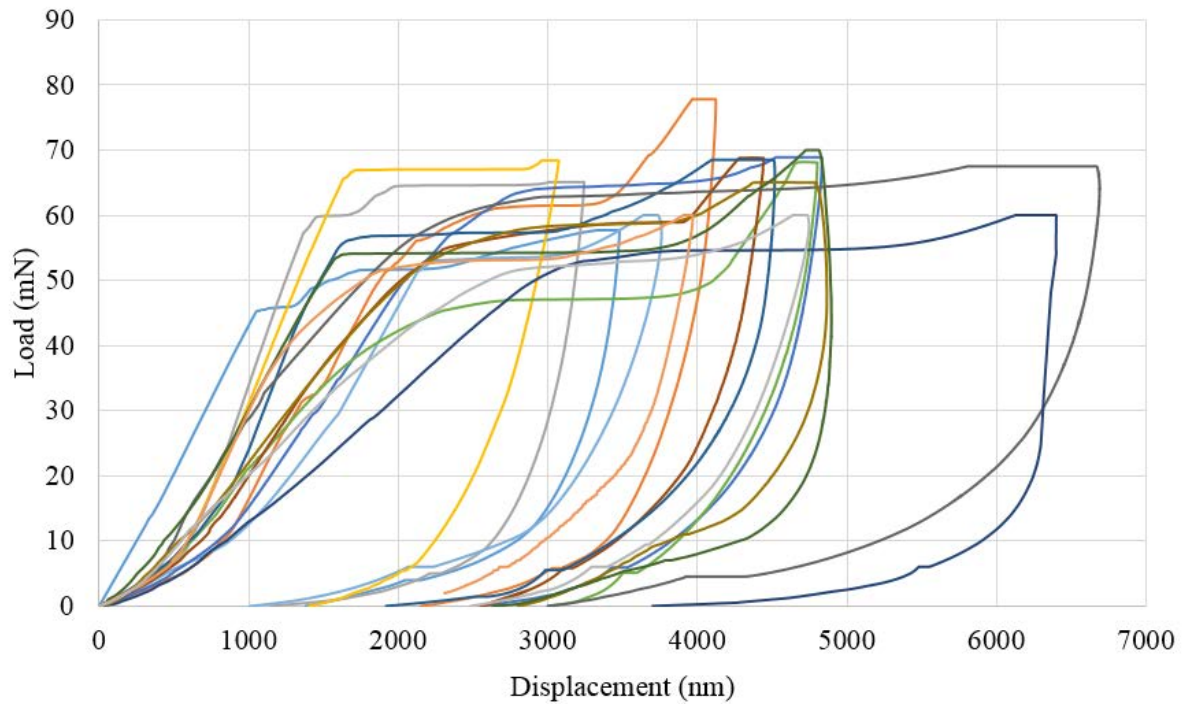
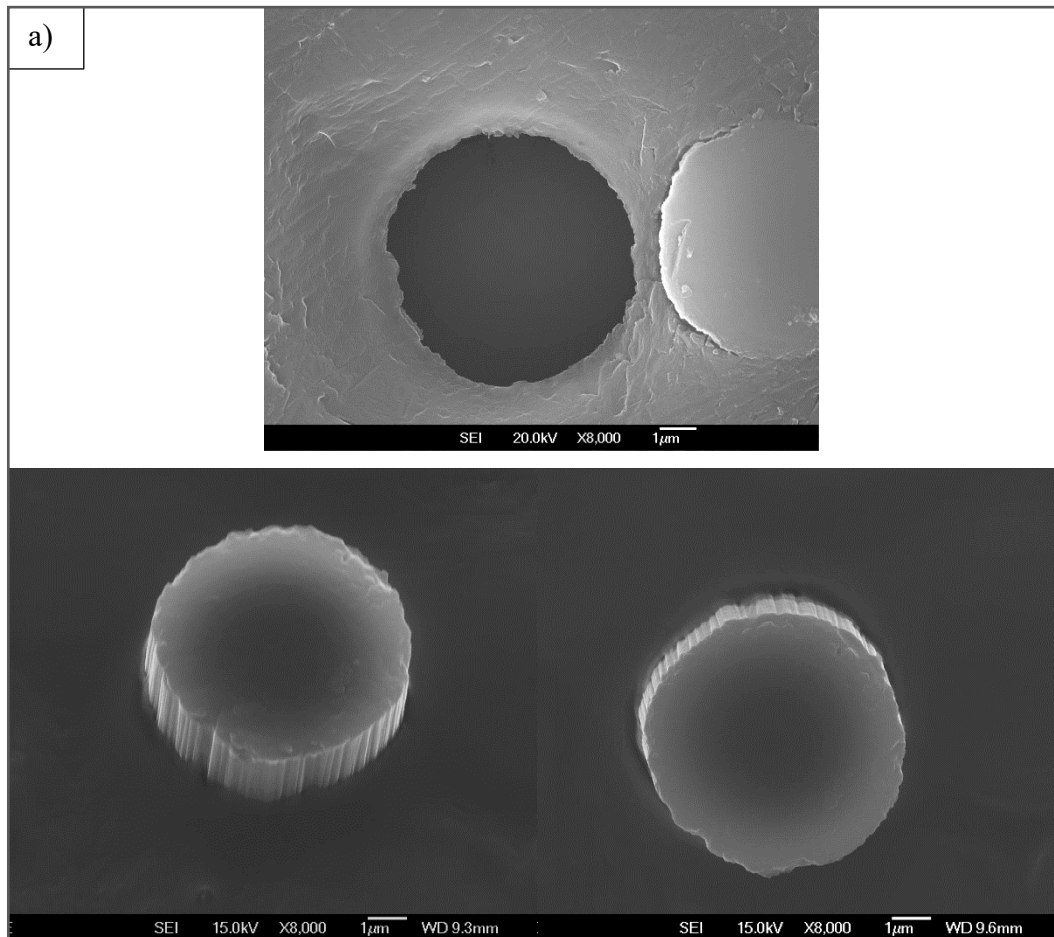


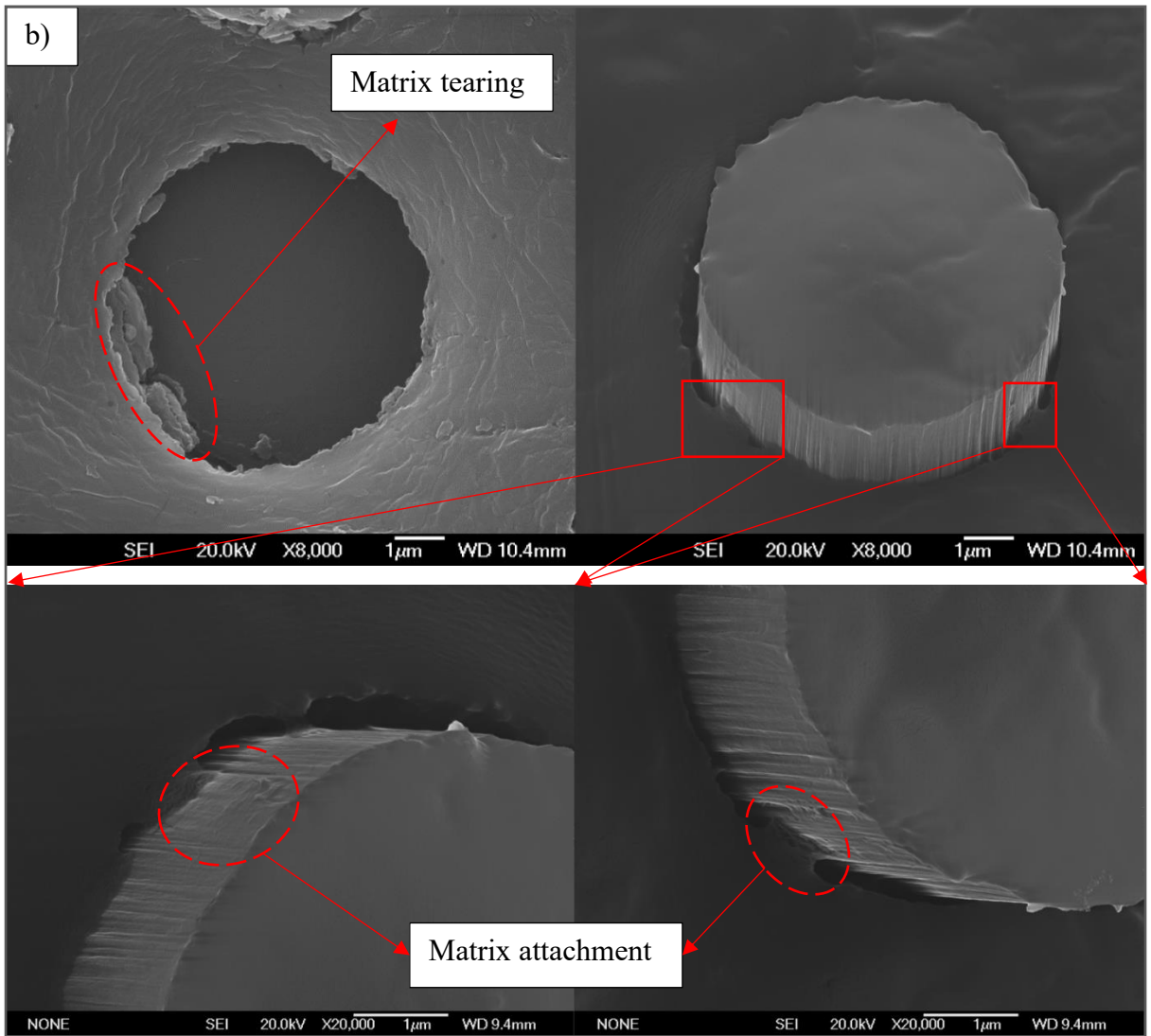
Figure 4.3-7 Experimental load-displacement curves of pushed-out CFs taken from composites made with a) pristine CFs ($h = 39.1 \mu\text{m}$), b) ASPN5 CFs ($h = 31.2 \mu\text{m}$) and c) ASPAr5-10% CFs ($h = 36.4 \mu\text{m}$).

From the morphologies of the pushed-out fibres, it can be seen that without any treatment, as shown in Figure 4.3-8 (a), the cylindrical surface of the pushed-out pristine fibre is clean with no appreciable evidence of fibre damage or attached matrix material. The adjacent matrix seems very smooth without plastic extrusion induced flanging, implying that only elastic deformation may have occurred for the matrix during the push-out test.

By contrast, Figures 4.3-8 (b) and (c) clearly show matrix material attached to the surface of pushed-out ASP treated CFs. Adjacent matrix tearing can also be observed on the top side and in some cases, the matrix was protruded together with the fibre on the back side, implying that the local failure may have occurred in the adjacent matrix rather than at the interface. These observations indicate that the ASP treated CFs have a strong interfacial adhesion with the epoxy

resin in the composites and the bonding between the ASP treated CFs and the matrix is higher than the strength of the matrix materials.





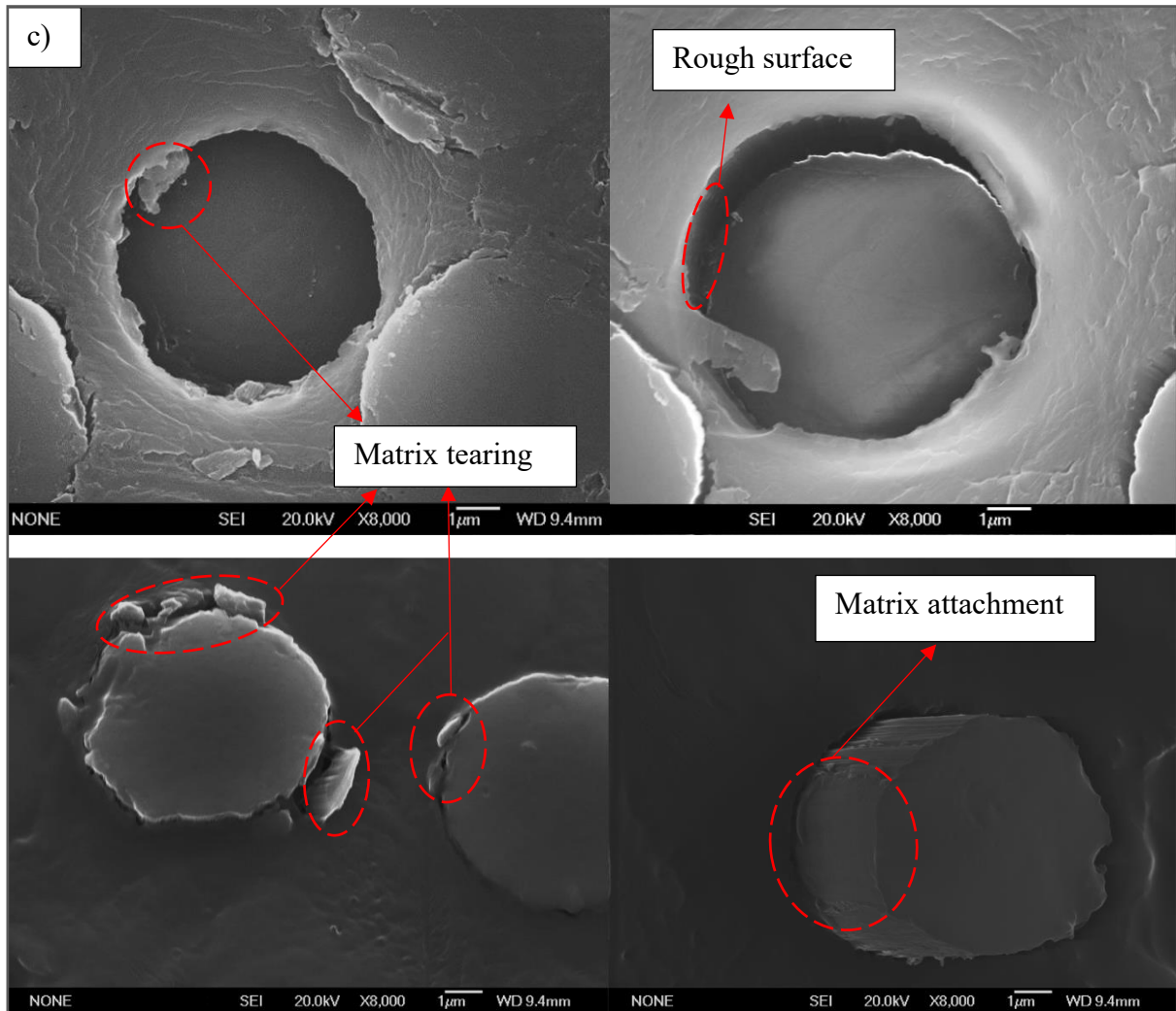


Figure 4.3-8 Post observations of pushed-out CFs taken from composites made with a) pristine CFs, b) ASPN5 CFs and c) ASPAr5-10% CFs.

4.3.4 Interfacial shear strength (IFSS)

Based on the critical loads identified from the load-displacement curves recorded during push-out tests, the average IFSS was calculated according to Equation (3-4) in Section 3.4.3.2 and the results are summarised in Table 4.3-1, together with the diameters of the pristine, ASPN5 and ASPAr5-10% treated CFs. The results show very promising improvements on the IFSS of the composites made with ASP modified CFs than the ones made with pristine CFs. The IFSS increased from 55 MPa to 72 MPa for ASPN5 and 77 MPa for ASPAr5-10% CFs reinforced

composites, indicating an improvement exceeding 30%. However, there are relatively large variations of the measured average IFSS values, which makes it difficult to conclude that significant improvement in IFSS by ASP treatment of the CFs are obtained if the experimental errors are taken into account.

For this reason, Weibull distribution has been adopted to statistically analyse the push-out test data. The Weibull plots and the fitted straight lines according to Equation (3-5) for the IFSS of composites made with three types of CFs are presented in Figure 4.3-9 and the results of the Weibull statistical analysis are summarised in Table 4.3-1. It can be seen that the Weibull plots are approximately linear, and all the fitting coefficient values R^2 are over 93%, signifying that the IFSS of all composites followed a Weibull distribution. The Weibull scaling parameters (τ) of IFSS after ASP treatments followed the same trend with the average IFSS values. In addition, the Weibull plots of IFSS for composites with ASP treated CFs are clearly separated from the pristine system, highlighting that the improvements in the IFSS values are statistically significant. Another observation related to Table 4.3-1 is that the ASPAr5-10% treatment slightly reduced the Weibull modulus, indicating that the measured data from ASPAr5-10% treatments possessed a slightly larger scattering.

Table 4.3-1 Average interfacial shear strength and Weibull parameters for pristine, ASPN5 and ASPAr5-10% CFs reinforced composites.

Sample code	d (μm)	Average IFSS (MPa)	Weibull modulus, m	Weibull scaling parameter, τ (MPa)	R^2
Pristine	6.76 ± 0.32	55 ± 12	10.22	57	93.8
ASPN5	6.62 ± 0.25	72 ± 9	10.36	75	93.1
ASPAR5-10%	6.63 ± 0.28	77 ± 10	9.80	81	97.3

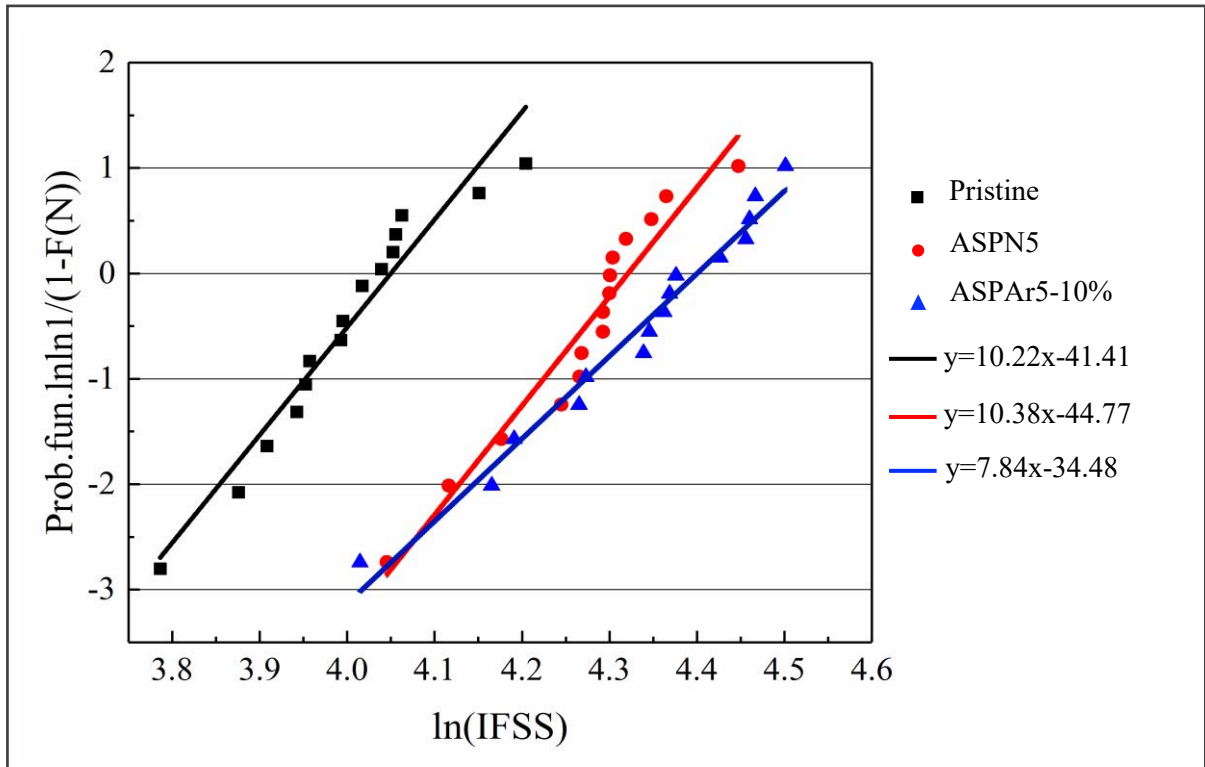


Figure 4.3-9 Weibull probability plots and linear fits for the push-out tests data taken from the composites made with pristine, ASPN5 and ASPAr5-10% treated CFs.

4.3.5 Creep behaviour of the CF/matrix system

The push-out test as described in 4.3-6 is conducted by continuously increasing the load until the de-bonding between the fibre and the surrounding resin (interface failure) occurs and a plateau on the load-displacement curve is detected. However, the interface could fail as well when a constant load, which is lower than the critical load, is applied on the fibre for a longer dwell time. Indeed, most composite components work under constant loads for a long service period. Therefore, the creep behaviour of the CF/matrix system is very important for advanced scientific understanding and industrial application.

Figure 4.3-10 (a) shows the load-displacement curves of push-out tests under different peak loads for composites with ASPAr5-10% modified CFs. It can be seen clearly that the slopes of

the loading part of the curves decreased when increasing the peak load from 6 mN to 8 mN and 10 mN. The displacement during the holding time at the peak load increased significantly as the applied peak load increased. After unloading, residual displacement (plastic deformation) can be observed from the load-displacement curves in the cases of larger peak loads (8 mN and 10 mN). Figures 4.3-10 (b), (c) and (d) depict the changes of the displacement at peak loads of 6 mN, 8 mN and 10 mN, respectively. It can be seen that the creep deformation occurred at a relatively high rate initially and then continued at a slow rate for all three tests. For the peak load of 6 mN, the displacement of fibre increased gradually until reaching the maximum deformation of about 28 nm for 90 seconds. However, when the peak load was elevated to 8 mN, two steps (about 2 and 5 nm) in the displacement occurred after holding approximately 53 and 75 seconds respectively as shown in Figure 4.3-10 (c), indicating the failure of the fibre/matrix interface. Post observation revealed that the fibre was pushed out at this load. The maximum deformation of the fibre/resin system at the peak load of 8 mN increased to 51 nm including the push-out distance of about 7 nm. For the highest peak load of 10 mN, a relatively large step (24 nm) appeared just after holding about 12 seconds and the fibre was pushed out by 15 nm. The maximum deformation of the fibre/matrix system was further increased to 105 nm.

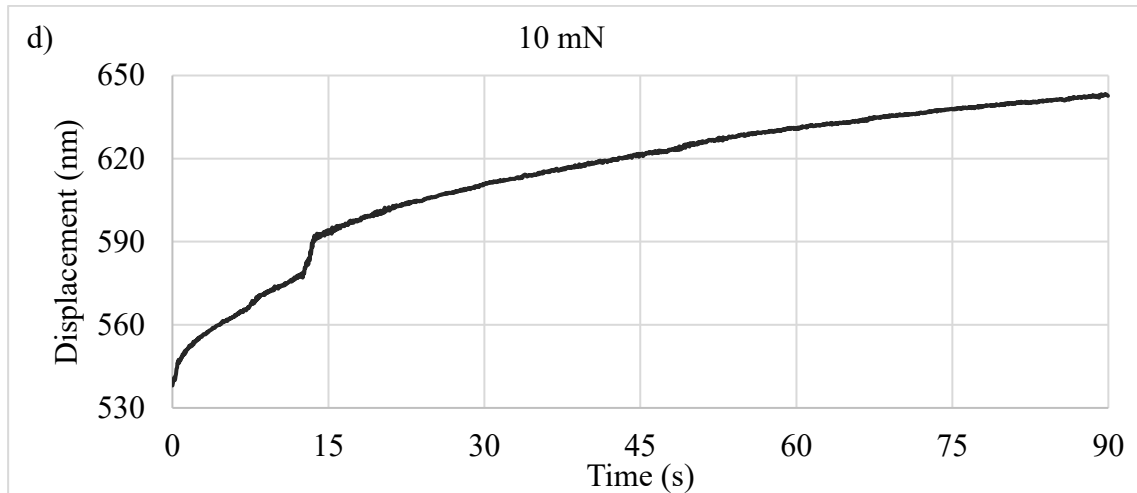
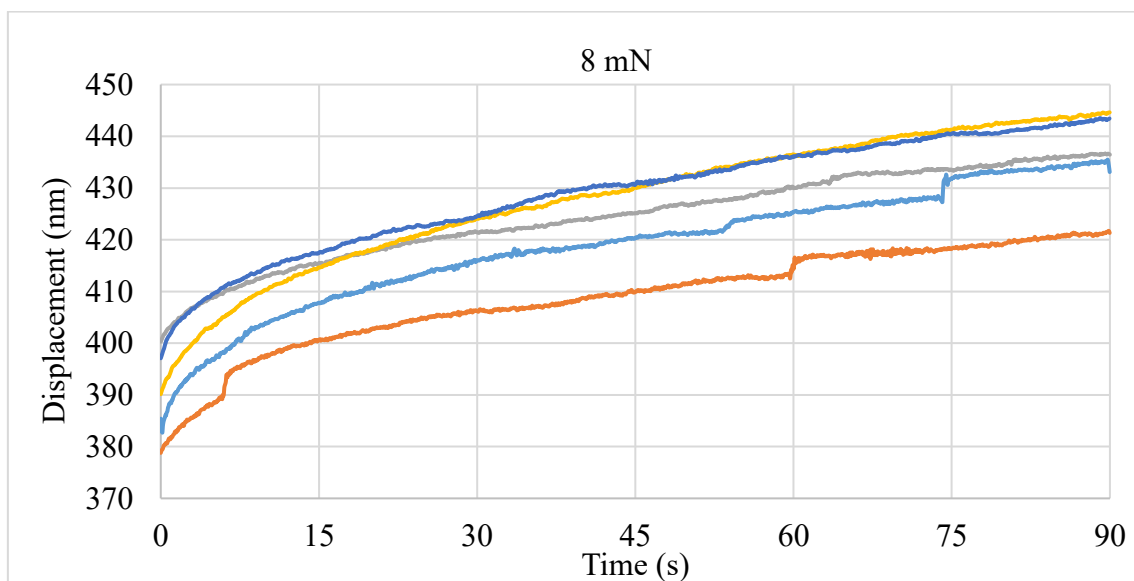


Figure 4.3-10 (a) Typical load-displacement curves for different peak loads and (b) (c) (d) the displacement of the indenter at peak load against the increment of time at dwelling period.

The push-out tests at the peak loads of 8 mN and 10 mN were repeated five times on a 9 μm thick composite sheet and their deformation curves are depicted in Figure 4.3-11. It can be seen that when loaded at 8 mN, the displacement steps, which indicate the failure of the fibre/matrix system, can be observed in two out of five tests. However, when loaded at 10 mN, the fibre/matrix system failed for all five tests and the initial failure tends to occur earlier than when tested at a lower load of 8 mN.



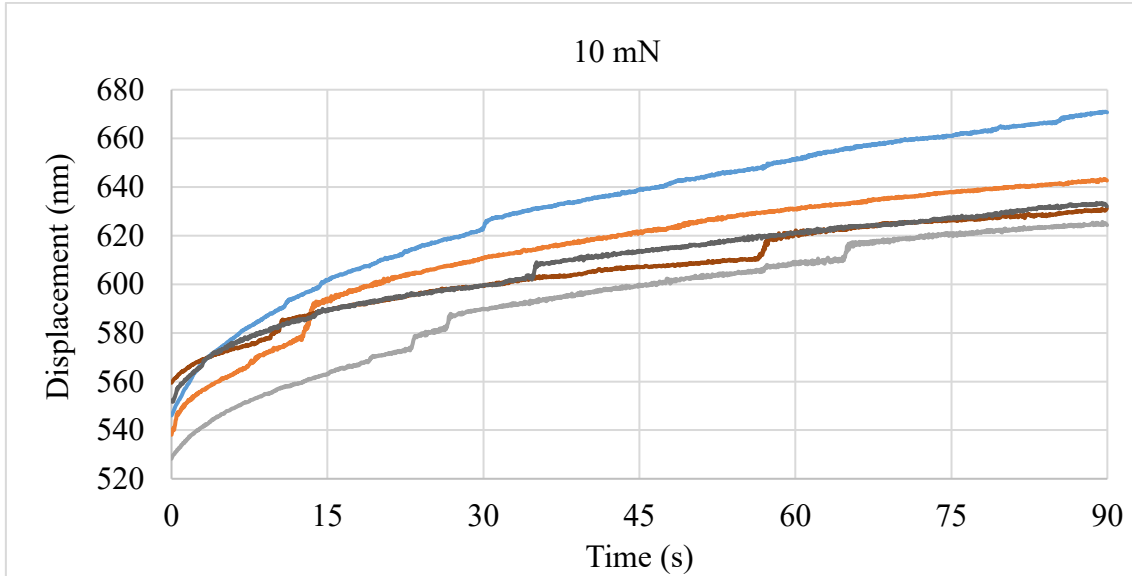


Figure 4.3-11 The displacement of the fibre/matrix system at peak loads of 8 mN and 10 mN against the increment of time at dwelling period.

The creep rates for the tests with 8 mN and 10 mN are calculated based on Equation (3-6), and the maximum creep displacements are recorded and compared in Table 4.3-2 and Figure 4.3-12. As expected, both the maximum creep displacements and the creep rates increased when the peak load was increased from 8 mN to 10 mN, despite being more scattered at the higher load (10 mN). The average maximum creep deformation and average creep rate increased from 46.51 nm and 12% to 122.06 nm and 19% when the load increased from 8 mN to 10 mN. The reason for the larger creep deformation and creep rate at the higher load of 10 mN is that all the fibres are pushed out at the peak load of 10 mN. Therefore, the critical creep load for this 9 μm thick composite made with ASPAr5-10% modified CFs is believed to be in the range of 8 mN to 10 mN. Further de-bonding tests on this thin composite carried out by continuously increasing load revealed that the critical push-out load is around 12 mN as shown in Figure 4.3-13. Clearly, the critical creep load is lower than the critical push-out load.

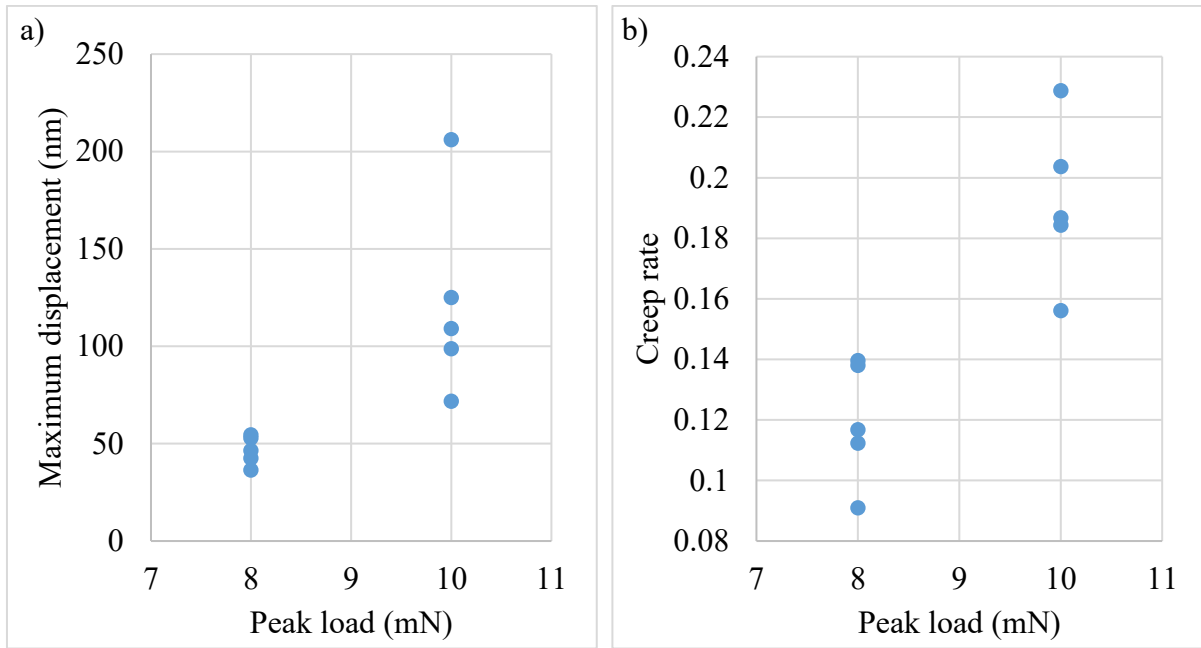


Figure 4.3-12 (a) Maximum creep deformation and (b) creep rate of the fibre/matrix system for a 9 μm thick composite sheet with peak loads of 8 mN and 10 mN.

Table 4.3-2 Creep maximum deformation and creep rate of the fibre/matrix system.

Peak load (mN)	Maximum creep deformation (nm)	Average max creep deformation (nm)	Creep rate	Average creep rate
8	52.80	46.51 ± 7.43	0.14	0.12 ± 0.02
	42.52		0.11	
	36.41		0.09	
	54.45		0.14	
	46.35		0.12	
10	124.91	122.06 ± 50.74	0.23	0.19 ± 0.03
	109.09		0.20	
	98.63		0.19	
	205.95		0.18	
	71.72		0.16	

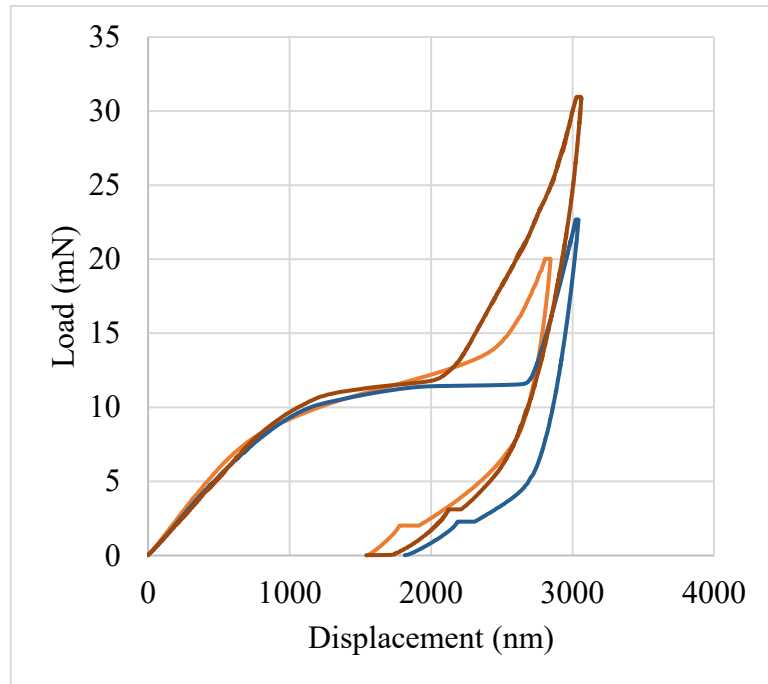


Figure 4.3-13 Load-displacement curves for push-out tests of 9 μm composites with ASPAr5-10% modified CFs.

4.4 Mechanical properties of carbon fibre reinforced composites

The mechanical properties of CFs reinforced composite (CFRC) are of great importance for their applications in different areas. Thus, this section reports the response of composites, reinforced by pristine and ASP modified CFs, to different mechanical tests. Section 4.4.1 and Section 4.4.2 present the results of mechanical tests on woven fabric reinforced laminate composites and unidirectional CFs reinforced composites respectively.

4.4.1 Mechanical properties of woven fabric reinforced laminate composites

4.4.1.1 Surface morphology

The surface morphologies of the pristine and the ASP treated CF fabrics were observed by optical microscope and SEM, respectively. As shown in Figure 4.4-1, the ASP treatments induced changes in the colour of the fabric surfaces, which could be attributed to the oxidation of the treated fabric surfaces when exposed to air after these treatments. From the SEM images, it can be seen that almost identical surfaces with longitudinal grooves are observed in all cases except a few contaminations on the pristine fabrics. Neither surface defects nor arcing damage can be observed on the treated fabric surfaces. This indicates that due to the remote-plasma nature ASP can effectively avoid surface damages caused by DC and other plasma technologies.

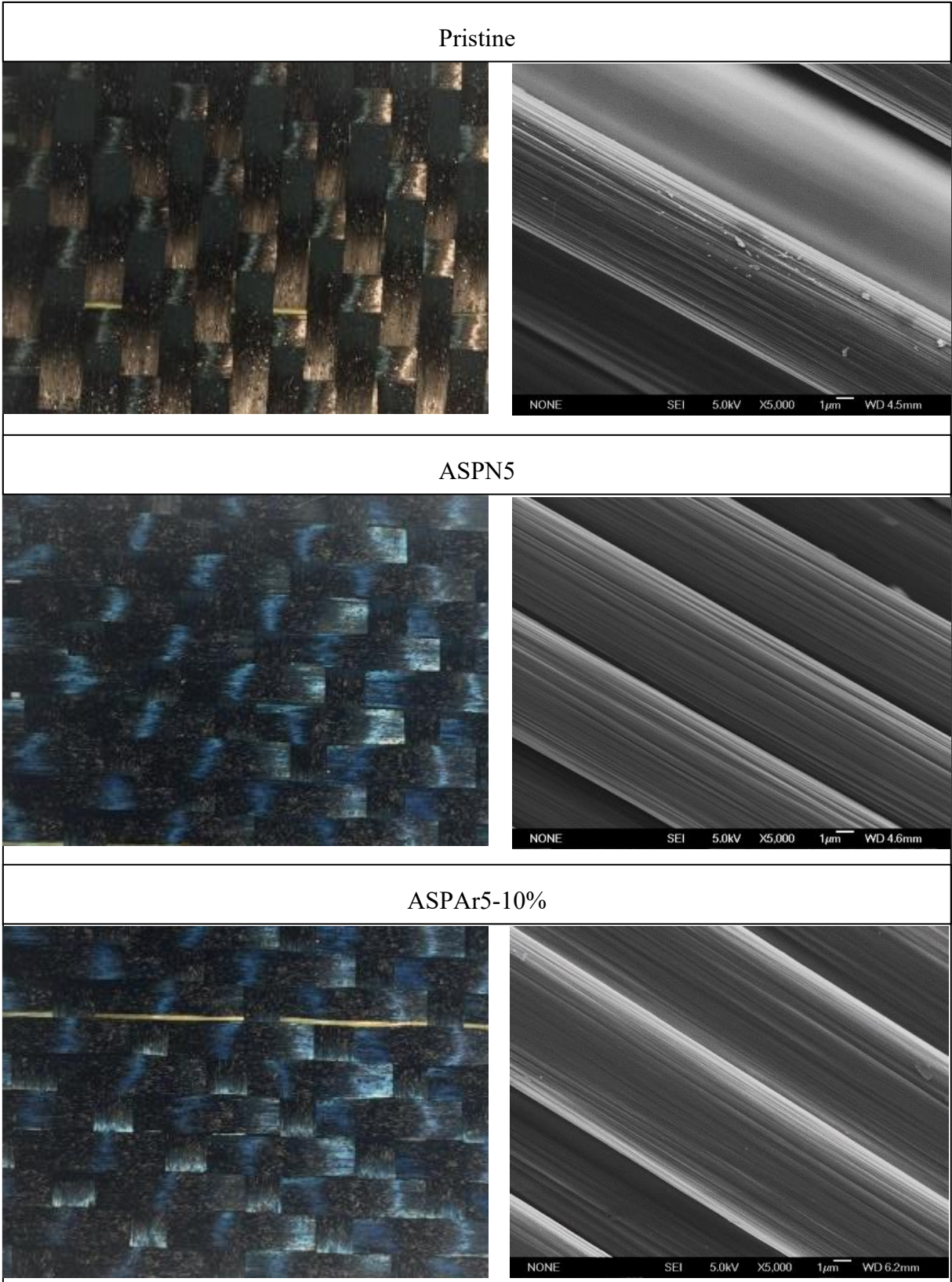


Figure 4.4-1 Images of the pristine and the ASP treated carbon fabrics.

4.4.1.2 Flexural strength and interlaminar shear strength (ILSS)

The flexural strength and the ILSS results for the woven fabric reinforced laminate composites are demonstrated in Figure 4.4-2. It shows that both the average flexural strength and ILSS increased after ASPN5 and ASPAr5-10% treatments. The flexural strength increased from 754.6 MPa for the pristine laminate samples to 769.0 MPa for the ASPN treated ASPN5 sample and 783.4 MPa for the ASPAr treated ASPNAr5-10% sample. The pristine laminate specimens revealed an ILSS of 43.7 MPa, whereas the ASPN and ASPAr treated specimens revealed an ILSS of 46.4 MPa and 43.9 MPa, respectively. However, it is noted that the scattering of experimental data is quite large and the differences in the flexural strength and ILSS are not statistically significant although the trend could be deduced from the average values.

The interlaminar shear fracture morphology along the cross-section of composites (Figure 4.4-3) revealed that the ASP treatment could improve the interfacial adhesion between the fibres and the epoxy resin. As shown in Figure 4.4-3, the pristine CFs were pulled out of the laminate composites with limited amount of resin material adhered to the pristine CF surfaces, suggesting that the pristine CFs/ epoxy composites would have poor interfacial bonding. Whilst for the samples reinforced by modified CFs, it can be seen that the fibres and the matrix are still bonded to each other. The fracture surface seems relatively flat and the CFs are engulfed by the matrix. These results imply that the interfacial bonding between the CFs and the epoxy resin has been improved after the ASP treatments.

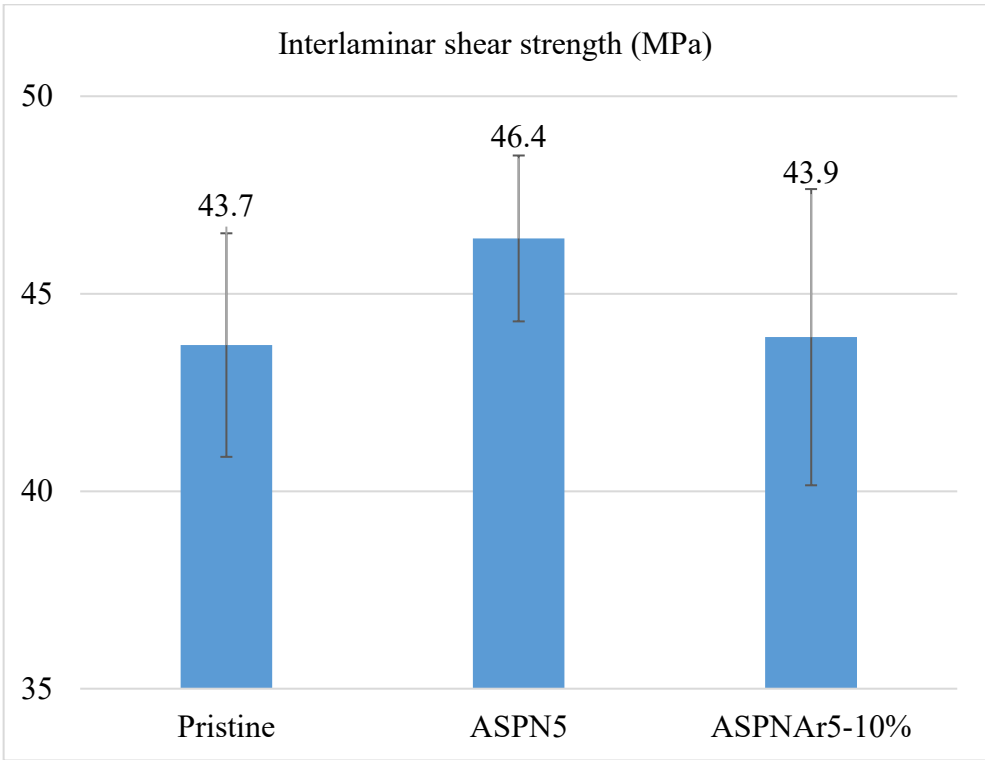
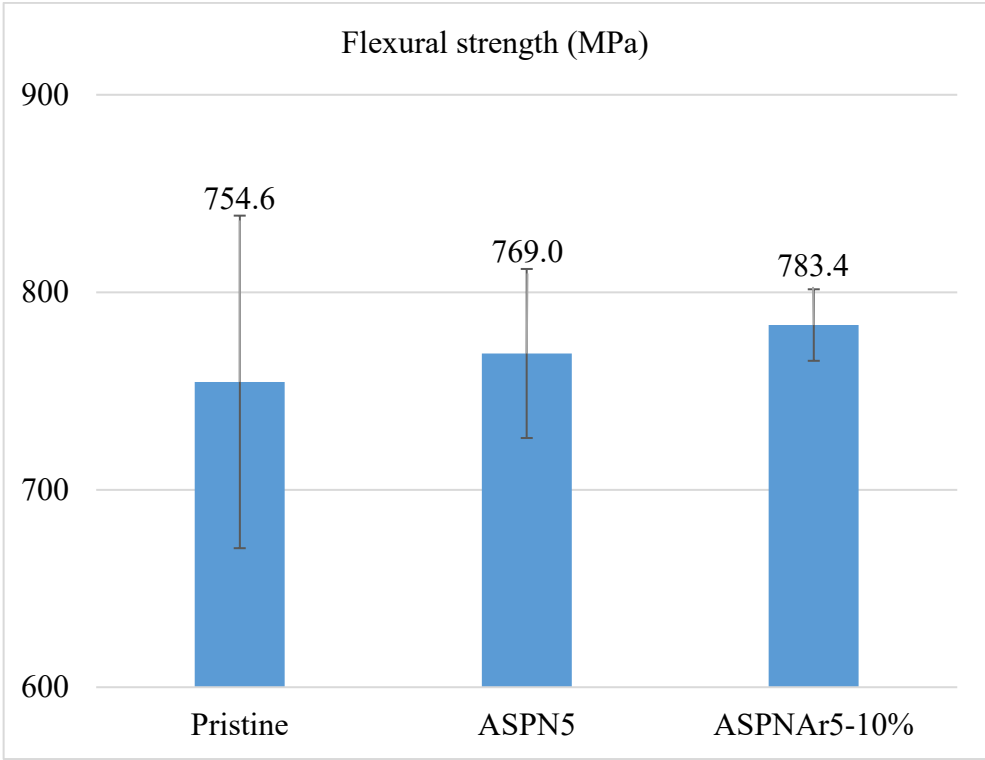


Figure 4.4-2 Flexural strength and ILSS of the woven fabric/epoxy resin composites with pristine, ASPN5 and ASPAr5-10% modified carbon fabrics.

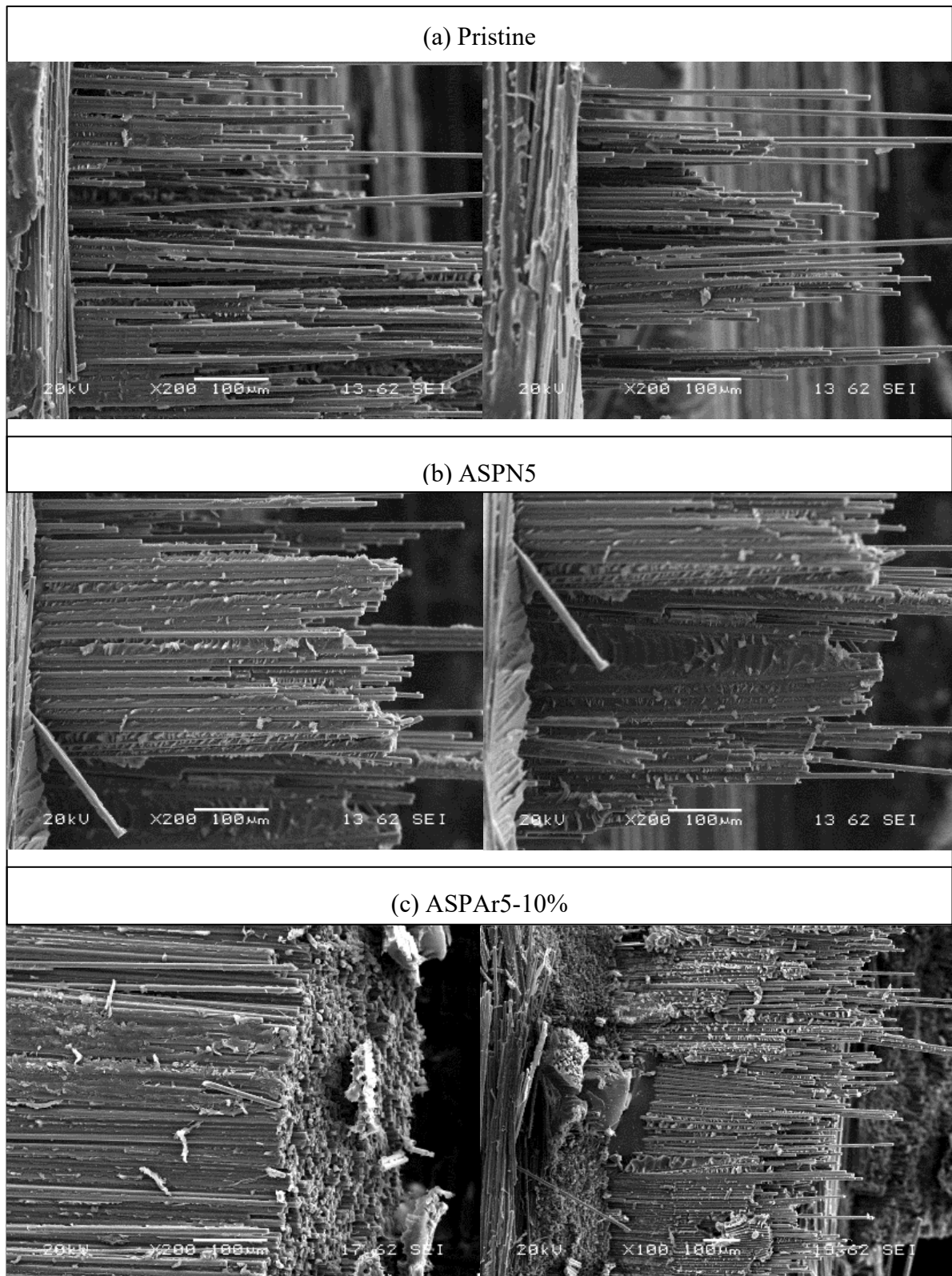


Figure 4.4-3 SEM side-view images of fracture surfaces of composites with pristine and ASP modified carbon fabrics.

4.4.1.3 Mode I interlaminar fracture toughness

Interlaminar fracture involves matrix cracking, fibre breakage, fibre pull-out, fibre slipping and fibre/matrix de-bonding, which is the primary challenge for the laminated fibre composites [170]. Thus, the interlaminar fracture property of laminate composites with pristine and ASPN5 modified fabrics has been measured using Mode I interlaminar fracture test. Some typical load-opening displacement curves are displayed in Figure 4.4-4. It can be seen that following the initial linear parts, continuous load-drops are shown on both curves, indicating that both laminate samples experienced stick-slip crack growth because of the existence of longitudinal and transversal oriented fibre bundles of woven fabrics. The crack initiation points (VIS), which are marked on the load-opening displacement curves, represent the delamination length and load at the onset of the visually recognisable crack. As shown in Figure 4.4-4, the delamination load at VIS point for ASPN5 modified sample (38 N) is slightly larger than that for pristine laminate sample (36 N), indicating that the laminate composite sample with ASPN5 modified fabrics is more effective at the interface than the sample with pristine carbon fabrics in the manner of energy absorption properties for the composites.

The average initial fracture toughness and average steady-state toughness (along with the corresponding standard deviation) for the pristine and ASPN5 carbon fabric reinforced laminates are summarised in Figure 4.4-5. Comparing to the pristine laminate samples, whose average initiation G_{IC} value and the average steady-state G_{IC} are 496 and 614 J/m² respectively, the ASPN5 modification can increase both the initiation fracture toughness and the steady-state toughness by 29% and 10% to 642 and 675 J/m², respectively.

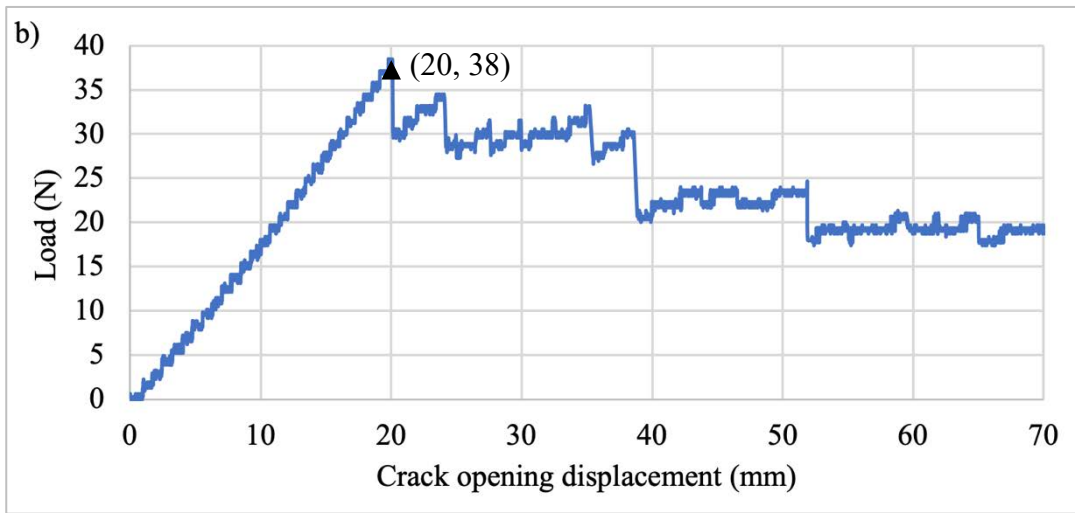
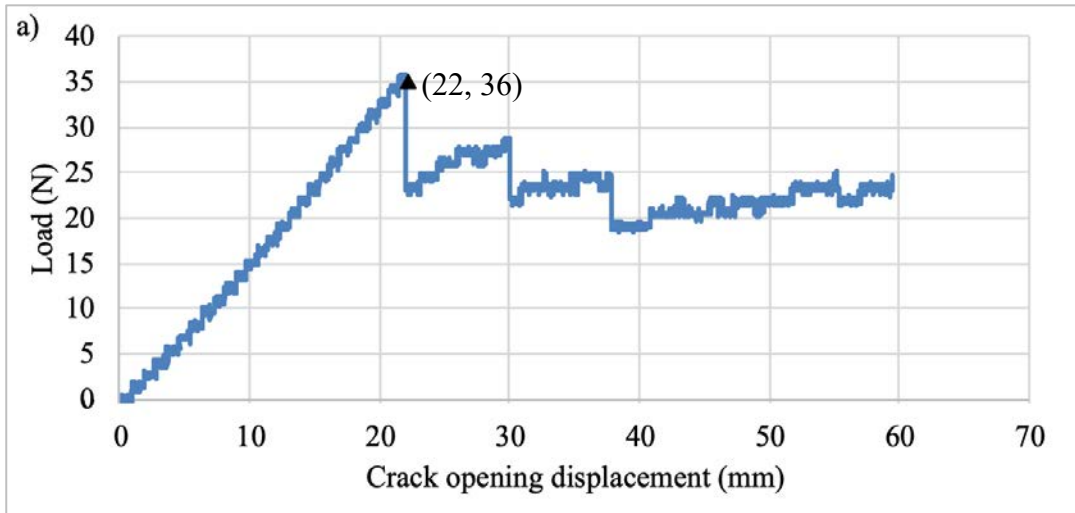


Figure 4.4-4 Load-crack opening displacement curves for the produced composite laminate with (a) pristine carbon fabrics and with (b) ASPN5 carbon fabrics.

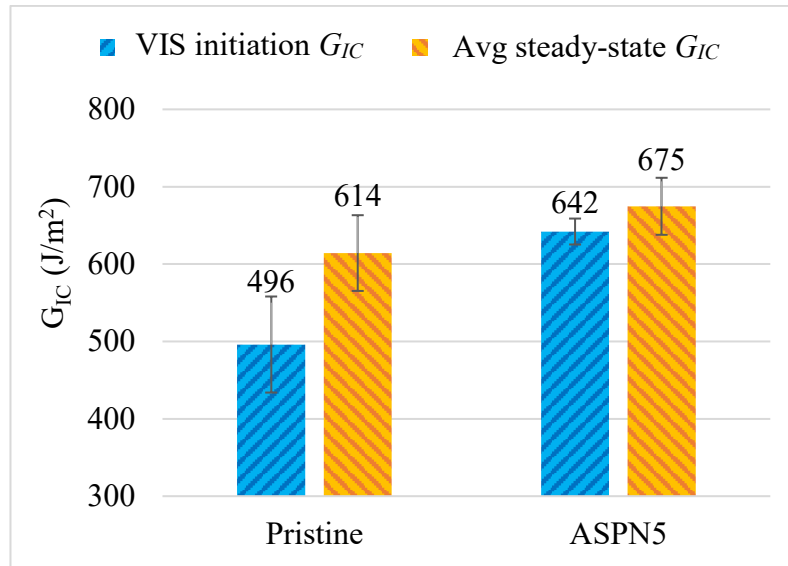


Figure 4.4-5 The average initial fracture toughness and the average steady-state toughness for pristine and ASPN5 carbon fabric reinforced composites.

The results of post SEM observations on the pristine and ASPN5 carbon fabric reinforced laminates are shown in Figure 4.4-6. It can be seen that a nearly straight breaking trace line can be observed for the laminate specimen with pristine carbon fabrics as shown in Figure 4.4-6 (a). In contrast, a zigzag breaking trace line was shown for the ASPN5 laminate specimen, indicating that the cracks were created in different layers as depicted in the detailed images in Figure 4.4-6 (b). The fracture surfaces for these two types of specimens are compared in Figures 4.4-6 (c) and (d). It can be seen that some of the fibres on the fracture surface of the pristine laminate sample were pulled out from the matrix and the fractured pristine fibre surfaces are clean and smooth, which indicates adhesion failure at the interface due to weak interfacial strength. On the contrary, for the laminate sample with ASPN5 modified fabrics, the fractured fibres are stuck together with partially covered epoxy patches.

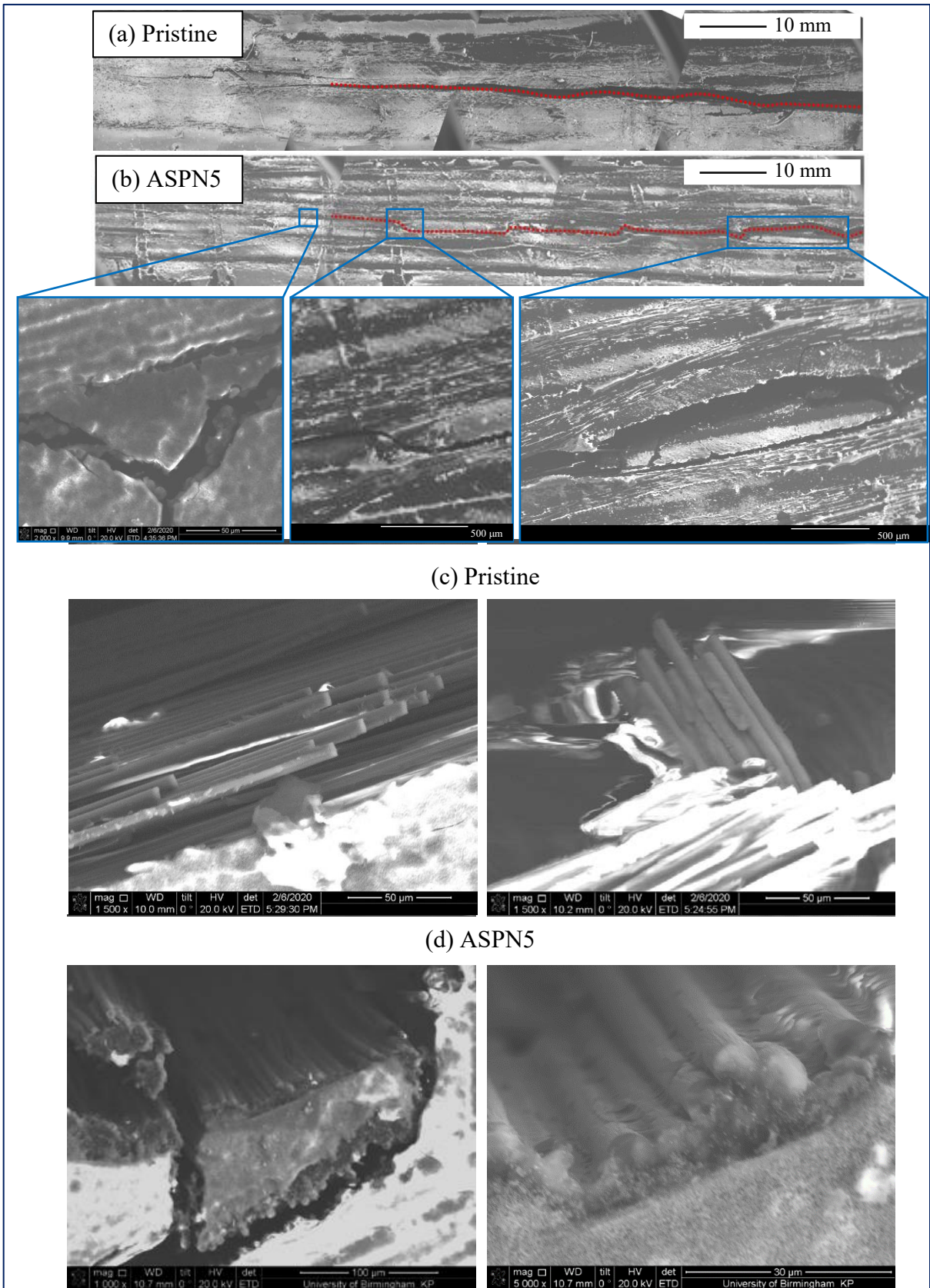


Figure 4.4-6 SEM images of fracture morphologies for composite laminates with pristine and ASPN5 carbon fabrics after Mode I interlaminar fracture tests.

4.4.2 Mechanical properties of unidirectional carbon fibre reinforced composites

4.4.2.1 Tensile, shear and flexural strengths

The tensile, shear and flexural strengths of the unidirectional CF-reinforced composite specimens made with pristine and treated CFs under ASPN5 treatment condition are summarised in Table 4.4-1. The tensile strength results tested from the composite specimens show the ultimate tensile strength of pristine and ASPN5 treated CFs possess comparable values, 3420 and 3398 MPa, respectively.

The interfacial adhesion strength of the composites is reflected in the shear and flexural tests results. It can be seen that the ASP treatment has shown a moderate effect on the shear strength under the current test conditions, in the order of a 3% increase. However, the flexural strength along fibre axis of ASPN5 treated CF reinforced composites are enhanced from 872 MPa for samples with pristine CFs to 1015 MPa, representing a 16% increase of the flexural strength.

Table 4.4-1 Tensile, shear and flexural strengths of composites reinforced with unidirectional pristine and ASPN5 treated CFs.

Sample code	Tensile strength (MPa)	Shear strength (MPa)	Flexural strength (along fibres) (MPa)	Flexural strength (cross fibres) (MPa)
Pristine	3420 ± 95	66 ± 3	872 ± 9	65 ± 10
ASPN5	3398 ± 121	68 ± 7	1015 ± 14	76 ± 11

4.4.2.2 Internal pressure destruction

As ASPN5 treated CFs revealed higher strength than the pristine CFs both in fibres and in composite samples than that of the pristine ones, 9000-m-long ASPN5 treated CFs have been validated by making airspace components of propellant tanks. The images of propellant tanks manufactured with pristine and ASPN5 modified CFs are shown in Figure 4.4-7. It can be seen that compared to the tight structures shown on the tank with pristine CFs (Figure 4.4-7 (a)), gaps were clearly shown between the adjacent yarns in the image of the tank manufactured with ASPN5 CFs (Figure 4.4-7 (c)). The thermographic and ultrasound non-destructive tests also revealed several defects on the tank made with ASPN5 CFs about 15×15 mm, 20 × 20 mm, 20 × 25 mm, 25 × 25mm, 20 × 30 mm and 40 × 10 mm. These defects are most probably resulted from the deformation of the ASPN5 fibre yarns caused by the fibre loading/unloading process during the winding process after the ASP treatments, as evidenced by the difference of the pristine and the ASPN5 bobbins shown in Figures 4.4-7 (b) and (d).

Internal pressure destructive tests were conducted to assess the performance of composites with ASP treated CFs on an industrial scale. From the results listed in Table 4.4-2, the calculated destructive pressure increased from 6.8 MPa for the fuel tank made with the pristine CFs to 8.0 MPa for the tank made with ASPN5 modified CFs. In addition, the tank made with the modified CFs showed 12%, 33% and 18% improvement in the average strain than the ones made with the pristine CFs on the central part in the transversal and longitudinal directions and on the end part in the transversal direction, respectively. It is expected that the propellant tank made with ASPN5 modified CFs could outperform the one with pristine CFs in the internal pressure destructive test.

Table 4.4-2 Calculated destructive pressure and average strain values in different sections of the tank manufactured with pristine and ASPN5 treated CFs.

Tank code	Calculated destructive pressure (MPa)	Average strain in different sections		
		Central part in the transversal direction	Central part in the longitudinal direction	End part in the transversal direction
Tank pristine	6.8 ± 0.3	0.017 ± 0.004	0.003 ± 0.001	0.022 ± 0.005
Tank ASPN5	8.0 ± 0.5	0.015 ± 0.003	0.002 ± 0.001	0.018 ± 0.003

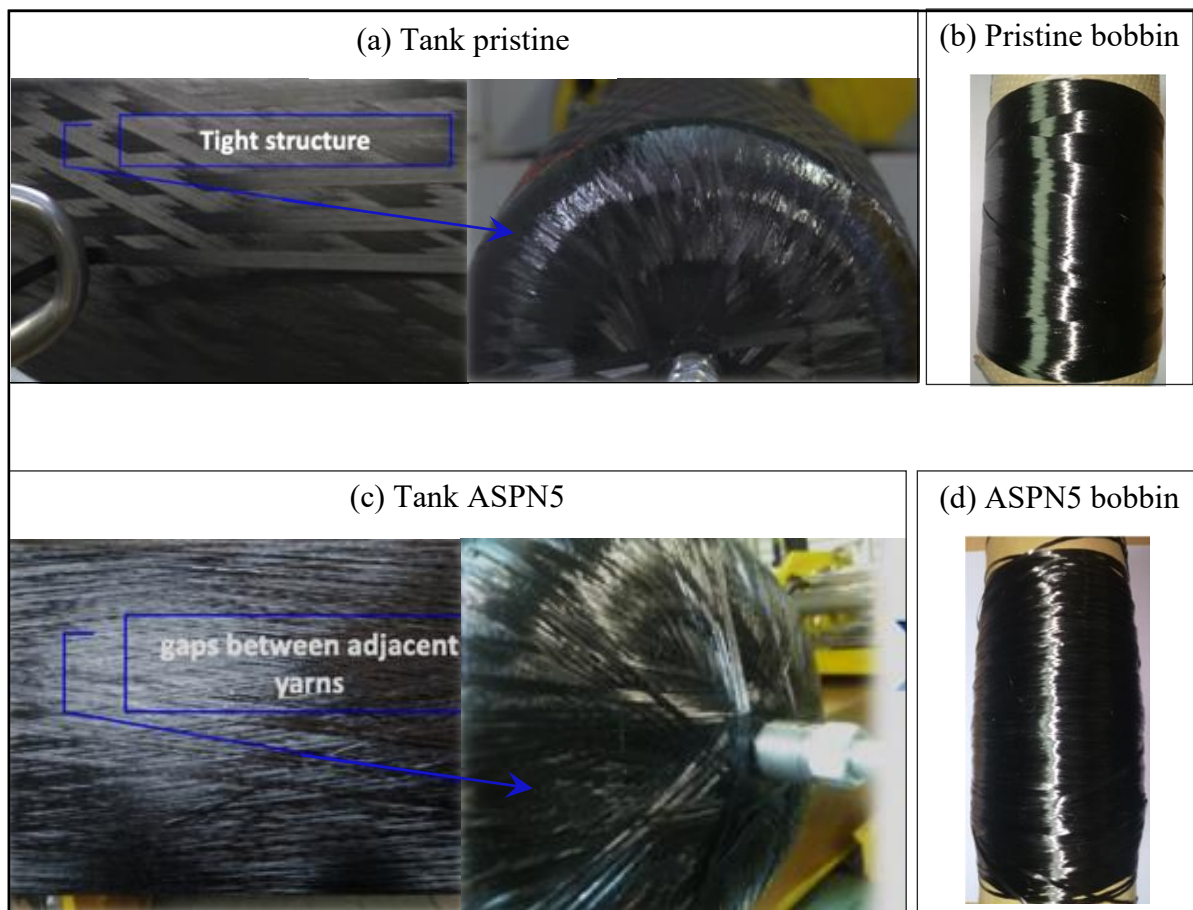


Figure 4.4-7 Images of (a) (c) tanks manufactured with (b) (d) pristine CFs and ASPN5 treated CFs.

CHAPTER 5 DISCUSSION

5.1 The interaction between active screen plasma and CF

As reported in Chapter 4 and summarised in Table 5.1, active screen plasma treatments have improved the interfacial adhesion of CF to epoxy resin and multiple mechanical properties of CF reinforced composites under optimised treatment condition (ASPN5 & ASPAr5-10%) without tensile strength degradation. Therefore, understanding the mechanisms involved in the interaction between the active screen plasma and the CF surface is very important from both a scientific and technological point-of-view.

Table 5.1 Summary of properties of single fibres, interfaces and composites under optimised ASP treatments conditions.

		Pristine	ASPN5	ASPAr5-10%
Single fibre	Weibull scaling parameter for tensile strength (MPa)	2410	2560	3000
Interface	Average IFSS (MPa)	55 ± 12	72 ± 9	77 ± 10
	Weibull scaling parameter for IFSS (MPa)	57	75	81
Woven fabric reinforced Composite	Flexural strength (MPa)	755 ± 84	769 ± 43	783 ± 18
	ILSS (MPa)	44 ± 3	46 ± 2	44 ± 4
	Average steady toughness (J/m ²)	614 ± 49	675 ± 37	none
Unidirectional CF reinforced Composite	Shear strength (MPa)	66 ± 3	68 ± 7	none
	Longitudinal flexural strength (MPa)	872 ± 9	1015 ± 15	none
	Transversal flexural strength (MPa)	65 ± 10	76 ± 11	none

The plasma modification of CFs is a process including a series of interactions between the fibre surface being treated and highly active species, such as electrons, ions and radicals, which are generated from the collisions between the accelerated electrons and gas molecules in plasma reactors [159, 171, 172]. These interactions between the CF surface and the active species can lead to desirable functionalisation and degradation reactions on the fibre surfaces depending on the type of plasma techniques used and the operation conditions [173, 174].

As discussed in Section 2.6.6, the literature shows a wide range of plasma techniques and processing conditions. These plasma surface treatments are reported consistently to remove contaminations from the surface, roughen the surface, change the surface microstructures, increase surface energy and/or introduce functional groups, but most of these plasma treatments could also cause tensile strength damage [162].

Generally, these changes are attributed to chemical and physical interactions between the fibre surface and the plasma active species. The chemical interaction is based on the reactions between the surface carbon atoms and the chemically active species, e.g. atomic nitrogen (radical) [15, 175] and/or molecular oxygen [2, 6, 176], forming functional groups that can improve the surface energy and reactivity. The physical interaction proceeds through the bombardment of the fibre surface with energetic charged species or ions, such as H^+ [177], Ar^+ [178-180] or O_2^+ [2, 6, 176] ions, leading to changes in surface structure and/or degradation in tensile property. Therefore, it can be deduced that the functionalisation reactions are mainly initiated by the interaction with radicals and the degradation reactions related to the etching effect are mainly initiated by the bombardment of ions. The results of Solís-Fernández *et.al* bring some experimental support to this hypothesis [181]. They distinguished the chemical and the physical interactions by conducting a comparative study of ultraviolet (UV) oxidation and dielectric barrier discharge (DBD) air plasma treatments. Their results proved that the chemical

attack from the UV oxidation selectively created atomic vacancies at a limited number of surface locations, which subsequently attributed to the formation of functional groups. By contrast, the physical attack observed in DBD air plasma caused etching effect at random locations on the sample surface, leading to microstructural defects and strength damage.

Despite interactions with the fibre surface being treated, plasma active species could disappear through recombination in the forms of electron-ion and radical-radical, in which the former process is much faster than the latter one. According to Pejovic *et.al*, the rate constant is generally in the order of 10^{-7} cm³/sec for the electron-ion recombination and 10^{-33} cm³/sec for the radical-radical recombination [182]. This indicates that the radicals possess a longer lifetime than the ions and the electrons.

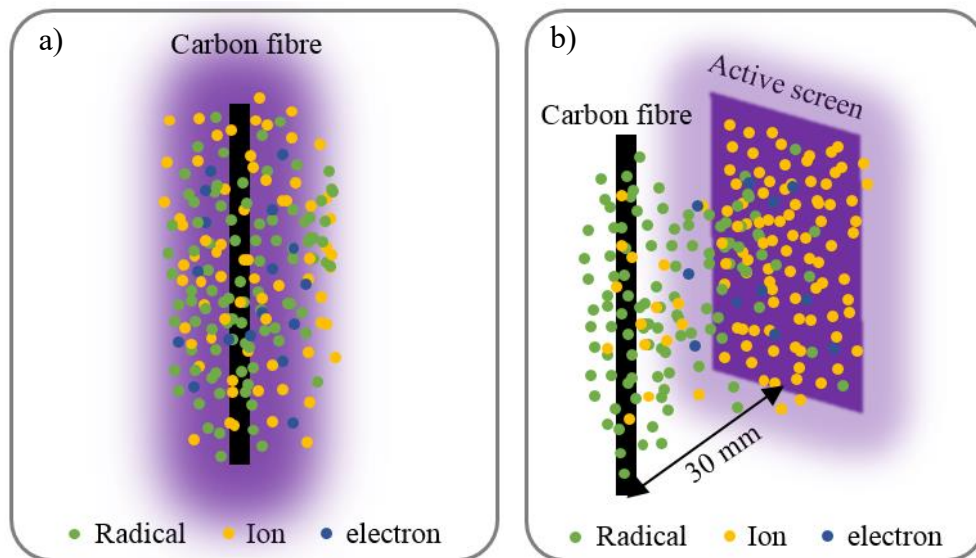


Figure 5.1 Schematic mechanisms of (a) conventional plasma treatment and (b) active screen plasma treatment.

The interactions between the fibre surface and these active plasma species are mainly determined by the type of plasma techniques. For most conventional direct plasma techniques, such as RF, MW and direct current (DC) plasmas, the treated CFs is immersed in the plasma as

schematically shown in Figure 5.1 (a). All active species, electrons and ions as well as radicals interact with the surface of the CFs. As a result, the functionalised fibre surface from these conventional plasma treatments is normally accompanied by surface damages due to the inevitable ions bombardment induced etching effect [11, 14].

However, during the active screen plasma treatments in this research (Figure 5.1 (b)), the CFs were set appropriate 30 mm away from the active screen, where the plasma was generated, in order to separate the radicals from the ions and electrons with the consideration of the large lifetime difference. Therefore, the surface of CFs was mainly exposed to the stream of radicals in the ASP reactor. Such a treatment setting is supported by the findings of Inagaki, that the concentration of radical shows negligible decrease with increasing the distance between the treated sample and the plasma up to 100 cm, while the concentration of electron and ion decreases rapidly with increasing the distance [159]. According to their experimental results, the relative concentration of ions of hydrogen plasma drops to about 10% at a distance of 10 cm [159].

Therefore, in essence, active screen plasma treatment is a remote plasma or post-plasma treatment [2, 183]. The radicals are separated from the ions and electrons acting as the predominant component in the active screen plasma, and the ions and electrons are restricted to the active screen acting as the minor components on the sample surfaces. Accordingly, as the schematic diagram shown in Figure 5.1 (b), whilst radicles can easily reach CF surface for the desirable functionalisation reactions, limited number of ions could bombard the CF surface thus avoiding or reducing the undesirable degradation reactions.

In addition, plasma-surface interactions are closely related to the operating parameters. When a plasma technique is applied, the plasma species are created by the collisions between the

charged electrons and the gas molecules, which are mainly determined by their mean free path as the equation shown below [184].

$$\lambda_i = \frac{k_B T}{\sqrt{2} \pi P d^2} \quad (5-1)$$

where k_B is Boltzmann constant, $J \cdot K^{-1}$; T is temperature, $^{\circ}C$; P is total pressure, Pa; and d is the diameter of the species, m.

According to the mean free path equation (5-1), the plasma treatment with high-pressure brings a high discharge density, frequent collisions (short mean free paths) and low energetic species, as evidenced by the atmospheric-pressure plasma treatments [185]. On the contrary, the plasma species from a low-pressure plasma treatment can travel long distances between collisions, and therefore the surface exposed to the low-pressure plasma are subjected to a low density but of high energetic species, as mentioned in Section 2.6.6.1. From this point of view, the mild pressure (75 Pa) in this research allowed adequate amount of active species with low energy. However, as explained by Gallo and Dong in Figure 5.2, the energy level of these excited species in the active screen plasma is higher than the strength of the chemical bond in the CFs [129]. Therefore, the radicals from the active screen plasma can interact with the CF surface to trigger chemical reactions and structural changes. In the meanwhile, the ion bombardment which causes tensile degradation can be weakened because of their low energies.

The gases used for plasma treatment put an effect on the interactions between plasma species and CF surface as well. It can be deduced from Equation 5-1 that the active species with larger diameter possess a shorter mean free path, leading to a lower concentration of species around the CFs during the ASP treatments. On the contrary, the active species with a smaller diameter can travel longer to functionalise and bombard the fibre surface. Accordingly, the

functionalisation from the active species, as well as the ions bombardment varies when using different gases (plasma species with different diameters) during ASP treatment.

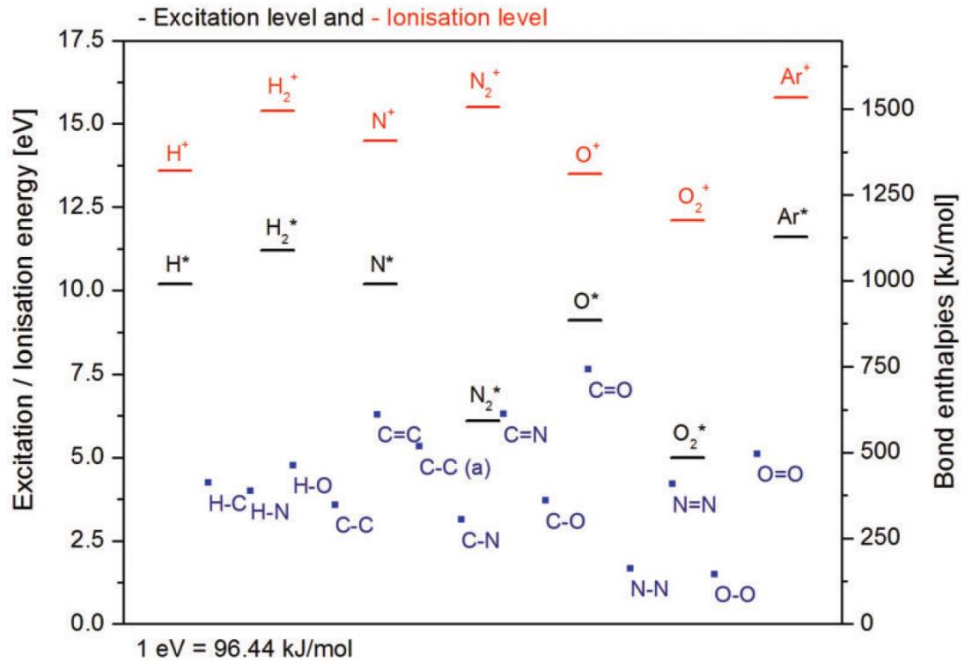


Figure 5.2 Illustration of the energy levels of active species in the plasma and the strength of chemical bonds found in CFs [129].

5.2 Effects of ASP modification on tensile property of CFs

As described in the literature review (Section 2.6.1), previous studies have reported that the plasma treatments can damage the fibre surfaces due to the ions bombardment, leading to a reduction of single fibre strength [14, 186, 187]. As exemplified in Figure 5.3 reported by Sharma *et al.*, plasma treatment significantly decreased the tensile load taken by the CFs before failure when comparing to the untreated CFs [188]. However, this is in contrast with the results of this research, which have been reported in Session 4.2.3, the tensile strength of active screen plasma modified CFs is indeed higher than that of pristine CFs with only one exception of ASPN8 (Table 4.2-3). The seemingly contradictory results could be attributed to the nature of the active screen plasma used in this research, the interaction between the CF surface and the plasma species, and the resulting surface structure.

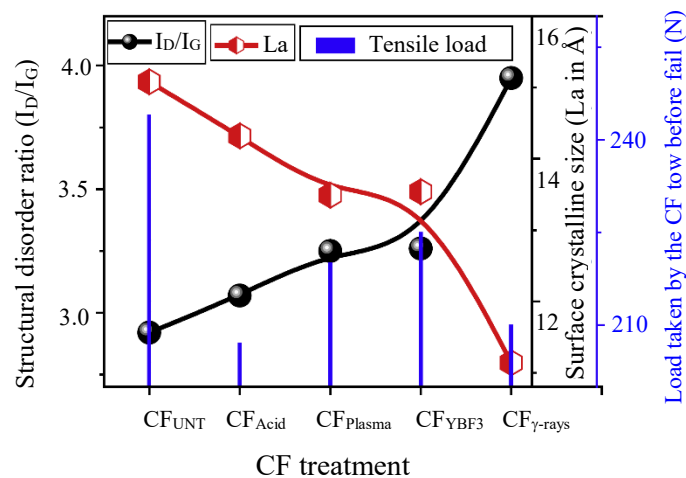


Figure 5.3 Variation of structural disorder parameter I_D/I_G , surface crystalline size L_a and tensile load of carbon fibres as a function of various carbon fibre treatments. (UNT-untreated; YBF₃-nano ytterbium fluoride particles treated) [188].

Referring to Sharma *et al.* (Figure 5.3), the reduction in the tensile property of CFs following conventional plasma treatments is accompanied by the increase in structural disorder ratio (I_D/I_G)

and the decrease in surface crystallite size La [188]. However, for the active screen plasma treated CFs, as evidenced in Table 5.2, the I_D/I_G intensity ratio is unchanged or slightly decreased (except for ASPN5) and both the crystallite height Lc and width La increased (except for ASPN2) with regard to that of the pristine CFs in this research. It can be found that the correlation among the single fibre strength, structural disorder ratio and surface crystallite size is still valid for the ASP treated CFs, although the effect of plasma treatment on single fibre strength is opposite. This is because the ASP treatment has the capability to separate the radicals from ions and electrons to modify the CF surface, resulting in a decreased structural disorder (I_D/I_G) and an increased surface crystallite size (La and Lc).

Table 5.2 Surface crystalline dimensions, structural disorder ratio and tensile strength of pristine and ASP treated CFs.

Sample code	Tensile strength (GPa)	Lc (nm)	La (nm)	I_D/I_G
Pristine	2.41	1.32	3.95	1.014
ASPN2	2.81	1.28	3.52	1.002
ASPN5	2.56	1.38	5.82	1.018
ASPN8	2.07	1.47	6.31	1.014
ASPAr5-5%	3.27	1.34	4.48	1.009
ASPAr5-10%	3.00	1.34	4.41	1.005
ASPAr5-15%	2.83	1.33	4.39	1.004

As discussed in Chapter 2, the PAN-derived fibres are characterised by extensively wrinkled and interlinked turbostratic layers (Figure 2.3), which exhibit a preferential orientation along the fibre axis and thus results in an excellent tensile strength. Internal strain is formed within these CF turbostratic structures during the stretching of the PAN fibre to form this preferential orientation, which has been confirmed by Li *et al.* through a careful analysis of wide-angle X-ray diffraction and Raman spectroscopy [189]. However, the strike of the energetic plasma

species during ASP treatments can increase the mobility of the carbon atoms, thus the C-C bonds and carbon planes potentially slide and rotate to release the internal strain and then straighten along the fibre axis. As a result, the crystallites stack closely and orderly, which consequently increases the size of the crystallites (L_a and L_c) and decreases the disorder degree (I_D/I_G) of the fibres.

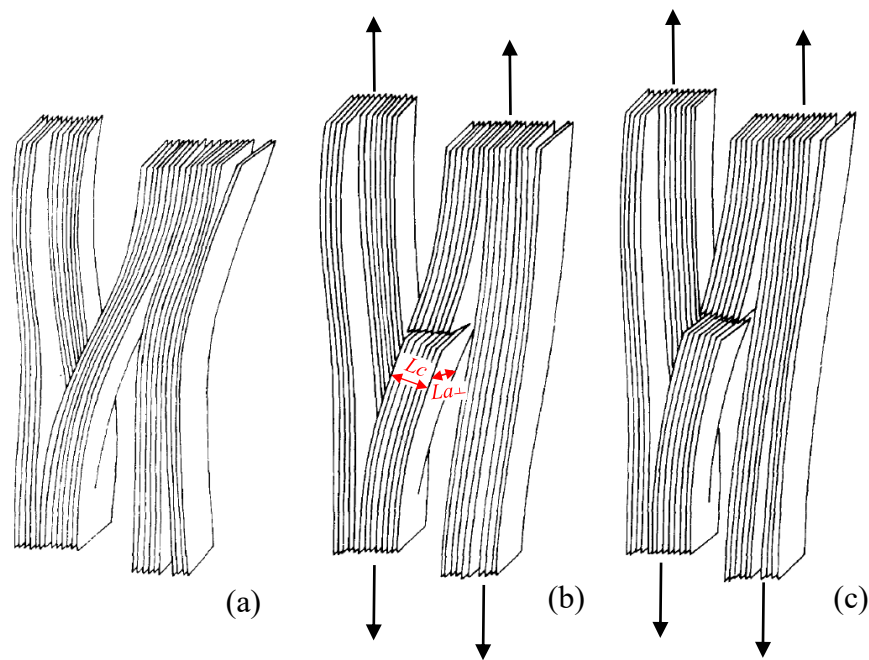


Figure 5.4 Reynolds and Sharp mechanism of tensile failure in misoriented crystallite [190].

According to the Reynolds-Sharp theory, as illustrated in Figure 5.4, the failure of a single fibre under tension initiates from a misoriented crystallite (Figure 5.4 (a)). After rupturing the basal plane by the shear stress which is parallel to these planes, the crack propagates in the direction of $L_{a\perp}$ and L_c (Figure 5.4 (b)), causing the complete failure of the disoriented crystallite (Figure 5.4 (c)) and finally the failure of single fibre [191]. Based on this failure theory, Bennett and Johnson pointed out that the tensile failure of a single fibre does not occur at the internal voids, but occurs in the well graphitised lamellar structures at the surface of the internal voids, which is associated with the accumulated shear stress concentration within the

ordered structure [56, 190]. They also established the relationship between the structural parameters and the tensile strength of single fibres. That is, large crystallites with layer planes parallel to the fibre axis do not initiate failure.

Therefore, for the ASP treatments carried out in this research, the changes in the turbostratic structure could align the enlarged crystallites with respect to the fibre axis (preferential orientation), leading to increased tensile strength. On the other hand, the bombardment of ions can be eliminated or reduced comparing to the conventional plasma treatments due to the reduced number of ions that could reach the CF surfaces. This limited bombardment is beneficial to minimise the etching effect but still to remove the weakly bonded regions on the carbon fibre surfaces, which contributes to clean the surfaces and diminish the surface critical-sized flaws that act as stress concentrators during tensile tests. This is the main reason for the tensile strength increase of ASPN2 treated CFs.

However, prolonged ASP treatment could still increase the potential of surface damages and hence reduce CF strength due to the accumulated ions bombardment on the CF surface, as evidenced by the I_D/I_G increase of ASPN5 treated CFs and the strength decrease of ASPN8 treated CFs. This agrees well with the findings of conventional plasma treatments showing that the severe ions bombardment increased surface disorder degree, damaged fibre surface and reduced fibre strength [1, 14, 186]. The degradation reactions are indicated by the widening of D band for ASPN8 (Table 4.1-2) as well, suggesting that defects or edge planes were created at the surface of the CFs by the long-time ASP treatments [12].

Another surprising observation from Table 5.2 is that the addition of a small amount of argon into the ASP treatments produced a remarkable effect on the disordered structure and the tensile strength of the ASPAr treated CFs as compared with that for ASPN treated one. As shown in

Table 4.1-2 and Table 5.2, comparing to the ASPN treatments, the ASPAr treatments showed less influence on the position and the width of D band, as well as the crystallite size (L_a and L_c), which is an indication of the reduced interactions with active plasma species. Moreover, the crystallite width L_a and the I_D/I_G intensity ratio decreased gradually with increasing the argon concentration in the gas mixtures. These changes could be attributed to the difference in the mean free path of argon, nitrogen and hydrogen species.

As can be seen from Table 5.3, the diameters of argon species are greater than that of the nitrogen and hydrogen species, which means that the argon species have shorter mean free paths comparing to nitrogen and hydrogen species according to Equation 5-1. As a result, the ion concentration around the CFs away from the active screen is lower during the ASPAr treatments than during the ASPN treatments. That is to say, when nitrogen/hydrogen was partially replaced by argon during the ASPAr treatments, ions etching induced degradation effect can be further reduced due to the reduced ions bombardment.

Table 5.3 The atomic diameter and ionic diameter of H, N and Ar elements [192].

Element symbol	Atomic diameter [Å]	Ionic diameter [Å]
H	1.06	0.50
N	1.12	1.30
Ar	1.42	1.42

However, the functionalisation reactions conferred by the radicals of argon, nitrogen and hydrogen still occurred and even have a powerful impact on the CF structures during ASPAr treatments, as evidenced by the decreased I_D/I_G intensity ratios and the decreased values of L_a and L_c with relative to that of ASPN5 treated CFs as shown in Table 5.2. This indicates that a more ordered but smaller graphitic structure may have been formed with the addition of argon

in the ASP treatments (i.e. ASPAr). This structure contributes to improving the preferential orientation of fibres with respect to the fibre axis as the structure of ASPN treated CFs, but it performs better than that of ASPN treated CFs at dissipating shear stress concentration [56, 190]. Therefore, an improved tensile strength has been achieved. However, the tensile strength of the ASPAr treated CFs decreased with further increasing the argon concentration in the gas mixture. This could be attributed to the increasing number of argon radicals in the plasma, which possess a short mean free path thus failing to functionalise the CF surfaces.

5.3 Effects of ASP modification on CF/resin interface

From the results of push-out tests reported in Section 4.3, it can be seen that under the treatment conditions of ASPN5 and ASPAr5-10%, the average interfacial shear strength of CF/epoxy composites has been increased by 31% and 40%, respectively. The post observation (Figure 4.3-8) of pushed-out CFs also shows that the failure of the fibre-epoxy system with ASP modified CFs occurred within the epoxy resin rather than at the fibre/epoxy interface, as illustrated in Figure 5.5. These results suggest that the adhesion of CFs to epoxy resin are enhanced after ASP treatments. According to the previous discussion, it is clear that the ASP treatment is able to activate and functionalise the CF surface and enhance the adhesion of fibre surface to epoxy resin most probably through changing surface topography, improving surface chemistry and wettability [32]. These three types of changes introduced by ASP treatments will be discussed below, respectively.

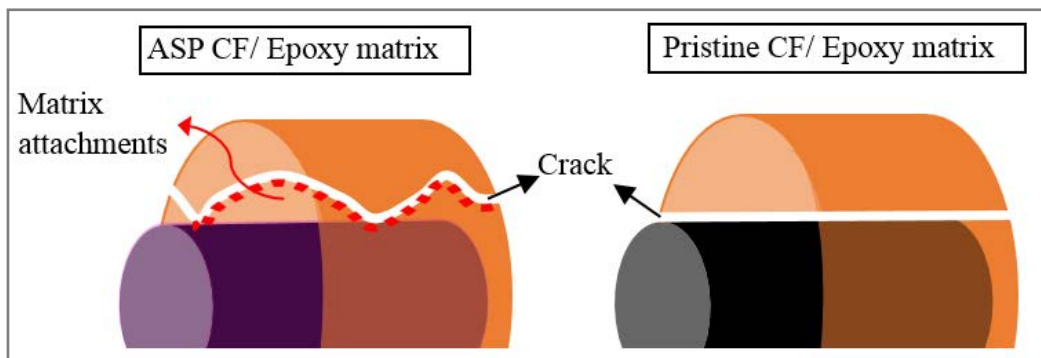


Figure 5.5 Schematic diagrams of interfacial failure mode of ASP CF/epoxy matrix and pristine CF/epoxy matrix.

5.3.1 Changes in surface topography

SEM and AFM observations have been conducted to investigate the influence of the ASP treatments on the surface morphology of CF, and it can be seen from the AFM images (Figure 4.1-1) that the surface of the pristine fibre is covered by a thin sizing layer with

some sizing protrusions. After ASP treatment under the conditions of ASPN5 and ASPAr5-10%, most sizing layers were removed, leaving clean fibre surfaces as evidenced by the well-defined surface grooves formed during CF manufacturing, especially for the ASPAr5-10% treatment. Clearly, the ASP treatments mildly roughened the surface of CFs and the introduction of argon contributed to a rougher surface. This could be explained as follows: although the number of ions reached CF surfaces is low due to the remote plasma nature of the ASP, the bombardment of these ions from the active screen plasma could not only remove the surface sizing layer but also eject some weakly bonded atoms or molecules on the fibre surface, thus leaving the notches on the fibre surfaces [193].

The increased surface roughness of ASP treated CFs is useful for reinforcing composites, because the roughened surface expands the available surface area for the attachment of active groups and increases the contact area with the epoxy resin, leading to enhanced interfacial adhesion in composites [193-195]. Also, the roughened surface could provide more and stronger mechanical interlocking (physical bonding) sites for the epoxy resin [162, 193]. In addition to this, the clean fibre surface revealed by the advanced ASP treatments could also increase the Van der Waals binding and hence the adhesion of epoxy resin on the CF surface can be achieved effectively.

5.3.2 Increase of chemical bonding

The surface chemical composition of CFs is of great importance in ensuring good adhesion to epoxy resin in resulting composites. Therefore, the surface composition of CFs after the ASP treatments has been examined by XPS in this research.

As can be seen from Figure 4.1-7, while carbon and oxygen mainly appeared on the surface of pristine CF, a small amount of nitrogen also presented on the fibre surfaces after both ASPN5

and ASPAr5-10% treatments. However, from the quantified analysis shown in Table 4.1-4, the pristine CF also exhibited very high values of nitrogen and oxygen contents but this should be related to the surface sizing material, which can be removed by 5-minutes ASP treatment as revealed by AFM images (Figure 4.1-3). It is well-known that the non-carbon elements, such as nitrogen and oxygen, are largely removed after the high-temperature carbonisation/graphitisation in inert gas and the carbon content of the carbonised fibres should be > 90% thereafter [66, 163]. Therefore, it can be deduced based on the above discussion that the nitrogen and oxygen contents measured from the surfaces of ASPN5 and ASPAr5-10% treated CFs must be introduced by the ASP treatments.

Furthermore, the deconvolution analysis of C 1s peaks (Figure 4.1-8) further reveals the effects of ASPN5 and ASPAr5-10% plasma on the fibre surfaces treated. It can be seen that the C-C group (284.5 eV) decreased after ASPN5 treatment, indicating that the C-C bonds are broken and changed to other groups. The C-O group (286.2 eV) decreased after both ASPN5 and ASPAr5-10% treatments but more prominently after ASPN5 treatment. Oxygen-containing groups were also identified on the O 1s spectra (Figure 4.1-9) after both treatments, which could be attributed to the post-reactions of carbon radicals with oxygen in the air after the ASP treatments. Nevertheless, the oxygen-containing functional groups could also contribute to the adhesion of ASP treated CFs to epoxy resin in composites.

The nitrogen content has increased to 3.7% after the ASPN5 treatment as shown in Table 4.1- 4 and the deconvolution of N 1s peak further indicates that the nitrogen-containing groups have been introduced on the fibre surface by ASPN5 treatment. As shown from Figure 4.1-10 (b), pyrrolic N (400.1 eV) and oxidised N (401.8 - 402.8 eV) were detected on ASPN5 treated CF surface. When nitrogen/hydrogen was partially replaced by argon (ASPAr5-10%), the nitrogen content on the surface of CF decreased (0.9%). However, a new nitrogen-containing group,

pyridinic N (398.6 eV), has been detected on the treated fibre surface as presented on Figure 4.1-10 (c).

These nitrogen-containing groups are believed to be the reaction products of fibre surface active sites with active nitrogen species in N_2-H_2 plasma environment (ASPN5) [196, 197]. The possible process could be proposed as follows: the attack of the energetic plasma species broke the covalent chemical bonds on the fibre surface to create active sites, which reacted with active nitrogen in the plasma environment to form various nitrogen-containing groups, e.g., pyrrolic N and pyridinic N. Some of these newly generated nitrogen-containing groups are unstable and react with oxygen to form oxidised N [196]. Moreover, the large number of dangling carbon bonds present on the surface of PAN-CFs could also provide active sites for reaction and the attached nitrogen species form nitrogen-containing functional groups [129, 162]. The generation of pyridinic N from the ASPAr5-10% treatment is probably due to the interaction of the nitrogen species with the active sites of vacant carbon bond created by the collisions of argon species. This is supported by the findings by Wang *et al.* that the generated pyrrolic N groups, located at the edges, voids and/or defects of the fibre structure, could be decomposed by the plasma species to form pyridinic N groups [198].

To sum up, nitrogen and oxygen-containing functional groups have been formed on the CF surface by ASP treatments and they are contributing to improving the chemical bonding with epoxy matrix in resulting composites.

5.3.3 Improvement of surface wettability

A good wettability of a CF surface is admired for the strong adhesion between the CF and the epoxy resin. However, because of the chemical inertness and low free energy of the CF surfaces, it is difficult to form strong adhesion between the CFs and the epoxy resin. Thus, the effect of

ASP treatment on surface wettability with N₂-H₂ and N₂-H₂-Ar has been examined by contact angle with epoxy droplets and dynamic vapour sorption (DVS) test.

From the photos of contact angles between the fibre surface and epoxy resin, it can be seen from Figure 4.2-1 that the contact angle of epoxy resin on CFs can be decreased for all ASP treated CFs, such as, from 70.6 ° for pristine CFs to 59.7 °, 58.4 ° and 60.6 ° for ASPN5, ASPAr5-5% and ASPAr5-10% treated CFs, respectively. The contact angle results suggest that epoxy resin is more readily spread on the ASP treated fibre surfaces than on the pristine fibre surface.

The affinity of the fibre surface to water has been improved as well, as evidenced by the DVS results in Table 4.2-2. The adsorbed water content has increased by 22%, 25% and 46% after ASPN5, ASPAr5-5% and ASPAr5-10% treatments respectively. This indicates that the ASP treated CFs possess a larger absorptive capacity of water than pristine CFs and that the addition of argon further increased their adsorptive capacity. These remarkable changes in the resin contact angle and adsorbed water content observed after the ASP treatments indicate the effectively increased wettability of the ASP treated fibre surface.

Generally, the change in the wettability of plasma functionalised surface could be attributed to surface topography and/or surface chemistry [199]. From the view of surface topography, as discussed in Section 5.2.1, the dense and deep grooves on the ASP modified surfaces are beneficial for epoxy droplets to easily spread on the fibre surface and for water molecules to be adsorbed on the CF surface by capillary effect. As for the surface chemistry, the polar functional groups, such as oxygen-containing and nitrogen-containing groups, introduced onto the fibre surface after the ASP treatments should be able to improve the surface polarity and energy. These introduced functional groups also provide sites for water molecules attachment through

hydrogen bonding, as evidenced by the increased chemisorption of ASP modified CFs (Table 4.2-2). Also, the changes in the surface topography and chemistry can also help to increase the surface energy of treated CFs [187] [200]. Consequently, the surface wettability of ASP treated CFs has been successfully improved, leading to significantly enhanced adhesion of the CFs to the epoxy resin.

However, a hydrophobic recovery was observed both from the contact angle tests and DVS tests after exposure the ASP treated fibres to air as shown in Figures 4.2-3 and 4.2-6. The oxidative scissions and the evaporative loss of the nitrogen functional groups are usually used to explain this phenomenon [201]. Similar hydrophobic recovery behaviour after plasma treatments was reported in polymer materials, although the rate of decay depends on the nature of the substrate, the plasma treatment conditions, and the aging environment [202-204].

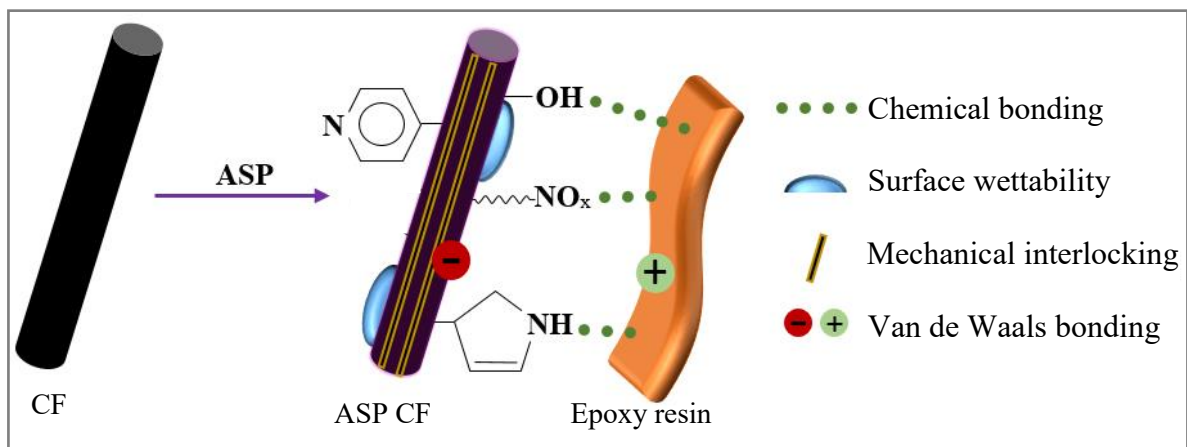


Figure 5.6 Schematic diagram of interfacial bonding mechanisms of ASP CF/epoxy resin.

Based on the above discussion of surface morphology, surface chemistry and surface wettability, the interfacial adhesion enhancement mechanisms of ASP treated CFs reinforced epoxy composites could be mainly attributed to 1) the increased Van der Waals bonding due to a more intimate contact provided after the removal of surface contaminations; 2) the enhanced

mechanical interlocking from the adequately roughened surface ; 3) the increased chemical bonding between the introduced functional groups on the fibre surface and the matrix; and 4) the improved surface wettability of CFs, as schematically illustrated in Figure 5.6.

5.4 Effects of ASP modification on CFs reinforced epoxy composite

The experimental results reported in Section 4.4 indicate that ASP treatments can affect the mechanical properties of ASP modified CF/epoxy composites. As has been shown in Figure 4.4-2 and Table 4.4-1 and summarised in Table 5.1, in general, the flexural strength and the interlaminar shear strength of ASP treated woven fabric/epoxy composites, as well as the shear strength, longitudinal and transversal flexural strengths of ASP treated unidirectional CF/epoxy composites, are higher than those of the pristine material. The propellant tank made with the ASPN5 modified CFs has also shown at least 12% improvement in the average strain when comparing to the one made with the pristine CFs (Table 4.4-2). These mechanical property improvements of the composites with ASP modified CFs could be considered to be mainly related to the improved interfacial shear strength and the increased fibre strength.

It is known that when the progressive load is applied on composites during the mechanical tests, the reinforcing fibres of the composites break firstly at locations determined by the stochastic fibre strength and local load distribution [205]. Then the load that the breakage fibre previously taken needs to be transferred to its neighbouring fibres through the matrix shear. However, as revealed by the fractured samples (Figures 4.4-3), the weak interface (low IFSS) of the pristine CF/epoxy composites is not able to transfer the load effectively, leading to long fibre delamination and subsequent pull-out (Figures 4.4-3 (a)). Thus, a large proportion of fibre length failed to function before the failure of the sample. Unsurprisingly, the load that the pristine CF/epoxy composites taken during the mechanical tests is relatively low. In contrast, the fracture morphologies of composites with modified CFs (Figures 4.4-3 (b) and (c)) show bonded fibres with well-attached epoxy resin, implying that the enhanced interface (Increased IFSS, Table 4.3-1) after the ASP treatments performed well at transferring the load, contributing to improving the mechanical properties of composites. In addition to that, as have discussed

earlier (Section 5.2), the ASP treated CFs exhibit increased single fibre tensile strength (Table 4.2-3), which is beneficial to lower the possibility of early failure of the reinforcing fibres. Therefore, the composites with ASP modified CFs showed increased shear and flexural strengths in general.

From previous researches, it may be expected that the toughness of the ASP CF/epoxy composites would decrease as the increased interfacial adhesion may induce premature failure (brittle failure) of the composites [120, 205]. Indeed, during the load-transferring from a broken fibre to its neighbouring fibres, a strong fibre/matrix interface provides adequate shear strength, but also raises the possibility of generating local stress concentration. If the local stress concentration could not be diffused or dissipated in any manner of interfacial debonding [206], such as fibre/matrix friction [207], fibre pull-out [117, 208] and/or stress relief in the interface [209], it will accumulate in neighbouring fibres, leading to a cluster of fibre breaks within the composite and consequently early brittle failure [210-213]. However, as can be seen from Figure 4.4-5, the average initial fracture toughness and the average steady-state toughness of the composites were increased by 24% and 5% respectively when reinforced by ASPN5 treated CFs. This is because more energy is required to transfer load through matrix shear (ASP strengthened interface) than through fibre/matrix debonding (Pristine CF/epoxy interface).

Besides, the fracture morphologies (Figure 4.4-6 (b)) also suggest the crack tips of the ASP CF/epoxy sample were bunted by crack deflection. So comparing to a near straight breaking trace line presented on the pristine CF/epoxy composite (Figure 4.4-6 (a)), a zigzagging trace line was exhibited on the ASP treated CF/epoxy composites (Figure 4.4-6 (b)). This phenomenon again indicates that the ASP enhanced interface redistributed the stress concentration at fibre breaks via crack tip blunting and crack deflection, thus contributing to a

high degree of energy absorption of the composites. Similar improvement has also been observed for the composites with nanostructure coated interface [8, 9].

It could be concluded based on the above analysis that ASP treatments of CFs could lead to mainly cohesive failure of the ASP CF/epoxy composites due to the improved interfacial strength to force the crack to propagate through the surrounding matrix instead of the immediate interface region. More energy is required for the cracks propagation and deflection [213]. Thereby, ASP treatments have successfully improved the flexural strength, shear strengths and fracture toughness simultaneously.

It should be indicated that the improvement in the mechanical properties of single fibre strength and CF/matrix interfacial shear strength seems more significant than the macro mechanical properties of the composites reinforced by ASP treated CFs. This could be attributed to the fact that the mechanical properties of composites not only depend on the strength of CFs and the CF/matrix interfacial shear strength but also the quality of the composites manufactured. After many years of research, the manufacturing process for the production of untreated or pristine CFs reinforced composites has been fully optimised; however, such process conditions are not necessarily suitable for ASP treated CFs. Hence, it is essential to investigate the optimal processing conditions for manufacturing ASP treated CFs reinforced composites thus realising the full potential of ASP treated CFs for high-performance composites.

CHAPTER 6 CONCLUSIONS

In the present project, advanced active screen plasma technology has been developed to modify the PAN-derived carbon fibres surfaces. The morphology, microstructure and chemistry of the treated fibre surfaces have been characterised and the properties of resultant fibres, fibre/epoxy interface and fibre-reinforced composites have been fully investigated. Based on the experimental results and discussion presented in Chapters 4 and 5, the key findings and implications can be drawn as follows:

Part I – Surface modification of CF surfaces

1. An advanced active surface plasma technology has been developed by exploring the remote-plasma benefits, selecting optimal treatment duration between 2-8 minutes and identifying favourable gas compositions from gas mixtures of N₂-H₂ and N₂-H₂-Ar.
2. The active screen plasma (ASP) treatment can clean and slightly roughen the carbon fibre (CF) surface without introducing undue surface damages due to the reduced ions bombardment of the remote plasma of the ASP technology.
3. Active screen plasma can effectively increase the average crystalline size (height increased from 1.32 nm to 1.47 nm and width increased from 3.95 nm to 6.31 nm).
4. Active screen plasma modification with gas mixtures of N₂-H₂ and N₂-H₂-Ar can change the surface chemistry by removing the sizing layer and introducing new functional groups, such as pyrrolic N, pyridinic N and oxidised N groups, to CF surfaces.
5. Active screen plasma modification can improve the wettability of the CF surface as evidenced by the decreased contact angle against epoxy resin from 71 ° to 58 °, which could be attributed to the introduction of surface functional groups and a slightly

- roughened surface resulting from the active screen plasma treatments.
6. Active screen plasma modification can improve the affinity of CF surfaces to water mainly through chemisorption (from 2.79% to 4.38%), which is associated with the introduced surface functional groups.
 7. The functionalised CF surfaces by active screen plasma treatments exhibit a hydrophobic recovery upon re-exposure to air. The degradation rate after 10 days can be up to 5%.
 8. The advanced active screen plasma treatment can lead to increased (rather than decreased for other plasma treatments) single fibre tensile strength by 16.6% and 35.7% respectively for ASPN and ASPAr treated CFs due to the changes in the fibre structure and the removal of the weakly bonded regions on the fibre surface.
 9. The morphological, structural and chemical changes, as well as the improvements in wettability and tensile strength under the nitrogen-hydrogen ASP treatments with the introduction of argon could be attributed to the shorter mean free path of argon species as compared with that of nitrogen and hydrogen species as the former has a larger diameter than the latter.

Part II – Interfacial property between fibre and epoxy resin

10. Advanced nano-indentation based push-out methodology has been developed in this study, including sample preparation, testing procedures and data interpretation, to effectively probe the interfacial shear strength for industrial composites with multiple CFs.
11. The interfacial shear strength between the active screen plasma treated CFs and epoxy resin has been improved by 32% when using ASPN5 treated CFs and 41% when using

ASP5-10% treated CFs, as disclosed by single fibre push-out tests.

12. The interfacial adhesion enhancement mechanisms of ASP treated CFs reinforced epoxy composites could be mainly attributed to 1) the increased Van der Waals bonding due to a more intimate contact provided by the removal of surface contaminations; 2) the enhanced mechanical interlocking from the increased surface roughness; 3) the increased chemical bonding between the introduced functional groups on the fibre surface and the matrix; and 4) the improved surface wettability of CFs.

Part III – Mechanical properties of CF reinforced composites

13. Active screen plasma technique can increase the flexural strength (from 755 MPa to 783 MPa) and the interlaminar shear strength (from 44 MPa to 46 MPa) of the woven fabric/epoxy composites, as well as the shear strength (from 66 MPa to 68 MPa), the longitudinal (from 872 MPa to 1015 MPa) and the transversal flexural strengths (from 65 MPa to 76 MPa) of the unidirectional CF/epoxy composites.
14. Active screen plasma enhanced interface can redistribute the stress concentration at fibre breaks via crack tip blunting and crack deflection, leading to increased fracture toughness of resulting composites (29% and 10% increase in the average initial fracture toughness and the average steady-state toughness).

CHAPTER 7 FUTURE WORK

The present project has shown that the adhesion of carbon fibre surface to epoxy resin can be improved effectively by the advanced active screen plasma modification of carbon fibres. However, the application of this technology to carbon fibre-based composites is still at its early stage and deserves more attention and researches. Therefore, based on the results of this research, the following future work is suggested.

Firstly, very promising results have been achieved in this research using active screen plasma with nitrogen-hydrogen and nitrogen-hydrogen-argon to modify carbon fibres. It is interesting to try other gases (for example CH₄, oxygen, etc.) to investigate the potential of different surface morphology, structure and chemistry.

Secondly, the results have shown that the active screen plasma modified fibre surface exhibits a hydrophobic recovery (Point 7, Chapter 6). Therefore, it is important to investigate the possibility of integrating the ASP treatment into composite manufacturing.

Thirdly, the nano-indentation push-out test has shown great potential in evaluating the interfacial properties (Points 10 and 11, Chapter 6). It is worth attempting to apply it to investigate the creep, impact and fatigue behaviours of the fibre/matrix interface.

Finally, the composites manufacturing process should be tailored for the active-screen plasma modified CFs to fully realise the potential of the advanced plasma functionalisation developed from this research for high performance composites.

REFERENCES:

1. D. Akbar and Ü.E. Güngör, *Study of high radio frequency plasma discharge effects on carbon fiber using Raman spectroscopy*. Surface and Coatings Technology, 2014. **240**: p. 233-242.
2. S. Tiwari, et al., *Influence of cold remote nitrogen oxygen plasma treatment on carbon fabric and its composites with specialty polymers*. Journal of Materials Science, 2011. **46**(4): p. 964-974.
3. F. Severini, et al., *Chemical modification of carbon fiber surfaces*. Carbon, 2002. **40**(5): p. 735-741.
4. D. Semitekolos, et al., *Advanced carbon fibre composites via poly methacrylic acid surface treatment; surface analysis and mechanical properties investigation*. Composites Part B: Engineering, 2018. **155**: p. 237-243.
5. J. Zhuoda, *Effects of plasma treatment of carbon fibers on interfacial properties of BMI resin composites*. Surface and Interface Analysis, 2019. **51**(4): p. 458-464.
6. M. Bagheri Borooj, et al., *Influence of oxygen plasma treatment parameters on the properties of carbon fiber*. Journal of adhesion science and Technology, 2016. **30**(21): p. 2372-2382.
7. L. Shang, et al., *Improving the interfacial property of carbon fibre/epoxy resin composites by grafting amine-capped cross-linked poly-itaconic acid*. Surface and Interface Analysis, 2019. **51**(2): p. 199-209.
8. De Luca, F., et al., *Increasing carbon fiber composite strength with a nanostructured "brick-and-mortar" interphase*. Materials Horizons, 2018. **5**(4): p. 668-674.
9. F. De Luca, et al., *"Brick-and-Mortar" nanostructured interphase for glass-fiber-reinforced polymer composites*. ACS applied materials & interfaces, 2018. **10**(8): p. 7352-7361.
10. M. Rallini, et al., *Effect of alumina nanoparticles on the thermal properties of carbon fibre-reinforced composites*. Fire and materials, 2014. **38**(3): p. 339-355.
11. L. Altay, et al., *The effect of atmospheric plasma treatment of recycled carbon fiber at different plasma powers on recycled carbon fiber and its polypropylene composites*. Journal of Applied Polymer Science, 2019. **136**(9): p. 47131.
12. M. A. Montes-Moran and R.J. Young, *Raman spectroscopy study of HM carbon fibres: effect of plasma treatment on the interfacial properties of single fibre/epoxy composites*. Carbon, 2002. **40**(6): p. 845-855.
13. G. Wu, *Oxygen plasma treatment of high performance fibers for composites*. Materials Chemistry and Physics, 2004. **85**(1): p. 81-87.

14. B. Z. Jang, *Control of interfacial adhesion in continuous carbon and Kevlar fiber reinforced polymer composites*. Composites science and technology, 1992. **44**(4): p. 333-349.
15. X. Fu, et al., *Characterization of active screen plasma modified polyurethane surfaces*. Surface and Coatings Technology, 2012. **206**(23): p. 4799-4807.
16. S. C. Gallo and H. Dong, *On the fundamental mechanisms of active screen plasma nitriding*. Vacuum, 2009. **84**(2): p. 321-325.
17. P. Morgan, *Carbon fibers and their composites*. 2005: CRC press.
18. T. A. Edison, *Electric lamp*. 1880. Patent, US223898.
19. T. V. Hughes and C. R. Chambers, *Manufacture of carbon filaments*. 1889. Patent, US405480.
20. W. R. Whitney, *Carbon, filament, and method of making the same*. 1909. Patent, US91690530.
21. R. Bacon and C.T. Moses, *Carbon fibers, from light bulbs to outer space*. High Performance Polymers: Their Origin and Development, 1986. p. 341-353.
22. R. Bacon, *Growth, structure, and properties of graphite whiskers*. Journal of Applied Physics, 1960. **31**(2): p. 283-290.
23. A. Shindo, *Report No. 317*. Government Industrial Research Institute: Osaka, Japan, 1961.
24. A. Shindo, *Process for the preparation of carbon fibers*. 1970. Patent, US3529934.
25. B. A. Newcomb, *Processing, structure, and properties of carbon fibers*. Composites Part A: Applied Science and Manufacturing, 2016. **91**: p. 262-282.
26. S. Ōtani, *On the carbon fiber from the molten pyrolysis products*. Carbon, 1965. **3**(1): p. 31-38.
27. S. Ōtani, et al., *High modulus carbon fibers from pitch materials*. Bulletin of the Chemical Society of Japan, 1972. **45**(12): p. 3710-3714.
28. M. Minus and S. Kumar, *The processing, properties, and structure of carbon fibers*. Jom, 2005. **57**(2): p. 52-58.
29. ReportLinker. *Global and China Carbon Fiber and CFRP Industry Report*. Available at: <https://www.reportlinker.com/p03605799/Global-and-China-Carbon-Fiber-and-CFRP-Industry-Report> (Accessed: 20 March 2021).
30. Markets and Markets. *Carbon Fiber Market by Raw Material (PAN, Pitch, Rayon), Fiber Type (Virgin, Recycled), Product Type, Modulus, Application (Composite, Non-composite), End-use Industry (A & D, Automotive, Wind Energy), and Region - Global Forecast to 2029*. Available at: <https://www.marketsandmarkets.com/Market-Reports/carbon-fiber-396.html> (Accessed 20 March 2021).

31. A. Gupta, D. Paliwal, and P. Bajaj, *Acrylic precursors for carbon fibers*. Journal of Macromolecular Science, Part C: Polymer Reviews, 1991. **31**(1): p. 1-89.
32. P. Bajaj, *Acrylic fibres*. Manufactured Fibre Technology, 1997. p. 406-456.
33. C. D. Han and J. K. Kim, *On the use of time-temperature superposition in multicomponent/multiphase polymer systems*. Polymer, 1993. **34**(12): p. 2533-2539.
34. B. A. Newcomb, et al., *Polyacrylonitrile solution homogeneity study by dynamic shear rheology and the effect on the carbon fiber tensile strength*. Polymer Engineering & Science, 2016. **56**(3): p. 361-370.
35. R. Cheraghi, et al., *Effect of comonomer on the viscoelastic behavior of co-poly (acrylonitrile) solutions*. Journal of Polymer Research, 2016. **23**(10): p. 207.
36. H. G. Chae, et al., *High strength and high modulus carbon fibers*. Carbon, 2015. **93**: p. 81-87.
37. G. P. Daumit, et al., *Formation of melt-spun acrylic fibers which are well suited for thermal conversion to high strength carbon fibers*. 1990. Patent, US4933128.
38. J. Knudsen, *The influence of coagulation variables on the structure and physical properties of an acrylic fiber*. Textile Research Journal, 1963. **33**(1): p. 13-20.
39. D. Grove, P. Desai, and A. Abhiraman, *Exploratory experiments in the conversion of plasticized melt spun PAN-based precursors to carbon fibers*. Carbon, 1988. **26**(3): p. 403-411.
40. E. A. Morris, et al., *High performance carbon fibers from very high molecular weight polyacrylonitrile precursors*. Carbon, 2016. **101**: p. 245-252.
41. Z. Bashir, *A critical review of the stabilisation of polyacrylonitrile*. Carbon, 1991. **29**(8): p. 1081-1090.
42. S. J. Park and G. Y. Heo, *Precursors and manufacturing of carbon fibers*. Carbon Fibers, 2015. p. 31-66.
43. A. Clarke and J. Bailey, *Oxidation of acrylic fibres for carbon fibre formation*. Nature, 1973. **243**(5403): p. 146-150.
44. A. Gupta and I. Harrison, *New aspects in the oxidative stabilization of PAN-based carbon fibers*. Carbon, 1996. **34**(11): p. 1427-1445.
45. T. K. Das, P. Ghosh, and N.C. Das, *Preparation, development, outcomes, and application versatility of carbon fiber-based polymer composites: a review*. Advanced Composites and Hybrid Materials, 2019. p. 1-20.
46. H. Ge, et al., *The microstructure of polyacrylonitrile-stabilized fibers*. Journal of applied polymer science, 2009. **113**(4): p. 2413-2417.

47. C. L. Weitzsacker, M. Bellamy, and P. M. Sherwood, *Studies of the effect of size on carbon fiber surfaces*. Journal of Vacuum Science & Technology A: Vacuum, Surfaces, and Films, 1994. **12**(4): p. 2392-2397.
48. J. Chen, J. Y. Liu, and D. Z. Wang. *Effect of emulsion type sizing agents on the properties of carbon fiber and carbon fiber reinforced polymer matrix composite*. Advanced Materials Research. 2011. **236**: p. 2295-2298.
49. J. Liu, et al., *The preparation of emulsion type sizing agent for carbon fiber and the properties of carbon fiber/vinyl ester resin composites*. Journal of applied polymer science, 2012. **124**(1): p. 864-872.
50. Z. Dai, et al., *Effect of sizing on carbon fiber surface properties and fibers/epoxy interfacial adhesion*. Applied Surface Science, 2011. **257**(15): p. 6980-6985.
51. S. Ōtani and A. Ōya, *Progress of pitch-based carbon fiber in Japan*. ACS Publications, 1986. p: 323-334.
52. Y. Yamada, et al., *Method for the preparation of pitches for spinning carbon fibers*. 1986. Patent, US4606808.
53. J. Barr and B. JB, *High modulus carbon fibers from pitch precursor*. Applied polymer symposia, 1976. **29**: p. 161-173.
54. M. Endo, *Structure of mesophase pitch-based carbon fibres*. Journal of materials science, 1988. **23**(2): p. 598-605.
55. Y. Huang and R. Young, *Effect of fibre microstructure upon the modulus of PAN-and pitch-based carbon fibres*. Carbon, 1995. **33**(2): p. 97-107.
56. D. Johnson, *Structure-property relationships in carbon fibres*. Journal of Physics D: Applied Physics, 1987. **20**(3): p. 286.
57. M. Guigon, A. Oberlin, and G. Desarmot, *Microtexture and structure of some high tensile strength, PAN-base carbon fibres*. Fibre Science and Technology, 1984. **20**(1): p. 55-72.
58. P. Marshall and J. Price, *Topography of carbon fibre surfaces*. Composites, 1991. **22**(5): p. 388-393.
59. W. Kowbel, E. Hippo, and N. Murdie, *Influence of graphitization environment of pan based carbon fibers on microstructure*. Carbon, 1989. **27**(2): p. 219-226.
60. H. Ge, et al., *The skin-core structure of poly (acrylonitrile-itaconic acid) precursor fibers in wet-spinning*. Journal of applied polymer science, 2008. **108**(2): p. 947-952.
61. M. Guigon, A. Oberlin, and G. Desarmot, *Microtexture and structure of some high-modulus, PAN-base carbon fibres*. Fibre Science and Technology, 1984. **20**(3): p. 177-198.

62. X. Qin, et al., *A comparison of the effect of graphitization on microstructures and properties of polyacrylonitrile and mesophase pitch-based carbon fibers*. Carbon, 2012. **50**(12): p. 4459-4469.
63. J. Johnson and D. Thorne, *Effect of internal polymer flaws on strength of carbon fibres prepared- from an acrylic precursor*. Carbon, 1969. **7**(6): p. 659-661.
64. W. Ruland, *X-Ray Studies on Preferred Orientation in Carbon Fibers*. Journal of Applied Physics, 1967. **38**(9): p. 3585-3589.
65. J. Biscoe and B. Warren, *An X-ray study of carbon black*. Journal of Applied Physics, 1942. **13**(6): p. 364-371.
66. X. Huang, *Fabrication and properties of carbon fibers*. Materials, 2009. **2**(4): p. 2369-2403.
67. S. Kumar, W. Adams, and T. Helminiak, *Uniaxial compressive strength of high modulus fibers for composites*. Journal of reinforced plastics and composites, 1988. **7**(2): p. 108-119.
68. S. Kumar, D. Anderson, and A. Crasto, *Carbon fibre compressive strength and its dependence on structure and morphology*. Journal of materials science, 1993. **28**(2): p. 423-439.
69. M. G. J. Dobb and C. R. Park, *Compressional behavior of carbon-fibers*. Journal of materials science, 1990. **25**: p. 829-834.
70. L. M. Manocha, *High performance carbon-carbon composites*. Sadhana, 2003. **28**(1-2): p. 349-358.
71. C. Pradère, et al., *Thermal properties of carbon fibers at very high temperature*. Carbon, 2009. **47**(3): p. 737-743.
72. E. Wolff, *Stiffness-thermal expansion relationships in high modulus carbon fibers*. Journal of composite materials, 1987. **21**(1): p. 81-97.
73. B. Budiansky and N. A. Fleck, *Compressive failure of fibre composites*. Journal of the Mechanics and Physics of Solids, 1993. **41**(1): p. 183-211.
74. A. Bunsell and B. Harris, *Hybrid carbon and glass fibre composites*. Composites, 1974. **5**(4): p. 157-164.
75. Y. Huang and R. J. Young, *Interfacial micromechanics in thermoplastic and thermosetting matrix carbon fibre composites*. Composites Part A: Applied Science And Manufacturing, 1996. **27**(10): p. 973-980.
76. C. Soutis, *Fibre reinforced composites in aircraft construction*. Progress in aerospace sciences, 2005. **41**(2): p. 143-151.
77. S. Laurenzi and M. Marchetti, *Advanced composite materials by resin transfer molding for aerospace applications*. Composites and their properties, 2012: p. 197-226.

78. C. Acquah, et al., *Optimization under uncertainty of a composite fabrication process using a deterministic one-stage approach*. Computers & chemical engineering, 2006. **30**(6-7): p. 947-960.
79. D. Cohen, *Influence of filament winding parameters on composite vessel quality and strength*. Composites Part A: Applied Science and Manufacturing, 1997. **28**(12): p. 1035-1047.
80. The composites hub. *Filiment winding: a cost-effective composites process*. Available at: <https://www.thecompositeshub-india.com/filament-winding--a-cost-effective-composites-process> (Accessed March, 2021).
81. J. D. Buckley and D. D. Edie, *Carbon-carbon materials and composites*. 1993. Noyes Publications, New jersey, USA.
82. M. Wagner and G. Norris, *Boeing 787 dreamliner*. 2009. Zenith Press, Minnesota, USA.
83. Composites. *Use of composite materials in aerospace*. Available at: <https://compositesuk.co.uk/composite-materials/applications/aerospace> (Accessed March, 2021).
84. Composites. *Use of composite materials in automotive*. Available at: <https://compositesuk.co.uk/composite-materials/applications/automotive> (Accessed March, 2021).
85. Composites. *Use of composite materials in consumer goods*. Available at: <https://compositesuk.co.uk/composite-materials/applications/consumer-goods> (Accessed March, 2021).
86. Composites. *Use of composite materials in construction*. Available at: <https://compositesuk.co.uk/composite-materials/applications/construction> (Accessed March, 2021).
87. Composites. *Use of composite materials in marine*. Available at: <https://compositesuk.co.uk/composite-materials/applications/marine> (Accessed March, 2021).
88. Composites. *Medical applications for composite materials*. Available at: <https://compositesuk.co.uk/composite-materials/applications/medical> (Accessed March, 2021).
89. P. H. Franco and L. Drzal, *Comparison of methods for the measurement of fibre/matrix adhesion in composites*. Composites, 1992. **23**(1): p. 2-27.
90. J. K. Kocsis, H. Mahmood, and A. Pegoretti, *Recent advances in fiber/matrix interphase engineering for polymer composites*. Progress in Materials Science, 2015. **73**: p. 1-43.
91. S. Incardona, et al., *The mechanical role of the fibre/matrix transcrystalline interphase in carbon fibre reinforced J-polymer microcomposites*. Composites science and technology, 1993. **47**(1): p. 43-50.

92. P. Drescher, et al., *Strengthening fibre/matrix interphase by fibre surface modification and nanoparticle incorporation into the matrix*. Composites science and technology, 2013. **74**: p. 60-66.
93. T. Clyne and D. Hull, *An introduction to composite materials*. 2019. Cambridge university press, Cambridge, UK.
94. H. Guo, et al., *Interface property of carbon fibers/epoxy resin composite improved by hydrogen peroxide in supercritical water*. Materials Letters, 2009. **63**(17): p. 1531-1534.
95. N. Dilsiz, N. Erinc, and E. Bayramli, *Surface energy and mechanical properties of plasma-modified carbon fibers*. Carbon, 1995. **33**(6): p. 853-858.
96. W. Song, et al., *Effect of the surface roughness on interfacial properties of carbon fibers reinforced epoxy resin composites*. Applied surface science, 2011. **257**(9): p. 4069-4074.
97. J. Hughes, *The carbon fibre/epoxy interface—a review*. Composites Science and Technology, 1991. **41**(1): p. 13-45.
98. R Day and J. C. Rodrigez, *Investigation of the micromechanics of the microbond test*. Composites Science and Technology, 1998. **58**(6): p. 907-914.
99. S. Sockalingam and G. Nilakantan, *Fiber-matrix interface characterization through the microbond test*. International Journal of Aeronautical and Space Sciences, 2012. **13**(3): p. 282-295.
100. C. DiFrancia, T. C. Ward, and R. O. Claus, *The single-fibre pull-out test. I: Review and interpretation*. Composites Part A: Applied Science and Manufacturing, 1996. **27**(8): p. 597-612.
101. S. Deng, L. Ye, and Y. W. Mai, *Measurement of interfacial shear strength of carbon fibre/epoxy composites using a single fibre pull-out test*. Advanced Composite Materials, 1998. **7**(2): p. 169-182.
102. S. C. Gallo, et al., *Viscoelastic response of carbon fibre reinforced polymer during push-out tests*. Composites Part A: Applied Science and Manufacturing, 2018. **112**: p. 178-185.
103. L. Zhang, et al., *Single fiber push-out characterization of interfacial mechanical properties in unidirectional CVI-C/SiC composites by the nano-indentation technique*. Applied Surface Science, 2015. **357**: p. 1427-1433.
104. N. Chandra and H. Ghonem, *Interfacial mechanics of push-out tests: theory and experiments*. Composites Part A: Applied Science and Manufacturing, 2001. **32**(3-4): p. 575-584.
105. P. Järvelä, et al., *The three-fibre method for measuring glass fibre to resin bond strength*. International journal of adhesion and adhesives, 1983. **3**(3): p. 141-147.

106. D. Tripathi and F. Jones, *Single fibre fragmentation test for assessing adhesion in fibre reinforced composites*. Journal of materials science, 1998. **33**(1): p. 1-16.
107. M. Jäger, et al., *Nano-enhanced interface in carbon fibre polymer composite using halloysite nanotubes*. Composites Part A: Applied Science and Manufacturing, 2018. **109**: p. 115-123.
108. A. Awal, et al., *Interfacial studies of natural fibre/polypropylene composites using single fibre fragmentation test (SFFT)*. Composites Part A: Applied Science and Manufacturing, 2011. **42**(1): p. 50-56.
109. Y. Liang, et al., *Enhanced properties of PAN-derived carbon fibres and resulting composites by active screen plasma surface functionalisation*. Plasma Processes and Polymers, 2020.
110. Y. Liu, et al., *Role of matrix modification on interlaminar shear strength of glass fibre/epoxy composites*. Composites Part B: Engineering, 2012. **43**(1): p. 95-98.
111. V. Kostopoulos, et al., *Interlaminar Fracture Toughness of Carbon Fibre-Reinforced Polymer Laminates With Nano-and Micro-Fillers*. Strain, 2011. **47**: p. e269-e282.
112. V. C. Nardone and K. M. Prewo, *Tensile performance of carbon-fibre-reinforced glass*. Journal of materials science, 1988. **23**(1): p. 168-180.
113. K. Sanada, I. Yasuda, and Y. Shindo, *Transverse tensile strength of unidirectional fibre-reinforced polymers and self-healing of interfacial debonding*. Plastics, rubber and composites, 2006. **35**(2): p. 67-72.
114. L. Dickinson, G. Farley, and M. Hinders, *Translaminar reinforced composites: a review*. Journal of Composites, Technology and Research, 1999. **21**(1): p. 3-15.
115. ASTM Standard D5528, 2007e3. *Standard Test Method for Mode I Interlaminar Fracture Toughness of Unidirectional Fiber-Reinforced Polymer Matrix Composites*. 2007. ASTM International, West Conshohocken, PA.
116. ASTM Standard D2344/D2344M-00e1. *Standard Test Method for Short-Beam Shear Strength of Polymer Matrix Composite Materials and Their Laminates*. 2006. ASTM International, West Conshohocken, PA.
117. A. Kelly and A. W. Tyson, *Tensile properties of fibre-reinforced metals: copper/tungsten and copper/molybdenum*. Journal of the Mechanics and Physics of Solids, 1965. **13**(6): p. 329-350.
118. S. Feih, et al., *Testing procedure for the single fiber fragmentation test*. 2004. Riso National Laboratory, Riso.
119. S. Deng, et al., *Evaluation of fibre tensile strength and fibre/matrix adhesion using single fibre fragmentation tests*. Composites Part A: Applied Science and Manufacturing, 1998. **29**(4): p. 423-434.

120. N. Graupner, et al., *Fibre/matrix adhesion of cellulose fibres in PLA, PP and MAPP: a critical review of pull-out test, microbond test and single fibre fragmentation test results*. Composites Part A: Applied Science and Manufacturing, 2014. **63**: p. 133-148.
121. D. Burn, et al., *The usability of recycled carbon fibres in short fibre thermoplastics: interfacial properties*. Journal of Materials Science, 2016. **51**(16): p. 7699-7715.
122. B. F. Sørensen and H. Lilholt. *Fiber pull-out test and single fiber fragmentation test-analysis and modelling*. IOP Conference Series: Materials Science and Engineering, 2016. **139**(1): p.012009.
123. F. Stojcevski, T. B. Hilditch, and L. C. Henderson, *A comparison of interfacial testing methods and sensitivities to carbon fiber surface treatment conditions*. Composites Part A: Applied Science and Manufacturing, 2019. **118**: p. 293-301.
124. L. Drzal and M. Madhukar, *Fibre-matrix adhesion and its relationship to composite mechanical properties*. Journal of materials science, 1993. **28**(3): p. 569-610.
125. M. S. Madhukar and L.T. Drzal, *Fiber-matrix adhesion and its effect on composite mechanical properties: IV. Mode I and mode II fracture toughness of graphite/epoxy composites*. Journal of Composite Materials, 1992. **26**(7): p. 936-968.
126. J. Bijwe and M. Sharma, *Carbon Fabric-Reinforced Polymer Composites and Parameters Controlling Tribological Performance*. Wear of advanced materials, 2013: p. 1-60.
127. G. A. Zickler, et al., *A reconsideration of the relationship between the crystallite size L_a of carbons determined by X-ray diffraction and Raman spectroscopy*. Carbon, 2006. **44**(15): p. 3239-3246.
128. Z. Wen, et al., *Electrochemical polymerization of carbon fibers and its effect on the interfacial properties of carbon reinforced epoxy resin composites*. Composites Part A: Applied Science and Manufacturing, 2019. **119**: p. 21-29.
129. G. S. Corujeira, and H. Dong, *Effect of microstructure on the plasma surface treatment of carbon fibres*. Journal of Composite Materials, 2017. **51**(23): p. 3239-3256.
130. J. W. Herrick, P. E. Gruber Jr, and F. T. Mansur, *Surface treatments for fibrous carbon reinforcements*. 1966. p. Air Force Materials Laboratory.
131. M. Kucera, et al., *Heat treatment of carbon fibres and its influence on mechanical properties of C-C composites*. Acta Montana, Ser. B, 1994. **91**(3): p. 91-102.
132. F. Molleyre and M. Bastick, *4th London Intern. Conf. on Carbon & Graphite, Sept. 23-27, 1974*. Society of Chemical Industry, London, 1976: p. 190-200.
133. S. J. Park, M. K. Seo, and K. Y. Rhee, *Studies on mechanical interfacial properties of oxy-fluorinated carbon fibers-reinforced composites*. Materials Science and Engineering: A, 2003. **356**(1-2): p. 219-226.
134. J. Goan, L. Joo, and G. Sharpe. *Surface treatment for graphite fibers(Graphite fibers surface treatment and interfacial adhesive bonding, considering resin composites shear*

- strength enhancement by sulfuric acid and sodium chlorate oxidation*). Society of the Plastics Industry, Annual Conference, 27 th, Washington, D. C. 1972.
135. B. Xu, X. Wang, and Y. Lu, *Surface modification of polyacrylonitrile-based carbon fiber and its interaction with imide*. Applied Surface Science, 2006. **253**(5): p. 2695-2701.
 136. Z. Wu, C. U. Pittman Jr, and S. D. Gardner, *Nitric acid oxidation of carbon fibers and the effects of subsequent treatment in refluxing aqueous NaOH*. Carbon, 1995. **33**(5): p. 597-605.
 137. J. Gulyás, et al., *Electrochemical oxidation of carbon fibres: surface chemistry and adhesion*. Composites Part A: Applied Science and Manufacturing, 2001. **32**(3-4): p. 353-360.
 138. J. Donnet and P. Ehrburger, *Carbon fibre in polymer reinforcement*. Carbon, 1977. **15**(3): p. 143-152.
 139. S. Yumitori and Y. Nakanishi, *Effect of anodic oxidation of coal tar pitch-based carbon fibre on adhesion in epoxy matrix: Part I. Comparison between H₂SO₄ and NaOH solutions*. Composites Part A: Applied Science and Manufacturing, 1996. **27**(11): p. 1051-1058.
 140. C. Baillie and M. Bader, *Some aspects of interface adhesion of electrolytically oxidized carbon fibres in an epoxy-resin matrix*. Journal of materials science, 1994. **29**(14): p. 3822-3836.
 141. X. Zhang and G. Wu, *Grafting Halloysite Nanotubes with Amino or Carboxyl Groups onto Carbon Fiber Surface for Excellent Interfacial Properties of Silicone Resin Composites*. Polymers, 2018. **10**(10): p. 1171.
 142. J. B. Donnet and R.C. Bansal, *Carbon fibers*. 1998. CRC Press, Florida, USA.
 143. F. An, et al., *Preparation of CNT-hybridized carbon fiber by aerosol-assisted chemical vapor deposition*. Journal of Materials Science, 2012. **47**(7): p. 3327-3333.
 144. B. Singh, et al., *Growth of carbon nanotube filaments on carbon fiber cloth by catalytic chemical vapor deposition*. Applied Nanoscience, 2014. **4**(8): p. 997-1003.
 145. M. Chen, C. M. Chen, and C. F. Chen, *Preparation of high yield multi-walled carbon nanotubes by microwave plasma chemical vapor deposition at low temperature*. Journal of materials science, 2002. **37**(17): p. 3561-3567.
 146. P. Lv, et al., *Increasing the interfacial strength in carbon fiber/epoxy composites by controlling the orientation and length of carbon nanotubes grown on the fibers*. Carbon, 2011. **49**(14): p. 4665-4673.
 147. Z. G. Zhao, et al., *The growth of multi-walled carbon nanotubes with different morphologies on carbon fibers*. Carbon, 2005. **43**(3): p. 663-665.
 148. V. G. De Resende, et al., *Growth of carbon nanotube forests on carbon fibers with an amorphous silicon interface*. Carbon, 2010. **48**(12): p. 3655-3658.

149. Q. Song, et al., *Grafting straight carbon nanotubes radially onto carbon fibers and their effect on the mechanical properties of carbon/carbon composites*. Carbon, 2012. **50**(10): p. 3949-3952.
150. A. R. Boccaccini, et al., *Electrophoretic deposition of carbon nanotubes*. Carbon, 2006. **44**(15): p. 3149-3160.
151. Y. Wang, et al., *Optimization of process parameters for electrophoretic deposition in CNTs/carbon fiber hybrid composites*. High performance structures and materials V, 2010. **112**: p. 291-300.
152. P. Karapappas, et al., *Multi-wall carbon nanotubes chemically grafted and physically adsorbed on reinforcing carbon fibres*. Advanced Composites Letters, 2008. **17**(3): p. 096369350801700304.
153. A. Laachachi, et al., *A chemical method to graft carbon nanotubes onto a carbon fiber*. Materials Letters, 2008. **62**(3): p. 394-397.
154. G. P. Wu, et al., *Direct electrochemical attachment of carbon nanotubes to carbon fiber surfaces*. Carbon, 2011. **49**(6): p. 2152-2155.
155. R. Sager, et al., *Effect of carbon nanotubes on the interfacial shear strength of T650 carbon fiber in an epoxy matrix*. Composites Science and Technology, 2009. **69**(7-8): p. 898-904.
156. Q. Zhang, et al., *Hierarchical composites of carbon nanotubes on carbon fiber: Influence of growth condition on fiber tensile properties*. Composites Science and Technology, 2009. **69**(5): p. 594-601.
157. E. S. Lee, et al., *Effect of hydrogen plasma-mediated surface modification of carbon fibers on the mechanical properties of carbon-fiber-reinforced polyetherimide composites*. Composites Part B: Engineering, 2017. **116**: p. 451-458.
158. W. Fan, et al., *Enhanced interfacial adhesion of aramid fiber III reinforced epoxy composites via low temperature plasma treatment*. Polymer Testing, 2018. **72**: p. 147-156.
159. N. Inagaki, *Plasma surface modification and plasma polymerization*. 1996. CRC Press, Florida, USA.
160. C. Li, T. Bell, and H. Dong, *A study of active screen plasma nitriding*. Surface Engineering, 2002. **18**(3): p. 174-181.
161. F. Hoecker and J. K. Kocsis, *Surface energetics of carbon fibers and its effects on the mechanical performance of CF/EP composites*. Journal of Applied Polymer Science, 1996. **59**(1): p. 139-153.
162. L. G. Tang and J. L. Kardos, *A review of methods for improving the interfacial adhesion between carbon fiber and polymer matrix*. Polymer composites, 1997. **18**(1): p. 100-113.

163. P. Goodhew, A. Clarke, and J. Bailey, *A review of the fabrication and properties of carbon fibres*. *Materials Science and Engineering*, 1975. **17**(1): p. 3-30.
164. D. C. Montgomery, G. C. Runger, and N. F. Hubele, *Engineering statistics*. 2009. John Wiley & Sons, New Jersey, USA.
165. X. Qian, et al., *Effect of fiber microstructure studied by Raman spectroscopy upon the mechanical properties of carbon fibers*. *Journal of Raman Spectroscopy*, 2019. **50**(5): p. 665-673.
166. N. A. Kumar, et al., *Plasma-assisted simultaneous reduction and nitrogen doping of graphene oxide nanosheets*. *Journal of Materials Chemistry A*, 2013. **1**(14): p. 4431-4435.
167. H. Okuda, et al., *Investigating nanostructures in carbon fibres using Raman spectroscopy*. *Carbon*, 2018. **130**: p. 178-184.
168. A. Bessadok, et al., *Influence of chemical modifications on water-sorption and mechanical properties of Agave fibres*. *Composites Part A: Applied Science and Manufacturing*, 2008. **39**(1): p. 29-45.
169. A. Céline, et al., *Qualitative and quantitative assessment of water sorption in natural fibres using ATR-FTIR spectroscopy*. *Carbohydrate polymers*, 2014. **101**: p. 163-170.
170. R. A. Jurf and R. B. Pipes, *Interlaminar fracture of composite materials*. *Journal of Composite Materials*, 1982. **16**(5): p. 386-394.
171. E. N. Voronina, et al., *Pore sealing mechanism in OSG low-k films under ion bombardment*. *Plasma Processes and Polymers*, 2020. **17**(2): p. 1900165.
172. N. Peltekis, et al., *Remote Plasma-Assisted CVD Growth of Carbon Nanotubes in an Optimised Rapid Thermal Reactor*. *Chemical Vapor Deposition*, 2012. **18**(1-3): p. 17-21.
173. N. Inagaki, *Surface modification of polymeric materials by remote plasma*. *Macromolecular symposia*. 2000. **159**(1): p. 151-162.
174. M. M. Giangregorio, et al., *H₂ and N₂ Remote Plasma Processing of Wurtzite-Like Oxides: Implications for Energy Applications*. *Plasma Processes and Polymers*, 2016. **13**(1): p. 147-160.
175. A. Salehi, et al. *Recent advances in OLED optical design*. *Advanced Functional Materials*, 2019. **29**(15), p.1808803.
176. J. Jang and H. Yang, *The effect of surface treatment on the performance improvement of carbon fiber/polybenzoxazine composites*. *Journal of materials science*, 2000. **35**(9): p. 2297-2303.
177. N. Inagaki, et al., *Surface modification of poly (tetrafluoroethylene) with pulsed hydrogen plasma*. *Journal of applied polymer science*, 2002. **83**(2): p. 340-348.

178. M. Moravej, et al., *Properties of an atmospheric pressure radio-frequency argon and nitrogen plasma*. Plasma Sources Science and Technology, 2006. **15**(2): p. 204.
179. R. Bruce, et al., *Relationship between nanoscale roughness and ion-damaged layer in argon plasma exposed polystyrene films*. Journal of Applied Physics, 2010. **107**(8): p. 084310.
180. D. Liu, et al., *Surface modification of high performance PBO fibers using radio frequency argon plasma*. Surface and Coatings Technology, 2012. **206**(16): p. 3534-3541.
181. P. Solís-Fernández, et al., *A comparison between physically and chemically driven etching in the oxidation of graphite surfaces*. Journal of colloid and interface science, 2010. **344**(2): p. 451-459.
182. M. M. Pejovic, G. S. Ristic, and J. P. Karamarkovic, *Electrical breakdown in low pressure gases*. Journal of Physics D: Applied Physics, 2002. **35**(10): p. R91.
183. Y. Yamada, et al., *Surface modification of poly (tetrafluoroethylene) by remote hydrogen plasma*. Macromolecules, 1996. **29**(12): p. 4331-4339.
184. S. Chapman, T. G. Cowling, and D. Burnett, *The mathematical theory of non-uniform gases: an account of the kinetic theory of viscosity, thermal conduction and diffusion in gases*. 1990. Cambridge university press, Cambridge, UK.
185. R. Li, L. Ye, and Y. Mai, *Application of plasma technologies in fibre-reinforced polymer composites: a review of recent developments*. Composites Part A: Applied Science and Manufacturing, 1997. **28**(1): p. 73-86.
186. A. Paul, et al., *UHTC-carbon fibre composites: preparation, oxyacetylene torch testing and characterisation*. Journal of the European Ceramic Society, 2013. **33**(2): p. 423-432.
187. J. Donnet, et al., *Plasma treatment effect on the surface energy of carbon and carbon fibers*. Carbon, 1986. **24**(6): p. 757-770.
188. M. Sharma, et al., *Carbon fiber surfaces and composite interphases*. Composites Science and Technology, 2014. **102**: p. 35-50.
189. D. Li, et al., *Heat-induced internal strain relaxation and its effect on the microstructure of polyacrylonitrile-based carbon fiber*. Journal of Materials Science & Technology, 2014. **30**(10): p. 1051-1058.
190. S. Bennett, D. Johnson, and W. Johnson, *Strength-structure relationships in PAN-based carbon fibres*. Journal of materials science, 1983. **18**(11): p. 3337-3347.
191. W. Reynolds and J. Sharp, *Crystal shear limit to carbon fibre strength*. Carbon, 1974. **12**(2): p. 103-110.
192. CrystalMaker Software, *Elements, atomic radii and the periodic table*. Available at: <http://crystallmaker.com/support/tutorials/atomic-radii/> (Accessed: 20 March 2021).

193. L. B. Nohara, et al., *Evaluation of carbon fiber surface treated by chemical and cold plasma processes*. *Materials Research*, 2005. **8**(3): p. 281-286.
194. C. Lu, et al., *Interfacial adhesion of plasma-treated carbon fiber/poly (phthalazinone ether sulfone ketone) composite*. *Journal of applied polymer science*, 2007. **106**(3): p. 1733-1741.
195. J. Boudou, et al., *Oxygen plasma modification of pitch-based isotropic carbon fibres*. *Carbon*, 2003. **41**(1): p. 41-56.
196. S. Tang and H. S. Choi, *Comparison of low-and atmospheric-pressure radio frequency plasma treatments on the surface modification of poly (methyl methacrylate) plates*. *The Journal of Physical Chemistry C*, 2008. **112**(12): p. 4712-4718.
197. J. Chai, et al., *Wettability interpretation of oxygen plasma modified poly (methyl methacrylate)*. *Langmuir*, 2004. **20**(25): p. 10919-10927.
198. S. Zhuang, et al., *Synthesis of nitrogen-doped graphene catalyst by high-energy wet ball milling for electrochemical systems*. *International Journal of Energy Research*, 2016. **40**(15): p. 2136-2149.
199. F. Liu, Z. Shi, and Y. Dong, *Improved wettability and interfacial adhesion in carbon fibre/epoxy composites via an aqueous epoxy sizing agent*. *Composites Part A: Applied Science and Manufacturing*, 2018. **112**: p. 337-345.
200. J. Y. Ji, et al. *Study on O₂ plasma surface modification of aramid fiber III*. *Applied Mechanics and Materials*. 2012. **155**: p. 936-939.
201. G, S. Corujeira, C. Charitidis, and H. Dong, *Surface functionalization of carbon fibers with active screen plasma*. *Journal of Vacuum Science & Technology A: Vacuum, Surfaces, and Films*, 2017. **35**(2): p. 021404.
202. W. Brennan, et al., *Investigation of the ageing of plasma oxidized PEEK*. *Polymer*, 1991. **32**(8): p. 1527-1530.
203. A. Jordá-Vilaplana, et al., *Effects of aging on the adhesive properties of poly (lactic acid) by atmospheric air plasma treatment*. *Journal of Applied Polymer Science*, 2016. **133**(11).
204. S. Lee, et al., *Photooxidation of amine-terminated self-assembled monolayers on gold*. *The Journal of Physical Chemistry C*, 2010. **114**(23): p. 10512-10519.
205. G. Grail, et al., *Exploring the potential of interleaving to delay catastrophic failure in unidirectional composites under tensile loading*. *Composites Science and Technology*, 2015. **106**: p. 100-109.
206. J. O. Outwater, and M. C. Murphy, *Fracture energy of unidirectional laminates*. *Modern Plastics*, 1970. **47**(9): p. 160.
207. A. Kelly, *Interface effects and the work of fracture of a fibrous composite*. *Proceedings of the Royal Society of London. A. Mathematical and Physical Sciences*, 1970. **319**(1536): p. 95-116.

208. J. Kim, C. Baillie, and Y. Mai, *Interfacial debonding and fibre pull-out stresses*. Journal of materials science, 1992. **27**(12): p. 3143-3154.
209. G. Marom and R. Arridge, *Stress concentrations and transverse modes of failure in composites with a soft fibre-matrix interlayer*. Materials Science and Engineering, 1976. **23**(1): p. 23-32.
210. A. Scott, et al., *Damage accumulation in a carbon/epoxy composite: comparison between a multiscale model and computed tomography experimental results*. Composites Part A: Applied Science and Manufacturing, 2012. **43**(9): p. 1514-1522.
211. D. R. Aroush, et al., *A study of fracture of unidirectional composites using in situ high-resolution synchrotron X-ray microtomography*. Composites science and technology, 2006. **66**(10): p. 1348-1353.
212. A. Scott, et al., *In situ fibre fracture measurement in carbon–epoxy laminates using high resolution computed tomography*. Composites Science and Technology, 2011. **71**(12): p. 1471-1477.
213. S. C. Joshi and V. Dikshit, *Enhancing interlaminar fracture characteristics of woven CFRP prepreg composites through CNT dispersion*. Journal of Composite Materials, 2012. **46**(6): p. 665-675.